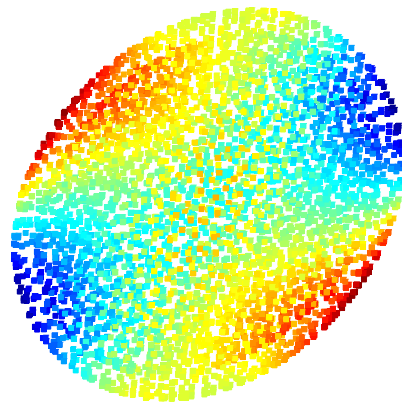


# Meshfree Methods for the Dynamics of Solids

Markus von Nida



Kaiserslautern, April 2005

The picture on the front page displays the first component of the deviatoric stress  $S$  in case of simple shearing and can be found on page 88.

# Meshfree Methods for the Dynamics of Solids

Vom Fachbereich Mathematik  
der Technischen Universität Kaiserslautern  
zur Verleihung des akademischen Grades  
Doktor der Naturwissenschaften  
(Doctor rerum naturalium, Dr. rer. nat.)  
genehmigte Dissertation

von  
**Dipl.-Math. techn. Markus von Nida**

Referent: Prof. Dr. Dr. h.c. em. Helmut Neunzert  
Koreferent: Prof. Dr. Michael Junk

Kaiserslautern, April 2005



I would like to take the opportunity to thank all those who have supported and accompanied me during the last years. First and foremost, I would like to express my sincere gratitude to Prof. Helmut Neunzert for giving me the opportunity to work in this exciting field at the *Fraunhofer Institut für Techno- und Wirtschaftsmathematik* (ITWM). His enduring encouragement and his helpful advice gave me motivation and guided me to a better understanding of the arising problems. I would like to thank Prof. Michael Junk for having accepted to be my second referee.

I am very grateful to Dr. Jörg Kuhnert for his support, particular in all questions concerning the numerical method and the implementation. Moreover, I am deeply obliged to Dr. Sudarashan Tiwari, Prof. Axel Klar, Prof. René Pinnau and Dr. Thomas Götz for many helpful hints and discussions. Furthermore, I would like to express my gratitude to the entire *Arbeitsgruppe Technomathematik* at TU Kaiserslautern and the Department *Transportvorgänge* at the Fraunhofer ITWM for the amicable atmosphere. I am very thankful to Dipl.-Math. techn. Nicole Marheineke and Dr. Christian Schick for proof-reading the manuscript and many interesting discussions.

Mein herzlichster Dank gilt meinen Eltern, die mich während meines gesamten Studiums und meiner Promotion unterstützt und immer an mich geglaubt haben.



# Table of Contents

<b>Preface</b>	<b>5</b>
<b>1 Physical Model for Elastic Solids</b>	<b>7</b>
1.1 Conservation Laws . . . . .	7
1.1.1 Fundamental Equations . . . . .	8
1.1.2 Mixed Lagrangian-Eulerian Formulation of the Problem . . . . .	8
1.2 Stress Tensor . . . . .	11
1.2.1 Linear Elasticity . . . . .	11
1.2.2 Limitations of Hooke's Law . . . . .	14
1.2.3 Evolution of the Stress Tensor . . . . .	16
1.3 Final Set of Equations . . . . .	18
<b>2 Hyperbolic Systems</b>	<b>21</b>
2.1 Classification of Systems of PDEs . . . . .	21
2.1.1 Quasi-linear Form . . . . .	22
2.1.2 Eigenvalues . . . . .	23
2.2 Properties of Hyperbolic Systems . . . . .	25
2.2.1 Propagation of Information . . . . .	25
2.2.2 Characteristic Variables . . . . .	27
2.2.3 Non-smooth Solutions . . . . .	28
2.3 Numerical Treatment of Hyperbolic Systems . . . . .	28
<b>3 The Finite Pointset Method</b>	<b>31</b>
3.1 Classical Smoothed Particle Hydrodynamics . . . . .	31
3.1.1 Particle Approximation of Functions . . . . .	31
3.1.2 Limitations of SPH . . . . .	32
3.1.3 Related Research on SPH . . . . .	34
3.2 Finite Pointset Method . . . . .	34
3.2.1 Basic Idea and Definitions . . . . .	34
3.2.2 Alternative Minimization Problem . . . . .	36
3.2.3 Upwinding in FPM . . . . .	38

<b>4</b>	<b>Operator Splitting</b>	<b>39</b>
4.1	Operator Splitting in Eulerian Description . . . . .	39
4.2	Operator Splitting in Lagrangian Description . . . . .	41
4.2.1	Splitting of the Actual System . . . . .	42
4.2.2	Movement of the Particles . . . . .	45
4.3	Time Integration . . . . .	46
<b>5</b>	<b>Numerical Method</b>	<b>47</b>
5.1	Euler Part - Change of Volume . . . . .	47
5.1.1	Characteristic System for Euler Equations . . . . .	49
5.1.2	Boundary Conditions . . . . .	51
5.1.3	Single Upwind Direction . . . . .	52
5.1.4	Minimization of the Quadratic Form . . . . .	54
5.1.5	Remarks on Three Dimensions . . . . .	55
5.1.6	Multiple Upwind Directions . . . . .	56
5.2	Shear Part . . . . .	57
5.2.1	Characteristic System . . . . .	58
5.2.2	Technical Problems . . . . .	59
5.2.3	Dimensional Upwinding . . . . .	61
5.2.4	Boundary Conditions . . . . .	64
5.3	Rotation Part - Jaumann Rate . . . . .	64
5.3.1	Reduced System for Rotation Part . . . . .	64
5.3.2	Basic Results for Rotations . . . . .	65
5.3.3	Rotation of the Stress Tensor . . . . .	67
5.4	Coupling of Systems . . . . .	67
<b>6</b>	<b>Results for the Subsystems</b>	<b>69</b>
6.1	Results for the Euler Part . . . . .	70
6.1.1	Three-Dimensional Shock Tube Problem . . . . .	70
6.1.2	Pulsation of a Sphere . . . . .	75
6.1.3	Flattening of a Sphere . . . . .	79
6.1.4	Validation . . . . .	81
6.2	Results for the Shear Part . . . . .	82
6.2.1	Shearing of a Sphere . . . . .	83
6.2.2	Validation . . . . .	88
6.3	Results for the Rotation Part . . . . .	90
6.3.1	Rotation of a Sphere . . . . .	90
<b>7</b>	<b>Results for Coupled System</b>	<b>93</b>
7.1	Shearing of a Sphere . . . . .	94
7.2	Rotation of a Sphere . . . . .	99



---

7.2.1	Results . . . . .	99
7.2.2	Correction Strategies . . . . .	103
7.2.3	Approximation Properties . . . . .	106
7.3	Validation . . . . .	112
7.4	Discussion . . . . .	113
<b>Conclusion</b>		<b>117</b>
<b>A Proof of Lemma 3.1</b>		<b>119</b>
<b>Nomenclature</b>		<b>123</b>
<b>References</b>		<b>125</b>



# Preface

Over the last decades, mathematical modeling has reached nearly all fields of natural science. The abstraction and reduction to a mathematical model has proven to be a powerful tool to gain a deeper insight into physical and technical processes. The increasing computing power has made numerical simulations available for many industrial applications. The advantages for industry are obvious. These are for example the abolition of expensive prototypes in the design and optimization of products and the ability to give lifetime prediction for mechanical parts.

In recent years, mathematicians and engineers have turned their attention to model solid materials. New challenges have been found in the simulation of solids and fluid-structure interactions. In this context, it is indispensable to study the dynamics of elastic solids. Elasticity is a main feature of solid bodies while demanding a great deal of the numerical treatment.

There exists a multitude of commercial tools to simulate the behavior of elastic solids. Anyhow, the majority of these software packages consider quasi-stationary problems. But in this thesis, we are interested in highly dynamical problems, e.g. the rotation of a solid. The applicability to free-boundary problems is a further emphasis of our considerations.

In the last years, *meshless* or *particle methods* have attracted more and more attention. In many fields of numerical simulation these methods are on a par with classical methods or superior to them. By now a broad spectrum of physical and technical applications has successfully been solved with meshless methods. Most particle approximations are assigned to the finite difference or finite volume methods. The *Finite Pointset Method* (FPM) is a particle method developed by Dr. Jörg Kuhnert in [24] that uses a moving least squares particle approximation operator. The application of this method to various industrial problems at the Fraunhofer ITWM has shown that the method is particularly suitable for highly dynamical problems with free surfaces and strongly changing geometries.

Thereby, FPM offers exactly the features that we require for the simulation of solid bodies. In particular, the detachedness of the method from an underlying grid makes FPM very interesting for various problems.

The main objective of the present work is thus to provide a numerical scheme on the basis of the Finite Pointset Method capable to simulate the behavior of elastic solids. From the previous discussion derives the following structure of this thesis.

In the first chapter we present the system of partial differential equations describing the dynamics of elastic solids. We treat the solid as a continuum and consider the balance laws for mass, momentum and total energy. There, the system of equations is given in a mixed Eulerian-Lagrangian formulation. In Section 1.2 we focus our attention to the constitutive law for the stress tensor. We present evolution equations for the deviatoric part of the stress tensor in order to circumvent limitations of the classical Hooke's law.

In Chapter 2 we show that the previously derived system of partial differential equations forms a hyperbolic system. We give some basic properties of this class of systems and make some comments concerning the stability of finite difference schemes. Furthermore, we give the characteristic formulation of a hyperbolic system to extract additional information.

We start Chapter 3 with a short introduction to *Smoothed Particle Hydrodynamics* (SPH). We point out some limitations of the classical method and give a short overview on recent research in this field. In Section 3.2 we present the basic principle of the *Finite Pointset Method*. In particular, we provide the concept of upwinding in a given direction as a key ingredient for stabilizing hyperbolic systems.

The motion of an elastic solid is the superposition of rigid body movements and internal displacements. In general, these processes take place on different time scales. We take these time scales into account and present an operator splitting in Chapter 4. Moreover, the splitting simplifies characteristic considerations needed to successfully design a stable scheme. Additionally, we make some remarks on operator splitting in a Lagrangian framework.

The previous chapters provide the constituents to formulate our new numerical scheme. In Chapter 5 we describe in detail the development of different methods to solve each of the subsystems established in Section 4.2. Hereby, we introduce the notion of *system-inherent* directions and *dimensional upwinding*. In particular, we equip the particle approximation with upwinding in suitable directions.

In Chapter 6 we present numerical results obtained for the different subsystems. We turn our main attention to free-boundary problems. In general, these problems are difficult to handle with mesh-based methods as in many cases the surface does not coincide with grid points. The coupling of the different methods for the subsystems is given in Chapter 7. There, a full elastic body is simulated and the results are presented.

We close this work with some final conclusions and an outlook on future work.

# Chapter 1

## Physical Model for Elastic Solids

In this chapter we will derive a physical model for the description of elastic solids. For this purpose, we assume the elastic body to be a continuum. We will state balance laws and provide a constitutive relation to close the model.

### 1.1 Conservation Laws

In order to establish a mathematical model, one basic concept is widely used. This concept is based on the fact that certain physical quantities are conserved during the time.

Consider an arbitrary control volume  $\Omega \subset \mathbb{R}^d$  and the density  $\phi$  of a conserved quantity. The change of the amount of the quantity inside the volume is given by the convective flux  $\mathcal{F}$  through the boundary  $\partial\Omega$  and additional volume and surface sources denoted by  $\mathcal{V}$  and  $\mathcal{S}$ , respectively,

$$\frac{d}{dt} \int_{\Omega} \phi \, d\mathbf{x} = - \int_{\partial\Omega} \mathbf{n} \cdot \mathcal{F} \, d\mathbf{n} + \int_{\Omega} \mathcal{V} \, d\mathbf{x} + \int_{\partial\Omega} \mathbf{n} \cdot \mathcal{S} \, d\mathbf{n},$$

where  $\mathbf{n}$  is an outward normal to  $\partial\Omega$ . The surface integrals can be transformed into volume integrals with the help of Gauss' Theorem. Since the equation above holds for any control volume, we obtain thus the differential form

$$\frac{\partial\phi}{\partial t} + \operatorname{div}(\mathcal{F}) = \mathcal{V} + \operatorname{div}(\mathcal{S}). \quad (1.1)$$

Equation (1.1) is called a *balance law* for the quantity  $\phi$ . If  $\mathcal{V}$  and  $\mathcal{S}$  are both equal to zero, the equation is called *conservation law*. Furthermore, the equation is given in *conservative form*. A detailed discussion about the derivation of balance laws can be found in any textbook on conservation laws, e.g. [27].

### 1.1.1 Fundamental Equations

In order to describe a physical process by an adequate mathematical model we need to determine the conserved quantities and to provide equations for the flux and the source terms.

The conserved quantities are the mass  $\rho$ , the momentum  $\rho\mathbf{v}$  and the total energy  $\rho E$ . The equations describing the change of these quantities in  $d$  space dimensions are

$$\begin{aligned} \frac{\partial \rho}{\partial t} + \operatorname{div}(\rho\mathbf{v}) &= 0 \\ \frac{\partial(\rho\mathbf{v})}{\partial t} + \operatorname{div}(\rho\mathbf{v} \otimes \mathbf{v}) &= \operatorname{div}(\boldsymbol{\sigma}) + \rho\mathbf{g} \\ \frac{\partial(\rho E)}{\partial t} + \operatorname{div}(\rho E\mathbf{v}) &= \operatorname{div}(\boldsymbol{\sigma}\mathbf{v}) + \rho\mathbf{g} \cdot \mathbf{v} - \operatorname{div}(\mathbf{q}) + Q, \end{aligned} \quad (1.2)$$

where  $\partial/\partial t$  denotes the partial derivative with respect to time. Here,  $\boldsymbol{\sigma}$  represents the stress tensor,  $\mathbf{g}$  the gravity,  $\mathbf{q}$  the heat flux and  $Q$  a source term to the total energy.

These very fundamental equations apply to a wide range of problems and their derivation can be found in any standard textbook on partial differential equations, e.g. [27, Chapter I.1].

The system of equations (1.2) is not closed, which means that there are more unknowns than equations. In order to close the system we need a so-called *closure relation* or *constitutive law* which expresses the stress tensor  $\boldsymbol{\sigma}$  in terms of the quantities  $\rho$ ,  $\rho\mathbf{v}$  and  $\rho E$ . In Section 1.2 the derivation of the applied stress tensor will be given. For our problem, we will neglect gravity as well as heat fluxes and sources  $Q$ .

**Remark 1.1** *The equations above apply to a wide range of materials and physical problems. Anyhow, deriving a mathematical model requires the prescription of the material-dependent stress tensor in terms of the conserved quantities and the description of suitable initial and boundary conditions according to the given problem. Thereby, the constitutive laws are very often taken from physics or other natural sciences.*

### 1.1.2 Mixed Lagrangian-Eulerian Formulation of the Problem

The Finite Pointset Method (FPM) is a particle method. Therefore, we have to describe the change of the quantities along the particle paths. Thereby, it becomes necessary to reformulate the set of equations given in Eulerian coordinates in a Lagrangian setting. But we do not aim for a purely Lagrangian description of the governing equations. A detailed discussion about FPM will be given in Chapter 3.

First, let us give some basic definitions to motivate the different formulations of the equations. For a short introduction to that topic we refer to [37].

**Definition 1.1 (Configuration, Motion, Displacement)** *Let  $\Omega$  be a simply connected domain in  $\mathbb{R}^d$ .*

- We call a domain  $\Omega \subset \mathbb{R}^d$  that is initially occupied by a body  $\mathcal{B}$  the reference configuration of  $\mathcal{B}$ .
- A continuous mapping  $X(\boldsymbol{\xi}, t)$  with

$$X : \Omega \times \mathbb{R}^+ \longrightarrow \mathbb{R}^d$$

such that  $X(\boldsymbol{\xi}, 0) = \boldsymbol{\xi}$  for all  $\boldsymbol{\xi} \in \Omega$  which is injective for fixed time  $t \in \mathbb{R}^+$  is called the motion of the body  $\mathcal{B}$ .

- The domain  $\Omega_t := X(\Omega, t)$  is called the actual configuration of the body  $\mathcal{B}$  at time  $t$ .
- We introduce the mapping  $X_t : \Omega \longrightarrow \Omega_t \subset \mathbb{R}^d$  defined as

$$X_t(\cdot) := X(\cdot, t)$$

for fixed  $t$ .  $X_t$  is invertible with inverse  $X_t^{-1}$ .

- The coordinates attached to the reference and the actual configuration are called Lagrangian coordinates and Eulerian coordinates, respectively.
- The displacement  $\mathbf{u}(\boldsymbol{\xi}, t)$  of a point  $\boldsymbol{\xi}$  in  $\mathcal{B}$  at time  $t$  is given by the relation

$$\mathbf{u}(\boldsymbol{\xi}, t) := X(\boldsymbol{\xi}, t) - \boldsymbol{\xi}. \quad (1.3)$$

Formally, the motion is simply a coordinate transformation from Lagrangian to Eulerian coordinates. We relate the motion  $X$  with the velocity  $\mathbf{v}$  given in equation (1.2) by the differential equation

$$\frac{\partial}{\partial t} X(\boldsymbol{\xi}, t) = \mathbf{v}(X(\boldsymbol{\xi}, t), t). \quad (1.4)$$

Let  $\boldsymbol{\xi}$  and  $\mathbf{x}$  be Lagrangian and Eulerian coordinates, respectively. The motion  $X$  maps a material point  $\boldsymbol{\xi}$  onto its actual position  $\mathbf{x} = X(\boldsymbol{\xi}, t)$  in space at time  $t$ . The Lagrangian and Eulerian coordinates are occasionally referred to as *material* and *actual coordinates*. For fixed  $t$  we have

$$X_0(\boldsymbol{\xi}) = \boldsymbol{\xi}, \quad X_t(X_t^{-1}(\mathbf{x})) = \mathbf{x}, \quad X_t^{-1}(X_t(\boldsymbol{\xi})) = \boldsymbol{\xi}.$$

**Remark 1.2** *Two different material points cannot occupy the same point in space after some time  $t$ . For that reason invertibility of the mapping  $X_t$  is a reasonable assumption.*

Consider a function  $f(\mathbf{x}, t)$  given in actual coordinates. We define a function  $\hat{f}(\boldsymbol{\xi}, t)$  in material coordinates by

$$\hat{f}(\boldsymbol{\xi}, t) := f(X(\boldsymbol{\xi}, t), t) = f(\mathbf{x}, t)|_{\mathbf{x}=X(\boldsymbol{\xi}, t)}. \quad (1.5)$$

This means that  $\hat{f}(\boldsymbol{\xi}, t)$  describes  $f$  along the path of material point  $\boldsymbol{\xi}$ .

To rewrite the system of equations we have to give the derivatives in Lagrangian coordinates. At first, we consider the time derivative:

$$\begin{aligned} \frac{\partial \hat{f}(\boldsymbol{\xi}, t)}{\partial t} &= \frac{\partial f(X(\boldsymbol{\xi}, t), t)}{\partial t} \\ &= \left( \frac{\partial f(\mathbf{x}, t)}{\partial t} + \frac{\partial X(\boldsymbol{\xi}, t)}{\partial t} \cdot \nabla f(\mathbf{x}, t) \right) \Big|_{\mathbf{x}=X_t(\boldsymbol{\xi})} \\ &\stackrel{(1.4)}{=} \left( \frac{\partial f(\mathbf{x}, t)}{\partial t} + \mathbf{v}(\mathbf{x}, t) \cdot \nabla f(\mathbf{x}, t) \right) \Big|_{\mathbf{x}=X_t(\boldsymbol{\xi})}. \end{aligned} \quad (1.6)$$

For the spatial derivative we obtain

$$\frac{\partial f(\mathbf{x}, t)}{\partial x_i} = \frac{\partial \hat{f}(X_t^{-1}(\mathbf{x}), t)}{\partial x_i} = \frac{\partial \hat{f}(\boldsymbol{\xi}, t)}{\partial \xi_j} \frac{\partial X_{t_j}^{-1}(\mathbf{x})}{\partial x_i} \Big|_{\boldsymbol{\xi}=X_t^{-1}(\mathbf{x})}, \quad (1.7)$$

where  $X_{t_j}^{-1}$  is the  $j$ -th component of  $X_t^{-1}$ . We introduce the matrix  $Z$  defined by

$$Z_{ij} := \frac{\partial X_{t_j}^{-1}(\mathbf{x})}{\partial x_i}$$

and can write

$$\nabla_{\mathbf{x}} f(\mathbf{x}, t) = Z \nabla_{\boldsymbol{\xi}} \hat{f}(\boldsymbol{\xi}, t) \Big|_{\boldsymbol{\xi}=X_t^{-1}(\mathbf{x})}.$$

Let us consider the conservation of mass. The equation reads in actual coordinates

$$\begin{aligned} 0 &= \frac{\partial \rho(\mathbf{x}, t)}{\partial t} + \operatorname{div}(\rho(\mathbf{x}, t) \mathbf{v}(\mathbf{x}, t)) \\ &= \frac{\partial \rho(\mathbf{x}, t)}{\partial t} + \mathbf{v}(\mathbf{x}, t) \cdot \nabla \rho(\mathbf{x}, t) + \rho(\mathbf{x}, t) \operatorname{div}(\mathbf{v}(\mathbf{x}, t)). \end{aligned}$$

This equation can be rewritten in Lagrangian coordinates using (1.6) and (1.7).

$$0 = \frac{\partial \hat{\rho}(\boldsymbol{\xi}, t)}{\partial t} + \hat{\rho}(\boldsymbol{\xi}, t) \frac{\partial \hat{v}_i(\boldsymbol{\xi}, t)}{\partial \xi_j} \frac{\partial X_{t_j}^{-1}(\mathbf{x})}{\partial x_i} \Big|_{\mathbf{x}=X_t(\boldsymbol{\xi})} \quad (1.8)$$

with Einstein's summation convention. We make the following observations:

- The Lagrangian formulation describes the change of the quantities along the path of the material points.
- Problems arise if the motion is not known. Even if it is known, the term including the spatial derivative is much more complicated than in Eulerian formulation.
- In a particle method the geometric arrangement of neighboring material points is known by the position of each particle, i.e. the Eulerian coordinates are given for the particles.



In the numerical scheme we make use of these properties and apply a mixed formulation of the system of equations. The update of the quantities is given at fixed material points. But the construction of the spatial derivatives is done using the actual positions of the points.

$$\frac{\partial}{\partial t} \hat{\rho}(\boldsymbol{\xi}, t) = -\hat{\rho}(\boldsymbol{\xi}, t) \operatorname{div}(\mathbf{v}(\mathbf{x}, t)) \Big|_{\mathbf{x}=X_t(\boldsymbol{\xi})} \quad (1.9)$$

$$\begin{aligned} \frac{\partial}{\partial t} \left( \hat{\rho}(\boldsymbol{\xi}, t) \hat{v}_i(\boldsymbol{\xi}, t) \right) &= -\hat{\rho}(\boldsymbol{\xi}, t) \hat{v}_i(\boldsymbol{\xi}, t) \operatorname{div}(\mathbf{v}(\mathbf{x}, t)) \Big|_{\mathbf{x}=X_t(\boldsymbol{\xi})} \\ &\quad + \frac{\partial}{\partial x_j} \sigma^{ij}(\mathbf{x}, t) \Big|_{\mathbf{x}=X_t(\boldsymbol{\xi})} \end{aligned} \quad (1.10)$$

$$\begin{aligned} \frac{\partial}{\partial t} \left( \hat{\rho}(\boldsymbol{\xi}, t) \hat{E}(\boldsymbol{\xi}, t) \right) &= -\hat{\rho}(\boldsymbol{\xi}, t) \hat{E}(\boldsymbol{\xi}, t) \operatorname{div}(\mathbf{v}(\mathbf{x}, t)) \Big|_{\mathbf{x}=X_t(\boldsymbol{\xi})} \\ &\quad + \operatorname{div}(\boldsymbol{\sigma}(\mathbf{x}, t) \mathbf{v}(\mathbf{x}, t)) \Big|_{\mathbf{x}=X_t(\boldsymbol{\xi})}, \end{aligned} \quad (1.11)$$

with  $i = 1, \dots, d$ . The functions given in Eulerian and Lagrangian coordinates, respectively, are connected by (1.5).

**Remark 1.3** *Note that the quantities  $\hat{\rho}$ ,  $\hat{\mathbf{v}}$  and  $\hat{E}$  are not the Lagrangian analogon of  $\rho$ ,  $\mathbf{v}$  and  $E$ , respectively. They are the original ones given with respect to the transformed coordinate system.*

## 1.2 Stress Tensor

The physical model is not yet complete. As mentioned in Section 1.1 we have to close the system (1.9) - (1.11) by providing a material law to express the relation of the stress tensor  $\boldsymbol{\sigma}$  with the conserved quantities. We will determine a suitable law with the help of the theory of *linear elasticity*. For a short motivation and a more detailed introduction to the theory we refer to [37] and [44], respectively.

**Convention** *In this section, we are working in a strict Lagrangian framework. Hence, we skip the notation  $\hat{\cdot}$  for functions given in Lagrangian coordinates.*

### 1.2.1 Linear Elasticity

Consider two points  $\boldsymbol{\xi}^1$  and  $\boldsymbol{\xi}^2$  with difference vector  $\boldsymbol{\xi}$  in the reference configuration  $\Omega$  as sketched in Figure 1.1. Under a motion  $X$  these two points are mapped onto  $\mathbf{x}^1$  and  $\mathbf{x}^2$ , respectively.

**Convention** *In the following,  $\|\cdot\|$  always denotes the standard Euclidean norm.*

Note that for small  $\|\boldsymbol{\xi}\|$  a Taylor expansion of  $\mathbf{x}$  yields

$$\mathbf{x} = X(\boldsymbol{\xi}^2, t) - X(\boldsymbol{\xi}^1, t) = (\boldsymbol{\xi} \cdot \nabla_{\boldsymbol{\xi}}) X(\boldsymbol{\xi}^1, t) + O(\|\boldsymbol{\xi}\|^2).$$

Hence, the distance  $\|\mathbf{x}\|$  between the new positions can be computed according to

$$\|\mathbf{x}\|^2 = \mathbf{x}^T \mathbf{x} = \boldsymbol{\xi}^T (\nabla_{\boldsymbol{\xi}} X(\boldsymbol{\xi}^1, t))^T (\nabla_{\boldsymbol{\xi}} X(\boldsymbol{\xi}^1, t)) \boldsymbol{\xi} + O(\|\boldsymbol{\xi}\|^2).$$

Introducing the displacement gradient  $\nabla_{\boldsymbol{\xi}} \mathbf{u}(\boldsymbol{\xi}, t) = \nabla_{\boldsymbol{\xi}} X(\boldsymbol{\xi}, t) - I$ , this simplifies to

$$\|\mathbf{x}\|^2 = \boldsymbol{\xi}^T (\nabla_{\boldsymbol{\xi}} \mathbf{u} + (\nabla_{\boldsymbol{\xi}} \mathbf{u})^T + (\nabla_{\boldsymbol{\xi}} \mathbf{u})^T \nabla_{\boldsymbol{\xi}} \mathbf{u} + I) \boldsymbol{\xi} + O(\|\boldsymbol{\xi}\|^2).$$

This gives a good motivation to define the *Green-St. Venant strain tensor*

$$C := \frac{1}{2} (\nabla_{\boldsymbol{\xi}} \mathbf{u} + (\nabla_{\boldsymbol{\xi}} \mathbf{u})^T + (\nabla_{\boldsymbol{\xi}} \mathbf{u})^T \nabla_{\boldsymbol{\xi}} \mathbf{u})$$

which is a first order approximation for the change of the length of  $\boldsymbol{\xi}$  under a motion  $X$ . In the following, we will consider a simpler strain tensor.

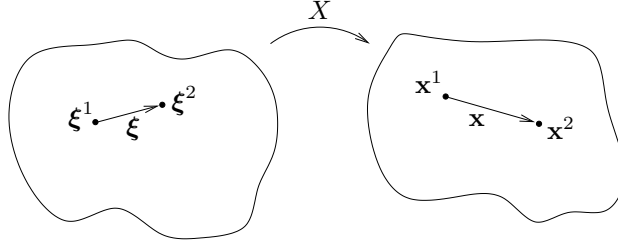


Figure 1.1: Deformation of a configuration

**Definition 1.2 (Linearized strain tensor)** Let  $X(\boldsymbol{\xi}, t)$  be a given motion and  $\mathbf{u}(\boldsymbol{\xi}, t) = X(\boldsymbol{\xi}, t) - \boldsymbol{\xi}$  the corresponding displacement field. Then the linearized strain tensor is defined by

$$\varepsilon_{\boldsymbol{\xi}} = \frac{1}{2} (\nabla_{\boldsymbol{\xi}} \mathbf{u} + (\nabla_{\boldsymbol{\xi}} \mathbf{u})^T), \quad (1.12)$$

where the subscript  $\boldsymbol{\xi}$  indicates material coordinates.

**Remark 1.4** For the proper application of this strain tensor one should always keep in mind that

- the linearized strain tensor  $\varepsilon_{\boldsymbol{\xi}}$  is an approximation of the Green-St. Venant strain tensor which is only valid for small  $\|\nabla_{\boldsymbol{\xi}} \mathbf{u}\|$ , and
- the displacement and thus the strain tensor are given in coordinates with respect to the reference configuration.

**Remark 1.5** In contrast to  $C$ , the linearized strain tensor  $\varepsilon_{\boldsymbol{\xi}}$  is not equal to zero for a rigid motion. This is an important fact since the correct rotation of a solid body is a main motivation for this work. A rigid body rotation is described by

$$X(\boldsymbol{\xi}) = M\boldsymbol{\xi},$$

where  $M$  is an orthogonal matrix with  $\det(M) = 1$ . Then

$$u(\boldsymbol{\xi}) = X(\boldsymbol{\xi}) - \boldsymbol{\xi} = (M - I)\boldsymbol{\xi}$$

and

$$\varepsilon_{\xi} = \frac{1}{2}(M + M^T) - I \neq 0$$

in general. Anyhow, we will see later that the linearized strain tensor is still applicable for our problem.

**Convention** In the following, we always consider the linearized strain tensor (1.12). Therefore, we will drop the term “linearized”.

In 1676 Robert Hooke stated under the anagram “CEIHNOSSTTUV” that “The power of any springy body is in the same proportion with the extension.” Later he revealed that the anagram means UT TENSIO SIC VIS and this work forms the basis of the theory of linear elasticity. Cauchy generalized Hooke’s law to three-dimensional anisotropic elastic bodies. Assuming isotropy, this can be expressed by

$$\boldsymbol{\sigma} = \lambda \operatorname{trace}(\varepsilon_{\xi})I + 2\mu\varepsilon_{\xi}. \quad (1.13)$$

This relation is known as the *generalized Hooke’s law*, where  $\lambda$  and  $\mu$  are the so-called *Lamé constants*. In order to apply this equation correctly it is important to consider its origin and limitations. We have already said that the strain tensor  $\varepsilon_{\xi}$  defined by (1.12) is only valid for small displacement gradients.

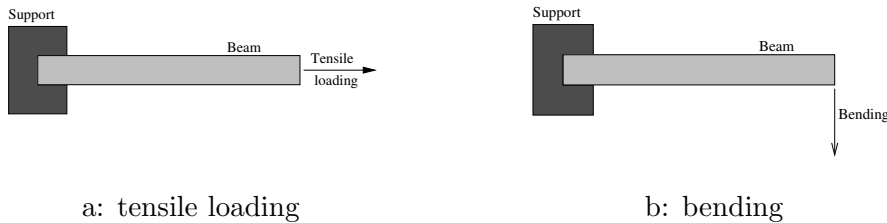


Figure 1.2: Experimental setup to determine the Lamé constants

Hooke’s law and its generalizations have been applied since long by material scientists. Two typical settings to determine the Lamé constants of a specific elastic solid are sketched in Figure 1.2. In these configurations a beam is fixed at one side. On the other side either a normal or a tangential force is applied. These classical experiments have the following assumptions in common.

- **Reference configuration:** The undeformed reference configuration is known. In particular, the solids in the experiments are initially free of stress.
- **Quasi-static:** The experiments are performed in a very slow way such that they can be considered to be quasi-static.

- **Small displacement:** The beam is stretched or bent only by a small amount compared to the size of it.

The last assumption is due to the fact that the applied strain tensor  $\varepsilon_\xi$  is a linearized tensor valid only for small displacement gradients. Furthermore, Hooke's law is a linearized law for small displacements.

The main objective of this section is to make the generalized Hooke's law applicable in a numerical scheme. In particular, the time discretization violates the first assumption. Therefore, it is not possible to apply Hooke's law unchanged in a numerical scheme. In Section 1.2.2 we will describe the difficulties in more detail.

However, we will first show the relevance of this linear theory for the simulation of solid bodies. Figure 1.3 shows the stress-strain relation for (a) annealed low carbon (0.18% C) steel and (b) 316 annealed stainless steel (UNS S31600). The pictures are taken from [49]. Typical for all solid materials is the fact that

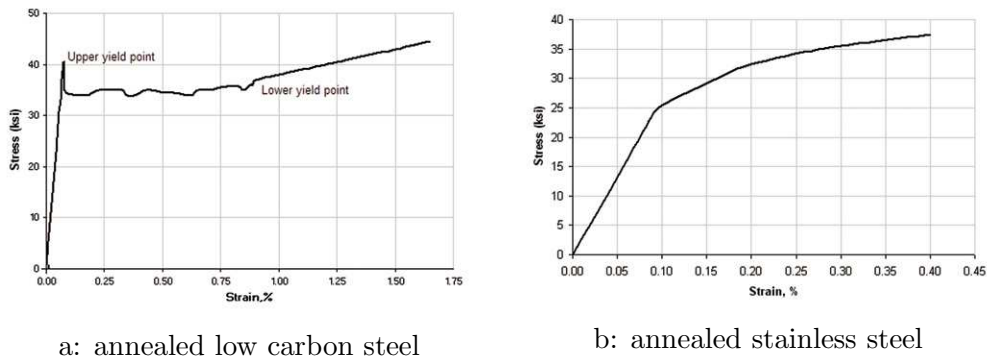


Figure 1.3: Stress-strain relation for two different steels

the stress-strain curve is linear in the beginning. The size of the linear regime depends on the material. However, describing the elastic regime correctly is a first important step towards simulating the whole range of industrial problems connected with solid bodies.

### 1.2.2 Limitations of Hooke's Law

Hooke's law is a linear law in which it is assumed that the displacement gradients are small. In order to apply the law to a wider range of problems we introduce a splitting of the stress tensor into a *volumetric* and a *deviatoric* part.

$$\begin{aligned}
 \sigma &= \lambda \operatorname{trace}(\varepsilon_\xi) I + 2\mu \varepsilon_\xi \\
 &= \left( \lambda + \frac{2}{3}\mu \right) \operatorname{trace}(\varepsilon_\xi) I + 2\mu \left( \varepsilon_\xi - \frac{1}{3} \operatorname{trace}(\varepsilon_\xi) I \right).
 \end{aligned}$$

We define  $p$  and  $S$  by

$$p := -\left(\lambda + \frac{2}{3}\mu\right)\text{trace}(\varepsilon_\xi) \quad (1.14)$$

$$S := 2\mu\left(\varepsilon_\xi - \frac{1}{3}\text{trace}(\varepsilon_\xi)I\right) \quad (1.15)$$

and thus obtain

$$\sigma = -pI + S. \quad (1.16)$$

It follows directly from this definition that the deviatoric part  $S$  is traceless. Furthermore, the part  $p$  acts isotropically in any direction. In analogy to fluid dynamics, the volumetric part  $p$  is called the *pressure*. The deviatoric part  $S$  describes the shear forces.

At first glance, this splitting seems to make no sense. In fluids, i.e. in liquids and gases, pressure is a well-known physical quantity. For solid bodies this is different and the introduction of a pressure term requires further motivation.

In the first place, the definition of a pressure part and a deviatoric part was motivated to stress the analogy to liquids in the equations. But the real advantage of the splitting is that we are able to replace the expression for the pressure (1.14) by an *equation of state* (EoS). An equation of state is a function describing the pressure in terms of density  $\rho$  and internal energy  $e$ , i.e.

$$p = p(\rho, e).$$

The introduction of an equation of state provides the possibility to cover the non-linearity for larger strains and strain rates. Hence, we will apply Hooke's law in the following only to the deviatoric part  $S$  according to equation (1.15). The pressure will be computed by an equation of state specified in Section 1.3 and in more detail in Section 2.1.2.

The computation of the strain tensor  $\varepsilon_\xi$  requires the knowledge of the undeformed reference configuration and of the motion  $X$ . These are assumptions which can not be guaranteed in general.

- The strain tensor  $\varepsilon_\xi$  is given with respect to coordinates attached to the usually unknown reference configuration. In particular, in a time discretized numerical scheme the body is in most cases deformed at the beginning of each time step.
- Even if the undeformed reference configuration is known, this might not be true for the motion  $X$ .

Consider as example the situation sketched in Figure 1.4. We start with an initially undeformed beam given at time  $t_0$ . At time  $t_1$  the beam is bent and

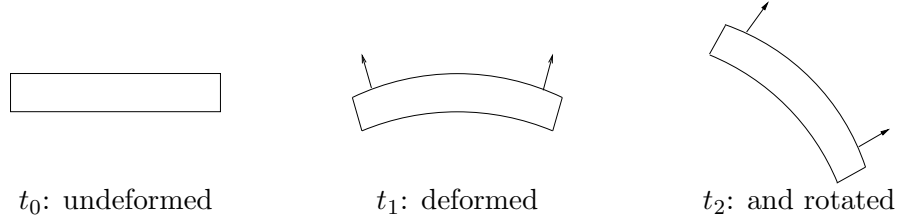


Figure 1.4: Configuration at different states

at time  $t_2$  additionally rotated by some angle. The arrows indicate the main stresses within the body.

If we choose the reference configuration as the undeformed beam at time  $t_0$  the strain is computed correctly for  $t_1$  and  $t_2$ . Hence, the stress tensor describes the behavior of the solid correctly.

On the other hand, if we take the deformed beam at time  $t_1$  as reference configuration Hooke's law fails. The motion from  $t_1$  to  $t_2$  is rigid. Hence, the Green-St.Venant strain tensor remains unchanged while the linearized one yields the wrong strain. This means that equation (1.15) is not able to take the initial deformation into account.

### 1.2.3 Evolution of the Stress Tensor

The key to avoid the problems described above is the introduction of additional equations to the conservation laws. We have seen that we cannot compute the stress directly by equation (1.13). Instead, we will use equation (1.15) for the deviatoric part of the stress tensor to establish equations describing its update. Recall that

$$S = 2\mu \left( \varepsilon_\xi - \frac{1}{3} \text{trace}(\varepsilon_\xi) I \right).$$

We note that

$$\frac{\partial \mathbf{u}(\boldsymbol{\xi}, t)}{\partial t} = \frac{\partial}{\partial t} (X(\boldsymbol{\xi}, t) - \boldsymbol{\xi}) = \frac{\partial X(\boldsymbol{\xi}, t)}{\partial t} = \mathbf{v}(\boldsymbol{\xi}, t)$$

and hence, we are able to define the *strain rate tensor*  $\dot{\varepsilon}_\xi$  by

$$\dot{\varepsilon}_\xi := \frac{\partial \varepsilon_\xi}{\partial t} = \frac{1}{2} (\nabla_\xi \mathbf{v} + (\nabla_\xi \mathbf{v})^T). \quad (1.17)$$

At this point it seems natural to define the update of the deviatoric part of the stress tensor by simply taking the time derivative of equation (1.15), i.e.

$$\frac{\partial S}{\partial t} = 2\mu \left( \dot{\varepsilon}_\xi - \frac{1}{3} \text{trace}(\dot{\varepsilon}_\xi) I \right), \quad (1.18)$$

but this will not solve our previously discussed problems, i.e. that the equation does not cover the situation when starting with an already deformed configuration.

**Remark 1.6** *Considering the update of the deviatoric stress has the advantage that we do not need to compute the displacement field  $\mathbf{u}$ . Instead, we express the stress relation in terms of the velocity. This approach does not work with the Green-St. Venant strain tensor since in this case, the derivative of  $C$  with respect to time still includes the displacement.*

Note that the strain rate tensor is the symmetric part of  $\nabla_\xi \mathbf{v}$ . The velocity gradient can be split into a symmetric and a skew-symmetric part:

$$\nabla_\xi \mathbf{v} = \frac{1}{2} (\nabla_\xi \mathbf{v} + (\nabla_\xi \mathbf{v})^T) + \frac{1}{2} (\nabla_\xi \mathbf{v} - (\nabla_\xi \mathbf{v})^T) .$$

We call the skew-symmetric part the *rotation rate matrix* and define it by

$$R_\xi := \frac{1}{2} (\nabla_\xi \mathbf{v} - (\nabla_\xi \mathbf{v})^T) . \quad (1.19)$$

**Remark 1.7** *In Remark 1.5 we have observed that the linearized strain tensor  $\varepsilon_\xi$  is not equal to zero in a pure rotation. However, one can easily show that the strain rate tensor  $\dot{\varepsilon}_\xi$  remains zero in this case.*

Considering the update of the stress tensor given by equation (1.18) circumvents the restriction of not knowing the stress-free reference configuration. But existing stresses are not considered in a pure rotation since  $\dot{\varepsilon}_\xi$  is equal to zero. That means that we have to modify equation (1.18) by some correction terms motivated by the following consideration.

In a pure rotation, an arbitrary vector  $\phi$  obeys the differential equation

$$\frac{\partial \phi}{\partial t} = R_\xi \phi ,$$

where  $R_\xi$  is the rotation rate matrix. Applying the same to the vector  $\phi = S\mathbf{m}$  gives

$$\begin{aligned} \frac{\partial(S\mathbf{m})}{\partial t} &= R_\xi(S\mathbf{m}) \\ &= \frac{\partial S}{\partial t} \mathbf{m} + S \frac{\partial \mathbf{m}}{\partial t} = \frac{\partial S}{\partial t} \mathbf{m} + SR_\xi \mathbf{m} \end{aligned}$$

with arbitrary vector  $\mathbf{m}$ . Since this is true for any vector we conclude that

$$\frac{\partial S}{\partial t} = R_\xi S - SR_\xi .$$

This term describes the change of the deviatoric stress in a pure rotation and will be discussed further in Section 5.3. Hence, we find that

$$\frac{\partial S}{\partial t} = 2\mu \left( \dot{\varepsilon}_\xi - \frac{1}{3} \text{trace}(\dot{\varepsilon}_\xi) I \right) + \left( R_\xi S - SR_\xi \right) \quad (1.20)$$

is an adequate relation for the description of the evolution of the stress.

- The first term on the right hand side describes the effects “inside” the body.
- The second term rotates the stress tensor and is called the *Jaumann rate* (see [14]).

**Convention** *From now on, we will switch back to the notation used in Section 1.1, where  $\hat{\cdot}$  denotes functions given with respect to material coordinates.*

Both the strain rate tensor  $\dot{\epsilon}_\xi$  and the rotation rate matrix  $R_\xi$  are given in Lagrangian coordinates  $\boldsymbol{\xi}$ . To be consistent with the other equations, we provide  $\dot{\epsilon}$  and  $R$  in actual coordinates  $\mathbf{x}$ . Let  $\hat{\mathbf{u}}(\boldsymbol{\xi}, t)$  and  $\mathbf{u}(\mathbf{x}, t)$  be the displacement in the reference and in the actual configuration, respectively, then

$$\hat{\mathbf{u}}(\boldsymbol{\xi}, t) = \mathbf{u}(X_t(\boldsymbol{\xi}), t)$$

and

$$\frac{\partial \hat{\mathbf{u}}(\boldsymbol{\xi}, t)}{\partial \xi_j} = \frac{\partial \mathbf{u}(X_t(\boldsymbol{\xi}), t)}{\partial \xi_j} = \frac{\partial \mathbf{u}(\mathbf{x}, t)}{\partial x_i} \frac{\partial X_{t_i}(\boldsymbol{\xi})}{\partial \xi_j}.$$

We can write

$$\nabla_\xi \hat{\mathbf{u}}(\boldsymbol{\xi}, t) = \nabla_\xi (X_t(\boldsymbol{\xi}) - \boldsymbol{\xi}) = \nabla_\xi X_t(\boldsymbol{\xi}) - I.$$

Hence, if the displacement gradient  $\nabla_\xi \hat{\mathbf{u}}(\boldsymbol{\xi}, t)$  is small, then  $\nabla_\xi X_t(\boldsymbol{\xi})$  is approximately the identity matrix, such that

$$\frac{\partial \hat{\mathbf{u}}(\boldsymbol{\xi}, t)}{\partial \xi_j} \approx \frac{\partial \mathbf{u}(\mathbf{x}, t)}{\partial x_i} \delta_{ij}.$$

We define the strain rate tensor and the rotation matrix analogously to (1.17) and (1.19), respectively, by

$$\dot{\epsilon} = \frac{1}{2} (\nabla \mathbf{v} + (\nabla \mathbf{v})^T) \quad \text{and} \quad (1.21)$$

$$R = \frac{1}{2} (\nabla \mathbf{v} - (\nabla \mathbf{v})^T). \quad (1.22)$$

### 1.3 Final Set of Equations

**Convention** *In the following, we introduce a new notation skipping the hats for functions given with respect to Lagrangian coordinates. To emphasize the fact that the time evolution is given along particle paths, we use the material derivative  $\frac{D}{Dt}$ . The spatial derivatives are computed in the Eulerian frame.*

**Remark 1.8** *The connection between material derivative and the partial derivative with respect to time is then given by*

$$\frac{D}{Dt} f(\mathbf{x}, t) := \frac{\partial}{\partial t} \hat{f}(\boldsymbol{\xi}, t) \Big|_{\boldsymbol{\xi}=X_t^{-1}(\mathbf{x})} = \frac{\partial}{\partial t} f(\mathbf{x}, t) + \mathbf{v}(\mathbf{x}, t) \cdot \nabla f(\mathbf{x}, t) \quad (1.23)$$

as indicated by (1.5) and (1.6).



We are now able to give the complete set of equations describing the dynamics of solid bodies in the elastic regime.

$$\frac{D\rho}{Dt} = -\rho \operatorname{div}(\mathbf{v}) \quad (1.24)$$

$$\frac{D(\rho v_i)}{Dt} + \rho v_i \operatorname{div}(\mathbf{v}) = \frac{\partial \sigma^{ij}}{\partial x_j} \quad (1.25)$$

$$\frac{D(\rho E)}{Dt} + \rho E \operatorname{div}(\mathbf{v}) = \operatorname{div}(\sigma \mathbf{v}) \quad (1.26)$$

$$\frac{DS}{Dt} = 2\mu \left( \dot{\varepsilon} - \frac{1}{d} \operatorname{trace}(\dot{\varepsilon}) I \right) + RS - SR \quad (1.27)$$

where  $\sigma$  is computed by equation (1.16). The pressure  $p$  is computed by an equation of state presented in Section 2.1.2.

**Remark 1.9** *System (1.2) can be written in conservative form. Stress is a surface force which is no conserved quantity. Therefore, the complete system (1.24) - (1.27) cannot be formulated in conservative form.*

For further investigations it is useful to rewrite the set of equations in *primitive variables*, i.e. mass, velocity and pressure together with the stress tensor. In particular, we replace the equation for the total energy  $\rho E$  by an equation for the pressure. Note that

$$\rho E = \rho e + \frac{1}{2} \rho \mathbf{v}^2 \quad \text{and thus} \quad \frac{De}{Dt} = \frac{1}{\rho} \sigma^{ij} \dot{\varepsilon}^{ij}$$

obtained from equation (1.17) and (1.26). At this point we have to apply the equation of state for the pressure  $p = p(\rho, e)$ . We have

$$\frac{Dp}{Dt} = \frac{\partial p}{\partial \rho} \frac{D\rho}{Dt} + \frac{\partial p}{\partial e} \frac{De}{Dt} = c^2 \frac{D\rho}{Dt} + g \frac{De}{Dt}, \quad (1.28)$$

where

$$c^2 := \left. \frac{\partial p}{\partial \rho} \right|_e \quad \text{and} \quad g := \left. \frac{\partial p}{\partial e} \right|_\rho. \quad (1.29)$$

Later we will see that  $c$  is the speed of sound of the volumetric part of the system of equations. We obtain for the primitive variables:

$$\frac{D\rho}{Dt} + \rho \operatorname{div}(\mathbf{v}) = 0 \quad (1.30)$$

$$\frac{Dv_i}{Dt} + \frac{1}{\rho} \frac{\partial p}{\partial x_i} - \frac{1}{\rho} \frac{\partial S^{ij}}{\partial x_j} = 0 \quad (1.31)$$

$$\frac{Dp}{Dt} + \rho c^2 \operatorname{div}(\mathbf{v}) - g \frac{1}{\rho} \sigma^{ij} \dot{\varepsilon}^{ij} = 0 \quad (1.32)$$

$$\frac{DS}{Dt} - 2\mu \left( \dot{\varepsilon} - \frac{1}{d} \operatorname{trace}(\dot{\varepsilon}) I \right) + RS - SR = 0, \quad (1.33)$$

where  $d$  is the space dimension,  $c$  and  $g$  are material coefficients depending on the equation of state and  $\mu$  is the shear modulus. Note that the system is given in a mixed Eulerian-Lagrangian description.

**Convention** *In the following, the terms Eulerian and Lagrangian description refer to the pure Eulerian and the mixed Eulerian-Lagrangian description, respectively.*

Furthermore, we introduce for convenience the differential operator  $\mathcal{L}$  representing system (1.30) - (1.33) in the way that

$$\frac{D\Phi}{Dt} = \mathcal{L}(\Phi) \tag{1.34}$$

where  $\Phi$  is the vector containing the primitive variables.

## Chapter 2

# Hyperbolic Systems

The mathematical models of many processes occurring in real life include partial differential equations. In the previous chapter, we have already presented the equations describing the dynamics of elastic bodies. The systems of differential equations are commonly classified into three different classes, namely *hyperbolic*, *parabolic* and *elliptic systems*.

In order to design an adequate numerical scheme for a set of PDEs it is indispensable to determine the class of the system. In the following, we will show that the system (1.30) – (1.33) is hyperbolic, give some basic properties of that class of systems and motivate the development of our scheme. For a more detailed discussion about hyperbolic systems we refer to [13] and [16].

### 2.1 Classification of Systems of PDEs

We restrict ourselves to partial differential equations of first order in  $d$  space dimensions. We assume that the system of equations is given in *quasi-linear form*, that is

$$\frac{\partial \Phi}{\partial t} + \sum_{k=1}^d \tilde{A}^{(k)}(\Phi) \frac{\partial \Phi}{\partial x_k} = 0, \quad (2.1)$$

where  $\Phi$  is a vector containing the unknowns. This form is called quasi-linear since the *system matrices*  $\tilde{A}^{(k)}$  depend in general on  $\Phi$ . If the matrices are constant then the system is *linear* in the usual sense.

**Convention** *The tilde denotes matrices and functionals of a purely Eulerian description of the system of equations.*

**Definition 2.1 (Characteristic Functional)** For a system of partial differential equations given in quasi-linear form (2.1) we call

$$\tilde{\Sigma}(\mathbf{n}) := \sum_{k=1}^d n_k \tilde{A}^{(k)} \quad (2.2)$$

the characteristic functional of the system.

The functional provides an easy way to determine the class of a system of partial differential equations (see for example [13, IV.1]).

**Definition 2.2 (Hyperbolic Systems)** A system of partial differential equations in quasi-linear form (2.1) with characteristic functional  $\tilde{\Sigma}(\mathbf{n})$  as in (2.2) is called

- hyperbolic, if all eigenvalues of  $\tilde{\Sigma}(\mathbf{n})$  are real and  $\tilde{\Sigma}$  is diagonalizable,
- strictly hyperbolic, if the system is hyperbolic and all eigenvalues of  $\tilde{\Sigma}(\mathbf{n})$  are distinct and
- weakly hyperbolic, if all eigenvalues of  $\tilde{\Sigma}(\mathbf{n})$  are real

for all  $\mathbf{n}$  with  $\|\mathbf{n}\| = 1$ , where  $\|\cdot\|$  is the Euclidean norm.

A short motivation for this definition is given in Section 2.2. The reason for introducing the notation "weakly hyperbolic" will become clear in Section 2.2. Now, we identify the class of the system (1.30) – (1.33).

### 2.1.1 Quasi-linear Form

In order to apply the definition given above we need to rewrite our set of equations in quasi-linear form.

**Convention** From now on, the equations and the development of the numerical scheme will be presented in two space dimensions. Nevertheless, remarks on the extension to three dimensions will be given. Furthermore, the numerical results given in Chapters 6 and 7 are computed fully three-dimensional.

In two space dimensions the quasi-linear form reads

$$\frac{D\Phi}{Dt} + A^{(1)} \frac{\partial \Phi}{\partial x_1} + A^{(2)} \frac{\partial \Phi}{\partial x_2} = 0, \quad (2.3)$$

where  $\Phi$  is the vector

$$\Phi = (\rho, v_1, v_2, p, S^{11}, S^{22}, S^{21})^T. \quad (2.4)$$

The deviatoric part of the stress tensor can be represented by a symmetric two-by-two matrix  $S$ . Because of the symmetry, the equation for  $S^{12}$  is redundant. The system matrices in two dimensions are given by

$$A^{(1)} = \begin{pmatrix} 0 & \rho & 0 & 0 & 0 & 0 & 0 \\ 0 & 0 & 0 & \frac{1}{\rho} & -\frac{1}{\rho} & 0 & 0 \\ 0 & 0 & 0 & 0 & 0 & 0 & -\frac{1}{\rho} \\ 0 & \rho c^2 + \frac{\mu}{\rho}(p - S^{11}) & -\frac{\mu}{\rho}S^{21} & 0 & 0 & 0 & 0 \\ 0 & -\mu & S^{21} & 0 & 0 & 0 & 0 \\ 0 & \mu & -S^{21} & 0 & 0 & 0 & 0 \\ 0 & 0 & -\mu - \frac{1}{2}S^{11} + \frac{1}{2}S^{22} & 0 & 0 & 0 & 0 \end{pmatrix} \quad (2.5)$$

$$A^{(2)} = \begin{pmatrix} 0 & 0 & \rho & 0 & 0 & 0 & 0 \\ 0 & 0 & 0 & 0 & 0 & 0 & -\frac{1}{\rho} \\ 0 & 0 & 0 & \frac{1}{\rho} & 0 & -\frac{1}{\rho} & 0 \\ 0 & -\frac{\mu}{\rho}S^{21} & \rho c^2 + \frac{\mu}{\rho}(p - S^{22}) & 0 & 0 & 0 & 0 \\ 0 & -S^{21} & \mu & 0 & 0 & 0 & 0 \\ 0 & S^{21} & -\mu & 0 & 0 & 0 & 0 \\ 0 & -\mu + \frac{1}{2}S^{11} - \frac{1}{2}S^{22} & 0 & 0 & 0 & 0 & 0 \end{pmatrix} \quad (2.6)$$

where the rows are ordered according to  $\Phi$ .

### 2.1.2 Eigenvalues

Definition 2.2 refers to systems given in a purely Eulerian description. In order to apply this definition to our problem, the following lemma shows the connection between the purely Eulerian and the Lagrangian description of a system of PDEs.

**Lemma 2.1** *Let  $\tilde{\Sigma}$  be the characteristic functional of a hyperbolic system (2.1) and  $\Sigma$  the one of the corresponding system in Lagrangian description. Then*

- $\Sigma$  is diagonalizable with the same eigenvectors as  $\tilde{\Sigma}$ .
- Let  $\tilde{\lambda}_k$  and  $\lambda_k$  be the  $k$ -th eigenvector of  $\tilde{\Sigma}$  and  $\Sigma$ , respectively, then

$$\tilde{\lambda}_k + \mathbf{n} \cdot \mathbf{v} = \lambda_k.$$

*In particular, all eigenvalues of  $\Sigma$  are real iff all eigenvalues of  $\tilde{\Sigma}$  are real.*

*Proof:* We note first that the system matrices are connected by the relation

$$\tilde{A}^{(k)} = A^{(k)} + v_k I$$

and thus

$$\tilde{\Sigma}(\mathbf{n}) = \sum_{k=1}^d n_k \left( \tilde{A}^{(k)} + v_k I \right) = \Sigma(\mathbf{n}) + \sum_{k=1}^d n_k v_k I$$

Let  $L$  be the matrix of left eigenvectors of  $\tilde{\Sigma}$ , i.e.  $L\tilde{\Sigma} = \tilde{\Lambda}L$  with  $\tilde{\Lambda}$  a diagonal matrix containing the eigenvalues of  $\tilde{\Sigma}$ . Then

$$\begin{aligned} L\Sigma(\mathbf{n})L^{-1} &= L\left(\tilde{\Sigma}(\mathbf{n}) - \sum_{k=1}^d n_k v_k I\right)L^{-1} \\ &= \tilde{\Lambda} - \sum_{k=1}^d n_k v_k I = \tilde{\Lambda} - (\mathbf{n} \cdot \mathbf{v}) I, \end{aligned}$$

which concludes the proof. □

The lemma allows to identify the class of the system (1.30) - (1.33) introduced in Chapter 1 simply by computing the characteristic functional

$$\Sigma(\mathbf{n}) = n_1 A^{(1)} + n_2 A^{(2)} \quad (2.7)$$

with matrices (2.5) and (2.6). The eigenvalues of  $\Sigma$  depend on the chosen direction  $\mathbf{n}$  and are given by

$$\begin{aligned} \lambda_{1/2} &= \pm \sqrt{\frac{\mu}{\rho} + \frac{1}{\rho} n_i n_j S^{ij}} \\ \lambda_{3/4} &= \pm \sqrt{c^2 + \frac{\mu}{\rho} - \frac{g}{\rho^2} n_i n_j \sigma^{ij}} \\ \lambda_{5,6,7} &= 0 \end{aligned} \quad (2.8)$$

using Einstein's summation convention, where  $c$  and  $g$  are defined by (1.28) and  $\mu$  is the shear modulus.

**Remark 2.1** *At first sight it is not clear whether all eigenvalues are real or not. In particular, the type seems to change depending on the chosen  $\mathbf{n}$ . Hence, we need some knowledge about the material of interest, that means we need to specify an equation of state.*

There exists a great variety of closure relations depending on the actual requirements. Hiermayer discusses some equations of state (EoS) in [15]. We follow the suggestion of Benz in [3] and present the *Tillotson EoS*, i.e.

$$p(\rho, e) = \left[ a + \frac{b}{\left(\frac{e}{E_0 \eta^2} + 1\right)} \right] \rho e + A\nu + B\nu^2, \quad (2.9)$$

where  $\eta = \frac{\rho}{\rho_0}$ ,  $\nu = \eta - 1$  and  $\rho_0$  is the normal pressure density.  $A$ ,  $B$ ,  $a$ ,  $b$  and  $E_0$  are material-dependent coefficients and  $e$  is the specific internal energy.

**Remark 2.2** *Equation (2.9) is only a part of the full Tillotson EoS as stated in literature. However, the presented equation suffices to cover the elastic regime of the solid.*

	$a$	$b$	$A [N/m^2]$	$B [N/m^2]$	$E_0 [m^2/s^2]$	$\rho_0 [kg/m^3]$
Iron	0.5	1.5	$128 \cdot 10^9$	$105 \cdot 10^9$	$9.5 \cdot 10^9$	7800
Aluminum	0.5	1.63	$75.2 \cdot 10^9$	$65 \cdot 10^9$	$5 \cdot 10^9$	2700

Table 2.1: Tillotson parameters

In most cases, the parameters for the pressure equation are difficult to identify. Table 2.1 shows them for iron and aluminum. The parameters for additional solids can be found in [30].

	$c [m/s]$	$g [kg/m^3]$	$\mu [N/m^2]$	$\sigma_Y [N/m^2]$
Iron	$6.0 \cdot 10^4$	$6.8 \cdot 10^4$	$128 \cdot 10^9$	$2 \cdot 10^7$
Aluminum	$6.2 \cdot 10^4$	$2.5 \cdot 10^4$	$75.2 \cdot 10^9$	$2 \cdot 10^8$

Table 2.2: Magnitude of parameters

Table 2.2 shows the approximate magnitudes of  $c$ ,  $g$  and the yield stress  $\sigma_Y$  for iron and aluminum, taken from [50]. Computing the eigenvalues by (2.8) together with the above parameters we find that all eigenvalues are real independently of the direction  $\mathbf{n}$ . Furthermore, the characteristic functional  $\Sigma$  of the system is diagonalizable. Hence, we can conclude the following:

The system of partial differential equations (1.30) - (1.33) is **hyperbolic** in the elastic regime.

However, we note that the size of the eigenvalues themselves depends very well on  $\mathbf{n}$ . *The eigenvalues of the three-dimensional system are real in the elastic regime, too.*

## 2.2 Properties of Hyperbolic Systems

In this section we mention some basic properties of hyperbolic systems to motivate the development of a new numerical scheme. For a more detailed introduction to the theory of hyperbolic systems we refer to [13], [16] and others.

### 2.2.1 Propagation of Information

In a hyperbolic system information spreads out with a finite speed of propagation. In general, this speed depends on the direction under consideration. To

illustrate this point, we define for a given direction  $\mathbf{n} \in \mathbb{R}^d$  with  $\|\mathbf{n}\| = 1$  and a scalar  $\omega \in \mathbb{R}$  the function  $\Phi(t, \mathbf{x})$  by

$$\Phi(t, \mathbf{x}) = \hat{\Phi} e^{is(t, \mathbf{x})} \quad \text{with} \quad s(t, \mathbf{x}) = \mathbf{n} \cdot \mathbf{x} - \omega t, \quad (2.10)$$

where  $i$  is the complex unit and  $\hat{\Phi}$  some arbitrary vector. Since  $\omega$  is real, the function  $\Phi$  defines a plane wave running in direction  $\mathbf{n}$  with speed  $\omega$ . If we plug this function into the quasi-linear system (2.1), we find that

$$ie^{is(t, \mathbf{x})} \left( -\omega I + \sum_{k=1}^d n_k \tilde{A}^{(k)} \right) \hat{\Phi} = 0.$$

That means if  $\Phi(t, \mathbf{x})$  solves the system then  $\omega$  needs to be an eigenvalue of the characteristic functional  $\tilde{\Sigma}(\mathbf{n})$ . From this we conclude some important facts.

- The characteristic functional has a finite number of eigenvalues. Hence, system (2.1) allows only a finite number of waves running in direction  $\mathbf{n}$ .
- The eigenvalues of  $\tilde{\Sigma}(\mathbf{n})$  and thus the speed of propagation of information depend on the direction  $\mathbf{n}$ .
- Information spreads out from each point in every direction with a finite speed. Hence, the point influences only a bounded domain in finite time.
- A point  $P$  is influenced by all points in the bounded *domain of dependence* as sketched in Figure 2.1.

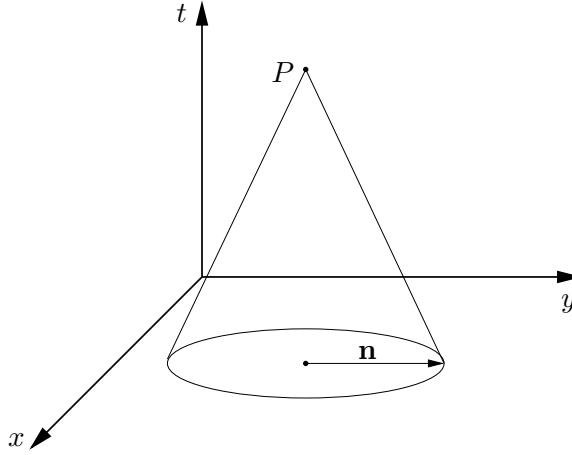


Figure 2.1: Domain of dependence

Figure 2.1 presents the situation for two space dimensions. The values at point  $P$  in the phase-space are influenced only by points lying inside the cone. The size of the cone depends on the eigenvalues of the characteristic functional.

**Remark 2.3** *From the ansatz (2.10) we get a good motivation for the classification of hyperbolic systems. If one eigenvalue  $\lambda$  of  $\Sigma(\mathbf{n})$  would be complex then the corresponding  $\Phi(t, \mathbf{x})$  would either decay or grow exponentially and thus would not describe a plane wave.*



### 2.2.2 Characteristic Variables

In order to do some further investigations, we now present an alternative formulation of the system (2.1).

For a quasi-linear system, the eigenvectors of  $\tilde{\Sigma}(\mathbf{n})$  depend in general on the direction  $\mathbf{n}$  and the primitive variables  $\Phi$ .

**Definition 2.3 (Characteristic Variable)** *Let  $l_\alpha$  be the left eigenvectors of  $\tilde{\Sigma}(\mathbf{n})$  corresponding to eigenvalues  $\lambda_\alpha$ . Furthermore, let  $\partial$  be any variation. Then*

$$\partial w^{(\alpha)} := l_\alpha \partial \Phi \quad \forall \alpha \quad (2.11)$$

*defines a new set of variables, the so-called characteristic variables.*

Since  $l_\alpha$  depends on the unknowns  $\Phi$  it is not clear whether  $w^{(\alpha)}$  exists in general. If the system (2.1) is linear then  $l_\alpha$  is constant and the characteristic variables are given by

$$w^{(\alpha)} = l_\alpha \Phi.$$

**Definition 2.4 (Characteristic System)** *Let (2.1) be hyperbolic and assume that the characteristic variables (2.11) exist for all eigenvectors  $l_\alpha$ . Furthermore, let  $L(\Phi)$  be the matrix containing all left eigenvectors  $l_\alpha$  and  $\mathbf{w}$  the vector of characteristic variables. Then the characteristic system is defined by*

$$\frac{\partial \mathbf{w}}{\partial t} + \sum_{k=1}^d \bar{A}^{(k)}(\mathbf{w}) \frac{\partial \mathbf{w}}{\partial x_k} = 0, \quad (2.12)$$

where  $\bar{A}^{(k)} := L \tilde{A}^{(k)} L^{-1}$ .

The actual form of the characteristic system depends on the chosen direction  $\mathbf{n}$ . The system matrices  $\bar{A}^{(k)}$  are defined with respect to the characteristic variables to be consistent with system (2.1). Furthermore, we note the following:

- In general, we hope that this approach reduces the coupling between the different equations. Indeed, if the system matrices are simultaneously diagonalizable with the same matrix  $L$  then the characteristic system decouples completely.
- The assumption of hyperbolicity is essential to diagonalize the characteristic functional. For weak hyperbolic systems this approach fails.

Another motivation for the characteristic system is that this approach introduces an explicit dependence on the direction  $\mathbf{n}$  into the system of equations. This fact is important for the development of our scheme and will be discussed in more detail in Chapter 5.

### 2.2.3 Non-smooth Solutions

Hyperbolic systems show another important behavior. The solution of such a system may develop discontinuities, which are generally referred to as *shocks*. This is best shown by the following little example.

Consider for a fixed  $c \in \mathbb{R}^+$  the scalar equation

$$\psi_t + c\psi_x = 0 \quad (2.13)$$

in  $\mathbb{R}$  with initial condition

$$\psi(0, x) = \psi_0(x) = \begin{cases} 1 & \text{for } x \leq \psi_l \\ 0 & \text{for } x > \psi_r \end{cases}$$

with  $\psi_l > \psi_r$  as sketched in Figure 2.2.

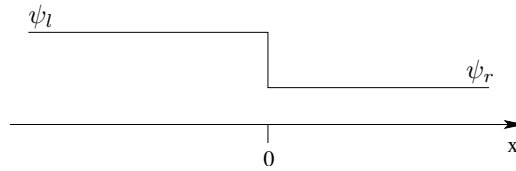


Figure 2.2: Initial condition  $\psi_0$

The solution of the problem is given by  $\psi(t, x) = \psi_0(x - ct)$  and thus the initial profile is simply transported along the  $x$ -axis. That means, the jump in initial data will not be smeared out and the shock will propagate to the right with speed  $c$ . The equation has no viscous term which could smoothen out the jump.

Even for smooth initial data shocks may form in time. The standard example for this is the inviscid Burgers equation

$$u_t + uu_x = 0 \quad \text{with} \quad u(0, x) = u_0(x)$$

which may develop shocks for monotonously decreasing initial condition  $u_0(x)$  (e.g. [13]).

## 2.3 Numerical Treatment of Hyperbolic Systems

The previously described properties of hyperbolic systems lead to special demands on numerical schemes. Consider again equation (2.13) with initial value  $\psi_0$ . Let us examine the finite difference scheme

$$\frac{\psi(x, t+k) - \psi(x, t)}{k} + c \frac{\psi(x+h, t) - \psi(x, t)}{h} = 0, \quad (2.14)$$

where  $k$  and  $h$  are the time and the space discretization, respectively. Let  $t = nk$  and  $\lambda = k/h$ . Then the solution of (2.14) at time  $t$  is given by

$$\psi(x, t) = \sum_{m=0}^n \binom{n}{m} (1 + \lambda c)^m (-\lambda c)^{n-m} \psi_0(x + (n - m)h). \quad (2.15)$$

That means the domain of dependence of  $\psi(x, t)$  is the set of points  $x, x + h, \dots, x + nh$ . For the differential equation (2.13), the domain of dependence of  $\psi$  at point  $(x, t)$  is exactly the point  $\tilde{x} := x - ct$  on the  $x$ -axis. Hence, we do not expect convergence to the true solution since the domain of dependence of the exact equation is not covered by the stencil of the finite difference scheme.

Furthermore, John shows in [20] that errors in  $\psi_0$  of order  $\epsilon$  can lead to an error in  $\psi(x, t)$  which grows exponentially with the number of time steps.

Consider now a finite difference scheme using a backward difference for the spatial derivative instead:

$$\frac{\psi(x, t + k) - \psi(x, t)}{k} + c \frac{\psi(x, t) - \psi(x - h, t)}{h} = 0 \quad (2.16)$$

The domain of dependence of  $\psi(x, t)$  now consists of the set of points  $x, x - h, \dots, x - nh$ . Letting  $k, h \rightarrow 0$  for fixed  $\lambda$  the domain of dependence tends to the interval  $K := [x - (t/\lambda), x]$ . Hence,  $\tilde{x}$  lies within  $K$  if the CFL-condition

$$\lambda c \leq 1 \quad (2.17)$$

is satisfied. Under assumption (2.17) a maximum error of  $\epsilon$  in  $\psi_0$  results in an error of order  $\epsilon$  in  $\psi(x, t)$ . For a more detailed discussion we refer to [20].

The CFL-condition is a necessary condition for the stability of an explicit time integration method. It is named after the mathematicians Courant, Friedrichs and Lewy and requires that the domain of dependence of a partial differential equation lies within the stencil of the numerical scheme.

From this we conclude that even in this simple example a naive approach may lead to an instable scheme. Hence, for any hyperbolic system the propagation of information needs to be investigated in order to successfully design a numerical scheme.

**Remark 2.4** *The situation changes tremendously if we try to extend this concept to higher space dimensions. The problems arising in this case are already adumbrated in Section 2.2.1. We have seen that the values of the quantities are influenced by the whole domain of dependence. In other words information can reach a point from an infinite number of directions.*

However, in a numerical scheme it is not possible to cover this infinite number of directions. In Section 5.1 we present an idea of Deconinck *et al.* described in [7] to single out directions which have some importance for the system of equations in the sense of Definition 5.1 on page 51.



## Chapter 3

# The Finite Pointset Method

In this chapter we present the derivation of the *Finite Pointset Method* (FPM) as introduced by Kuhnert in [24]. We start from a classical particle method (SPH) and point out some disadvantages to motivate FPM. The basic ideas of SPH are presented following Vila as given in [46].

### 3.1 Classical Smoothed Particle Hydrodynamics

The *Smoothed Particle Hydrodynamics* method (SPH) was invented by Gingold and Monaghan in [12] and Lucy in [29] to model astrophysical problems. Since then SPH has been applied to a broad range of physical processes among which we mention high velocity impacts considered by Benz and Asphaug in [2].

#### 3.1.1 Particle Approximation of Functions

In classical methods for solving partial differential equations, the computational domain is discretized by a fixed grid. *Meshless* or *particle methods* have no underlying mesh. Instead of a fixed grid, the domain is discretized by a set of particles moving with the velocity field.

Consider a set of particles  $(\mathbf{x}_i(t), w_i(t))_{i \in P}$ , where  $\mathbf{x}_i(t)$  and  $w_i(t)$  are position and weight of particle  $i$  at time  $t$ , respectively, and  $P$  is an index set of all particles. The particles are moved with the velocity field  $\mathbf{v}$ . The weights represent the volume assigned to each particle and are modified according to deformations due to the velocity field. We have

$$(i) \quad \frac{d\mathbf{x}_i}{dt} = \mathbf{v}(\mathbf{x}_i, t) \quad \text{and} \quad (ii) \quad \frac{dw_i}{dt} = \text{div}(\mathbf{v}(\mathbf{x}_i, t))w_i. \quad (3.1)$$

The mass of particle  $i$  is given by  $m_i = w_i \rho_i$ . The *particle approximation*  $\Pi$  of a function  $f$  is defined as

$$\Pi(f)(x) = \sum_{i \in P} w_i(t) f(\mathbf{x}_i(t)) \delta(\mathbf{x} - \mathbf{x}_i(t))$$

which relates to a quadrature rule in  $\mathbb{R}^d$  with weights  $w_i$ . Note that this formula is to be understood in a distributional sense to give meaning to the Dirac- $\delta$ -distribution. Introducing a smoothing kernel  $W(\mathbf{x}, h)$  we can formulate the *smoothed particle approximation*  $\Pi^h$  of  $f$

$$\Pi^h(f)(x) = \sum_{i \in P} w_i(t) f(\mathbf{x}_i(t)) W(\mathbf{x} - \mathbf{x}_i(t), h) = \Pi(f) * W, \quad (3.2)$$

where  $h$  is the so-called *smoothing length*. We require that  $W(\mathbf{x}, t)$  tends to the Dirac- $\delta$ -distribution as  $h \rightarrow 0$  in a weak sense and that

$$\int_{\mathbb{R}^d} W(\mathbf{x}, h) d\mathbf{x} = 1.$$

In most cases  $W$  is Gaussian-like with compact support such that the value of  $f$  at position  $\mathbf{x}$  is approximated using only neighboring particles. Gradients can easily be approximated by shifting the derivatives to the kernel, that is

$$\nabla \Pi^h(f)(\mathbf{x}_i) = \sum_{j \in P} w_j(t) f(\mathbf{x}_j(t)) \nabla W_{ij},$$

where we introduced the abbreviation  $W_{ij} := W(\mathbf{x}_i - \mathbf{x}_j, h)$ . For a detailed discussion about SPH we refer to any standard work on this field, e.g. [12] and [29]. For approximation results in particular we recommend the work of Vila in [46].

At this stage we will not present the formulation of an actual system of partial differential equations in the SPH framework. Instead, we make some remarks about limitations of the classical SPH method to motivate the development of enhanced schemes.

### 3.1.2 Limitations of SPH

Many numerical methods have been developed to solve specific physical or technical problems. The application to a wider range of problems very often requires the enhancement of the methods to meet the changing demands. Limitations of the classical SPH lie in the following fields.

#### Partition of Unity Method

In this context we call a method a *partition of unity method* if it reproduces constant functions correctly. One can easily show that in this sense SPH in its classical formulation is no partition of unity.

The weights  $w_i$  represent the volume occupied by a particle and thus  $w_i = m_i/\rho_i$ . Consider the approximation of the density of particle  $i$

$$\Pi^h(\rho_i) = \sum_{j \in P} w_j W_{ij} \rho_j = \sum_{j \in P} \frac{m_j}{\rho_j} W_{ij} \rho_j$$

on the domain  $\Omega = [x_0, x_n]$ . If we assume that all particles have the same mass  $m$  then we can write

$$\Pi^h(\rho_i) = m \sum_{j \in P} W_{ij}.$$

This shows already that a constant function can not be reproduced at the boundary of the domain as in this case a part of the support of  $W$  lies outside the computational domain.

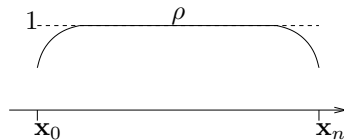


Figure 3.1: Approximation of  $\rho \equiv 1$

In Figure 3.1 the situation is sketched for the case where  $\rho_j = 1$  for all particles. The true solution is constant indicated by the dotted line. The solid line represents the approximation and decreases towards the boundaries. We conclude that the classical SPH is not able to reproduce constant functions on the whole domain. This is true even for an uniform particle distribution as shown in [36].

## Boundary Conditions

Due to the properties near the boundaries, it is difficult to handle boundary conditions in classical SPH. In the original field of application of SPH, namely astrophysics, mostly homogeneous boundary conditions were prescribed, e.g. pressure and temperature equal to zero. These conditions could be approximated well by (3.2).

But in most industrial problems there is the need to prescribe non-homogeneous boundary conditions.

## Adaptivity

The quality of the particle approximation strongly depends on the accuracy of the quadrature rule. To obtain good results it is necessary that a certain number of particles lie within the support of the kernel  $W$ . In some applications this requires the insertion of additional particles or the adaptation of the smoothing kernel.

In SPH this is a difficult task. On the one hand, the particles are physical particles with a certain mass and a volume. Simple insertion or removal of particles violates the conservation properties. On the other hand, the adaptation of the smoothing kernel requires a careful investigation of the approximation properties.

## Tensile Instability

SPH exhibits another unpleasant behavior called *tensile instability*. When a solid is stretched the SPH particles attract each other which can result in a clustering of particles.

This instability was first studied by Swegle *et al.* in [43]. Swegle related the instability to a combination of negative pressure and the sign of the second derivative of the smoothing kernel. Belytschko *et al.* showed in [1] that the tensile instability is basically a peculiarity of so-called *Eulerian kernels*.

### 3.1.3 Related Research on SPH

Many authors have presented ideas to adapt SPH to compensate the described limitations, examples are

- *Variable smoothing length*: Monaghan discusses already in [31] the need for variable smoothing length in case of rarefaction waves. Vila presents new concepts insuring consistency and global conservation properties in [46].
- *Anisotropic smoothing kernel*: The idea behind this approach is to use smoothing kernels adapted to the geometry or the flow. In general this leads to anisotropic kernels, see for example [39].
- *SPH without tensile instability*: In [33] Monaghan recommends to include some artificial stress or pressure to prevent the particles from clustering.
- *Renormalized Hybrid Methods*: Renormalization is a tool recently used to increase the accuracy of SPH. In [47] Vila presents renormalization together with hybrid SPH - Godunov type schemes to achieve robustness.

## 3.2 Finite Pointset Method

In this section we present a different approach developed by Kuhnert in his PhD thesis [24] in 1999.

### 3.2.1 Basic Idea and Definitions

The method was meant as a generalization of the classical SPH allowing for a wider range of approximation operators and thus named *General Smoothed Particle Hydrodynamics*.

Later the method was renamed to *Finite Pointset Method* to cope with the fact that the philosophy behind it is completely different from the one for the classical SPH. There are two fundamental differences between the methods:



- In classical SPH a volume and a mass are assigned to each particle which are "physical" in some sense. In contrast to that the particles have no physical meaning in FPM. They are only the nodes of a "grid" moving with the velocity field.
- In SPH the approximation of functions is done using a quadrature rule approximating integrals as described in Section 3.1.1. FPM uses a local least squares approach to establish a smooth approximation of functions.

Now we give some definitions to formulate the least squares approximation of a function  $f$ .

Let  $\Omega(t) \subset \mathbb{R}^d$  be a domain and  $\omega_N := (\mathbf{x}_i(t))_{i \in P}$  a set of particles in  $\Omega(t)$ , where  $P$  is an index set and  $N := |P|$  is the number of particles. Furthermore, let  $\mathcal{P}_d^\nu$  be the set of polynomials of order  $\nu$  over  $\mathbb{R}^d$ , that is

$$\mathcal{P}_d^\nu := \left\{ p : \mathbb{R}^d \rightarrow \mathbb{R} \mid p(\mathbf{x}) = \sum_{|\alpha| \leq \nu} c_\alpha \mathbf{x}^\alpha; c_\alpha \in \mathbb{R}; \mathbf{x} \in \mathbb{R}^d \right\},$$

where  $\alpha$  is a multi-index, and define  $p_{\mathbf{y}} \in \mathcal{P}_d^\nu$  as

$$p_{\mathbf{y}}(\mathbf{x}) = \sum_{|\alpha| \leq \nu} c_\alpha(\mathbf{y})(\mathbf{x} - \mathbf{y})^\alpha.$$

Then we can give the following definition:

**Definition 3.1 (Least squares approximation)**

Let  $\Omega(t)$  and  $\omega_N$  be defined as before. Let  $\mathbf{f} : \mathbb{R}^+ \rightarrow \mathbb{R}^N$  be a vector of real-valued functions  $f_i(t)$ . Furthermore, let  $W^n \in C_0^n(\mathbb{R}^+)$  be a weighting function with

- $0 \leq W^n(r) \leq 1 \quad \forall r \in \mathbb{R}^+$  and  $W^n(r) = 0$  for  $r > 1$
- $\frac{dW^n}{dr} \Big|_{r=0} = 0$  .

Let  $h : \mathbb{R}^+ \times \bar{\Omega} \rightarrow \mathbb{R}^+$  be the smoothing length and define for a fixed time  $\bar{t}$  the normalized distance between  $\mathbf{x}$  and  $\mathbf{y}$

$$r_{\mathbf{y}}(\mathbf{x}) := \left( \frac{\|\mathbf{x} - \mathbf{y}\|}{h(\bar{t}, \mathbf{x})} \right)^2.$$

Then we call  $p_{\mathbf{y}} \in \mathcal{P}_d^\nu$  the local least squares approximation of order  $\nu$  of the vector  $\mathbf{f}(\bar{t})$  in a neighborhood of  $\mathbf{y} \in \bar{\Omega}(\bar{t})$  if it minimizes the functional

$$\mathcal{D} := \sum_{i \in P} |W^n(r_{\mathbf{y}}(\mathbf{x}_i)) [f_i(\bar{t}) - p_{\mathbf{y}}(\mathbf{x}_i)]|^2. \quad (3.3)$$

For the computation of the coefficients of  $p_{\mathbf{y}}$  it is useful to write the minimization problem as

$$\min_{\mathbf{C}} \|\mathbf{A}\mathbf{C} - \mathbf{F}\|^2, \quad (3.4)$$

where  $A_{ij} := W^n(r_{\mathbf{y}}(\mathbf{x}_i))(\mathbf{x}_i - \mathbf{y})^{\alpha_j}$ ,  $\mathbf{C}_j := c_{\alpha_j}(\mathbf{y})$  and  $F_i := W^n(r_{\mathbf{y}}(\mathbf{x}_i))f_i$ . One can easily show that the solution of the minimization problem is

$$\mathbf{C} = (\mathbf{A}^T \mathbf{A})^{-1} \mathbf{A}^T \mathbf{F} \quad (3.5)$$

(see [40]). Note that the solution makes only sense if  $\mathbf{A}^T \mathbf{A}$  is regular. This induces a condition on the minimum number of particles in the neighborhood of  $\mathbf{y}$ . For a detailed discussion we refer to [24].

**Convention** Henceforth  $\Pi(f)(\mathbf{x})$  denotes the least squares approximation of a function  $f$  at position  $\mathbf{x}$ .

### 3.2.2 Alternative Minimization Problem

For the practical computation of the least squares approximation of a function  $\mathbf{f}$  with discrete function values  $f_j$  at  $\mathbf{x}_j$ , we present an alternative formulation of the minimization problem (3.4). We have

$$\Pi(\mathbf{f})(\mathbf{x}_i) = p_{\mathbf{x}_i}(\mathbf{x}_i) = c_0(\mathbf{x}_i), \quad (3.6)$$

where  $\Pi(\mathbf{f})(\mathbf{x}_i)$  is the least squares approximation of  $\mathbf{f}$  at point  $\mathbf{x}_i$ .  $c_0(\mathbf{x}_i)$  is simply the first entry of the solution  $\mathbf{C}$  of (3.5) established for the point  $\mathbf{y} = \mathbf{x}_i$ . But this we can write as

$$c_0(\mathbf{x}_i) = \sum_{j=1}^N d_{ij} F_j \quad (3.7)$$

with suitable  $d_{ij}$ . For the following we introduce the abbreviation  $W_{ij} := W^n(r_{\mathbf{x}_i}(\mathbf{x}_j))$ .

**Convention** Henceforth we restrict ourselves to polynomials of order one, i.e.  $p_{\mathbf{y}} \in \mathcal{P}_d^1$ . We solve for the coefficients  $c_k(\mathbf{x}_i)$  in

$$p_{\mathbf{x}_i}(\mathbf{x}_j) = c_0(\mathbf{x}_i) + \sum_{k=1}^d c_k(\mathbf{x}_i) \left( x_j^{(k)} - x_i^{(k)} \right),$$

where  $x_j^{(k)}$  is the  $k$ -th component of  $\mathbf{x}_j$  and  $d$  the space dimension.

**Lemma 3.1** The least squares approximation (3.6) of a function  $f$  at point  $\mathbf{x}_i$  given by the minimization problem (3.4) is equivalent to the problem

$$\min_{d_{ij}} \sum_{j=1}^N \left( d_{ij} \right)^2 \quad (3.8)$$

subjected to

$$\sum_{j=1}^N (W_{ij} d_{ij}) = 1 \quad \text{and} \quad (3.9)$$

$$\sum_{j=1}^N (W_{ij} d_{ij} (x_j^{(k)} - x_i^{(k)})) = 0 \quad \forall k = 1, \dots, d \quad (3.10)$$

for a fixed particle  $i$ .

That means the  $d_{ij}$  computed by (3.7) and (3.8), respectively, are the same. The proof of the lemma is technical and will be given in Appendix A.

**Remark 3.1** *Note that the coefficients  $d_{ij}$  depend only on the geometrical arrangement of the particles, not on the discrete function values  $f_j$ . Furthermore, the lemma extends to higher order polynomials with appropriate additional constraints.*

Later in the numerical scheme we rather solve the minimization problem (3.8) than (3.4) for the computation of the least squares approximation.

**Remark 3.2** *Solving the minimization problem (3.4) with first order polynomials or equivalently solving (3.8) leads to a first order method.*

Derivatives of functions can easily be approximated from (3.6) and (3.7). Recall that

$$\Pi(f)(\mathbf{x}_i) = c_0(\mathbf{x}_i) = \sum_{j=1}^N d_{ij} F_j = \sum_{j=1}^N d_{ij} W_{ij} f_j$$

such that

$$\nabla \Pi(f)(x_i) = \sum_{j=1}^N \nabla (d_{ij} W_{ij}) f_j, \quad (3.11)$$

where  $\nabla (d_{ij} W_{ij})$  can be computed analytically. We make the following observations:

- From Lemma 3.1 we conclude that FPM is a partition of unity method. Equation (3.9) can be viewed as approximation of discrete function values  $f_j \equiv 1$  for all  $j$ . The constraint forces that the approximation is also equal to one. Hence, constant functions are represented correctly.
- The quality of the approximation does not decrease towards the boundary provided that there are enough particles in the support of  $W^n$ . For that reason boundary conditions can be represented much better than in classical SPH.

- Recall that the particles are only nodes with no physical meaning. This fact together with the kind of approximation operator enables us to add and remove particles easily without violating the conservation properties.

In analogy to (1.34), we define the finite pointset approximation of a system of PDEs

$$\frac{D\Phi}{Dt} = \Pi\mathcal{L}(\Phi). \quad (3.12)$$

In case of linear systems, the particle approximation is given by  $\Pi\mathcal{L}(\Phi) = \mathcal{L}(\Pi(\Phi))$ .

### 3.2.3 Upwinding in FPM

A further feature of FPM is that approximations can be established for any point  $\mathbf{x}$  being not necessarily the position of a particle. This provides the possibility to include upwinding in the approximations.

Consider for fixed  $c \in \mathbb{R}$  the one-dimensional problem

$$\frac{\partial\phi}{\partial t} \pm c \frac{\partial\phi}{\partial x} = 0. \quad (3.13)$$

We have seen in Section 2.3 the need to take the direction into account from which information reaches a certain point. We define the *upwinded particle approximation* of  $\phi$  by

$$\Pi^+\phi(x) := \Pi\phi(x - \delta c) \quad (3.14)$$

$$\Pi^-\phi(x) := \Pi\phi(x + \delta c) \quad (3.15)$$

where  $\delta$  is an upwind offset such that the CFL-condition is fulfilled. The semi-discretization of (3.13) is then given by

$$\frac{\partial\phi}{\partial t} \pm c \frac{\partial}{\partial x} \Pi^\pm\phi = 0.$$

**Remark 3.3** *In terms of Section 2.3 we shift the point where the spatial derivative is approximated towards the domain of dependence of the exact equation.*

In higher dimensions this concept can easily be extended to upwinding in an arbitrary direction  $\mathbf{n}$ , we define

$$\Pi_{\mathbf{n}}^+\phi(\mathbf{x}_i) := \Pi\phi(\mathbf{x}_i - \delta c \mathbf{n}) \quad (3.16)$$

$$\Pi_{\mathbf{n}}^-\phi(\mathbf{x}_i) := \Pi\phi(\mathbf{x}_i + \delta c \mathbf{n}). \quad (3.17)$$

This upwinding with respect to a given direction  $\mathbf{n}$  is a key ingredient for our numerical scheme given in Chapter 5.

## Chapter 4

# Operator Splitting

There are several reasons to apply an *operator splitting* to a system of partial differential equations. One motivation is to transform a multi-dimensional system into a number of one-dimensional subsystems. This is done in the so-called *dimensional splitting* or *method of fractional steps* as described for example in [27]. A further reason is to split the system up according to different physical processes, e.g. convection-diffusion equations where the transport term is treated separately from the diffusive part (see [22]). In particular in the context of hyperbolic systems, we refer to Crandall and Majda who studied operator splittings in case of shocks in [6].

The motion of an elastic body is the superposition of a rigid body movement and deformations enabled by elasticity. These motions are results of internal and external forces and take place on different time scales in general. To take this fact into account, we split the original system up into subsystems according to different physical processes.

However, we start by presenting the basic ideas of the operator splitting in Eulerian coordinates. After that, we provide a splitting of the system (1.30) – (1.33) and give some remarks on Lagrangian coordinates.

### 4.1 Operator Splitting in Eulerian Description

We restrict ourselves to systems of partial differential equations in quasi-linear form. In this case, operator splitting means that the system matrices are split up according to some physical or numerical needs. Consider the vector-valued function  $\mathbf{u} = \mathbf{u}(t, x)$  and the one dimensional linear system

$$\frac{\partial \mathbf{u}}{\partial t} + A \frac{\partial \mathbf{u}}{\partial x} = 0 \quad \text{with} \quad \mathbf{u}(0, x) = \mathbf{u}_0(x) \quad (4.1)$$

for constant  $A$ . Provided that the Fourier transform  $\hat{\mathbf{u}}$  of  $\mathbf{u}$  exists we can rewrite the above system as

$$\frac{\partial \hat{\mathbf{u}}}{\partial t} + i\xi A \hat{\mathbf{u}} = 0 \quad \text{with} \quad \hat{\mathbf{u}}(0, \xi) = \hat{\mathbf{u}}_0(\xi),$$

where  $\hat{\mathbf{u}}_0(\xi)$  is the Fourier transform of the initial condition  $\mathbf{u}_0(x)$ . By this we have eliminated the spatial derivative and obtain a simple linear system of ordinary differential equations. The solution of the above system at time  $\Delta t$  is given by

$$\hat{\mathbf{u}}(\Delta t, \xi) = e^{-i\xi A \Delta t} \hat{\mathbf{u}}_0(\xi). \quad (4.2)$$

Our aim is not to solve the original system by means of Fourier transformation. We want to investigate how the solution changes if we replace in (4.1) the matrix  $A$  by two matrices  $A_1$  and  $A_2$  such that  $A = A_1 + A_2$ . We have

$$\frac{\partial \hat{\mathbf{u}}}{\partial t} + i\xi A_1 \hat{\mathbf{u}} + i\xi A_2 \hat{\mathbf{u}} = 0$$

and the solution after time  $\Delta t$  is

$$\hat{\mathbf{u}}(\Delta t, \xi) = e^{-i\xi(A_1+A_2)\Delta t} \hat{\mathbf{u}}_0(\xi) = e^{-i\xi A \Delta t} \hat{\mathbf{u}}_0(\xi).$$

This is of course the same as given by (4.2). Now let us consider the two systems

$$\begin{aligned} \text{(i)} \quad & \frac{\partial \mathbf{u}^{(1)}}{\partial t} + A_1 \frac{\partial \mathbf{u}^{(1)}}{\partial x} = 0 \quad \text{with} \quad \mathbf{u}^{(1)}(0, x) = \mathbf{u}_0^{(1)}(x) \\ \text{(ii)} \quad & \frac{\partial \mathbf{u}^{(2)}}{\partial t} + A_2 \frac{\partial \mathbf{u}^{(2)}}{\partial x} = 0 \quad \text{with} \quad \mathbf{u}^{(2)}(0, x) = \mathbf{u}_0^{(2)}(x). \end{aligned}$$

Let  $\mathbf{u}_0^{(1)}(x)$  be equal to the initial value of the original system (4.1), that is

$$\mathbf{u}_0^{(1)}(x) = \mathbf{u}_0(x),$$

and consider the Fourier transform of system (i). Then we find that the solution after time  $\Delta t$  is given by

$$\hat{\mathbf{u}}^{(1)}(\Delta t, \xi) = e^{-i\xi A_1 \Delta t} \hat{\mathbf{u}}_0^{(1)}(\xi) = e^{-i\xi A_1 \Delta t} \hat{\mathbf{u}}_0(\xi). \quad (4.3)$$

Integrating the Fourier transform of system (ii) using  $\hat{\mathbf{u}}_0^{(2)}(\xi) = \hat{\mathbf{u}}^{(1)}(\Delta t, \xi)$  gives

$$\begin{aligned} \hat{\mathbf{u}}^{(2)}(\Delta t, \xi) &= e^{-i\xi A_2 \Delta t} \hat{\mathbf{u}}_0^{(2)}(\xi) \\ &= e^{-i\xi A_2 \Delta t} \hat{\mathbf{u}}^{(1)}(\Delta t, \xi) \\ &= e^{-i\xi A_2 \Delta t} e^{-i\xi A_1 \Delta t} \hat{\mathbf{u}}_0^{(1)}(\xi) \\ &= (e^{-i\xi A_2 \Delta t} e^{-i\xi A_1 \Delta t}) \hat{\mathbf{u}}_0(\xi). \end{aligned} \quad (4.4)$$

If  $A_1$  and  $A_2$  commute then the solution is the same as for the original system (4.1). However, this is not true in general and thus the splitting introduces an error in the time-integration. Indeed, for non-commuting  $A_1$  and  $A_2$  we have

$$\begin{aligned} e^{(A_1+A_2)\Delta t} &= I + (A_1 + A_2) \Delta t + \frac{1}{2}(A_1 + A_2)^2 \Delta t^2 + \mathcal{O}(\Delta t^3) \\ &= I + (A_1 + A_2) \Delta t + \frac{1}{2}(A_1^2 + A_1 A_2 + A_2 A_1 + A_2^2) \Delta t^2 + \mathcal{O}(\Delta t^3), \end{aligned}$$

whereas

$$e^{A_1\Delta t}e^{A_2\Delta t} = I + (A_1 + A_2)\Delta t + \frac{1}{2}(A_1 + 2A_1A_2 + A_2^2)\Delta t^2 + \mathcal{O}(\Delta t^3).$$

This means we make an error of order  $\Delta t^2$ . This error can be reduced by applying the so-called *Strang splitting* as described in [28]. The splitting changes the order of integration and reads

$$e^{\frac{1}{2}A_1\Delta t}e^{A_2\Delta t}e^{\frac{1}{2}A_1\Delta t} = I + (A_1 + A_2)\Delta t + \frac{1}{2}(A_1^2 + A_1A_2 + A_2A_1 + A_2^2)\Delta t^2 + \mathcal{O}(\Delta t^3).$$

Hence, the error is reduced to  $\mathcal{O}(\Delta t^3)$ . A smart alignment of the order of integration can even increase the order of accuracy of the time integration.

**Remark 4.1** *At first sight this method seems to increase the number of evaluations per time step in a numerical scheme. But the Strang splitting is essentially the same as the heuristic splitting with a time-shift of  $\Delta t/2$ . Hence, in a splitting into two subsystems the number of evaluations does not notably increase.*

The Strang splitting can easily be extended to a splitting into three parts. In this case, we note that

$$\begin{aligned} e^{(A_1+A_2+A_3)\Delta t} - e^{A_1\Delta t}e^{A_2\Delta t}e^{A_3\Delta t} &= \mathcal{O}(\Delta t^2) \\ e^{(A_1+A_2+A_3)\Delta t} - e^{\frac{1}{2}A_1\Delta t}e^{\frac{1}{2}A_2\Delta t}e^{A_3\Delta t}e^{\frac{1}{2}A_2\Delta t}e^{\frac{1}{2}A_1\Delta t} &= \mathcal{O}(\Delta t^3). \end{aligned} \quad (4.5)$$

In the present work, we focus on an appropriate approximation of the spatial derivatives. The influence of the sequence of integration of the subsystems is not considered. Moreover, we find it desirable to provide an implementation whose structure is consistent with the one of the existing FPM code as far as possible. Therefore, we apply the most simple order of integration. Nevertheless, higher order time integration concepts might find their application in a future implementation of the method.

## 4.2 Operator Splitting in Lagrangian Description

The presented splitting considers systems in a purely Eulerian description in which the partial differential equations describe the change of physical quantities in actual coordinates. Adequate numerical methods use a mesh fixed in space. In a splitting, the spatial points where the quantities are approximated coincide for all subsystems.

In contrast to that, the Lagrangian formulation (1.30) - (1.33) describes the change of the quantities along the particle paths. FPM takes this into account and moves the particles according to their velocity. This already shows an important problem when combining particle methods with operator splitting.

Applying FPM to the different subsystems, the particles are moved in each system. But in the original unsplit system the particles are moved only once. Additionally, the points where the derivatives are approximated differ for the respective systems and depend on the order in which the splitting is performed. We discuss this aspect in more detail in Section 4.2.2.

*We conclude that there is no natural way to split a system up in a Lagrangian description.*

### 4.2.1 Splitting of the Actual System

We consider the set of equations describing elastic bodies given in quasi-linear form

$$\frac{D}{Dt}\Phi + A^{(1)}\frac{\partial}{\partial x_1}\Phi + A^{(2)}\frac{\partial}{\partial x_2}\Phi = 0,$$

where the system matrices  $A^{(k)}$  are defined in (2.5) and (2.6). We split these matrices up according to rigid body rotation, volume change and shear movements, denoted by  $A_R^{(k)}$ ,  $A_H^{(k)}$  and  $A_S^{(k)}$ , respectively, such that we have

$$A^{(k)} = A_H^{(k)} + A_S^{(k)} + A_R^{(k)} \quad \text{for } k = 1, 2.$$

With the help of these matrices we define the subsystems

$$\begin{aligned} \text{(i)} \quad & \frac{D}{Dt}\Phi^{(H)} + A_H^{(1)}\frac{\partial}{\partial x_1}\Phi^{(H)} + A_H^{(2)}\frac{\partial}{\partial x_2}\Phi^{(H)} = 0 \\ \text{(ii)} \quad & \frac{D}{Dt}\Phi^{(S)} + A_S^{(1)}\frac{\partial}{\partial x_1}\Phi^{(S)} + A_S^{(2)}\frac{\partial}{\partial x_2}\Phi^{(S)} = 0 \\ \text{(iii)} \quad & \frac{D}{Dt}\Phi^{(R)} + A_R^{(1)}\frac{\partial}{\partial x_1}\Phi^{(R)} + A_R^{(2)}\frac{\partial}{\partial x_2}\Phi^{(R)} = 0 \end{aligned} \quad (4.6)$$

with suitable boundary and initial conditions. First of all we present a splitting of the velocity gradient  $\nabla \mathbf{v}$ . We have already defined the strain rate tensor  $\dot{\varepsilon}$  in (1.21) and the rotation rate matrix  $R$  in (1.22). It is well-known that the trace of  $\dot{\varepsilon}$  describes the change of the volume of a body. We define

$$\mathcal{V} := \frac{1}{d}\text{trace}(\dot{\varepsilon}) = \frac{1}{d}\text{div}(\mathbf{v})I$$

as the tensor describing the change of volume and

$$\mathcal{F} := \frac{1}{2}\left(\nabla \mathbf{v} + (\nabla \mathbf{v})^T\right) - \frac{1}{d}\text{div}(\mathbf{v})I$$

as the tensor describing the change of the shape with constant volume. By this we provide a splitting of the gradient of the velocity according to different processes with

$$\nabla \mathbf{v} = \mathcal{F} + R + \mathcal{V}.$$



We know already that  $R$  is skew-symmetric and  $\dot{\varepsilon} = \mathcal{F} + \mathcal{V}$ . Furthermore, from the above definition follows directly that

$$\begin{aligned} R_{ii} &= 0 \quad \forall i, \\ \text{trace}(\mathcal{F}) &= 0, \\ \text{trace}(R) &= 0, \\ \text{trace}(\mathcal{V}) &= \text{div}(\mathbf{v}). \end{aligned}$$

We are now able to rewrite the system of equations in terms of  $R$ ,  $\mathcal{F}$  and  $\mathcal{V}$ :

$$\begin{aligned} \frac{D\rho}{Dt} &= -\rho \text{trace}(\mathcal{V}) \\ \frac{Dv_1}{Dt} &= \frac{1}{\rho} \left( -\frac{\partial p}{\partial x_1} + \frac{\partial S^{11}}{\partial x_1} + \frac{\partial S^{21}}{\partial x_2} \right) \\ \frac{Dv_2}{Dt} &= \frac{1}{\rho} \left( -\frac{\partial p}{\partial x_2} + \frac{\partial S^{21}}{\partial x_1} + \frac{\partial S^{22}}{\partial x_2} \right) \\ \frac{Dp}{Dt} &= -\rho c^2 \text{trace}(\mathcal{V}) - \frac{g}{\rho} p \text{trace}(\mathcal{V}) + g \frac{\sigma^{ij}}{\rho} \mathcal{F}^{ij} \\ \frac{DS}{Dt} &= 2\mu \mathcal{F} + RS - SR. \end{aligned}$$

Note that:

- The equation for the density is clearly assigned to the part describing the change of volume.
- The pressure equation is distributed among the volume and the shear part.
- The equation describing the update of the deviatoric stress tensor contains a shear part and the rotation of the stress.
- The splitting of the velocity gradient does not provide any information on how to split the momentum equation. Anyhow, we assign the pressure gradient to the volume part and the gradient of  $S$  to the shear part.

Hence, the respective subsystems are given by

- **Volumetric part:** Change in volume

$$\frac{D\rho}{Dt} = -\rho \text{div}(\mathbf{v}) \quad (4.7)$$

$$\frac{Dv_i}{Dt} = -\frac{1}{\rho} \frac{\partial p}{\partial x_i} \quad (4.8)$$

$$\frac{Dp}{Dt} = -\rho c^2 \text{div}(\mathbf{v}) \quad (4.9)$$

$$\frac{DS}{Dt} = 0 \quad (4.10)$$

Note that the equations form simply *Euler equations* for an ideal gas plus the deviatoric stress  $S$  which is constant. Remember that  $c$  is the sound speed according to (1.28) and depends on the chosen equation of state.

- **Deviatoric part:** Shear processes

$$\frac{D\rho}{Dt} = 0 \quad (4.11)$$

$$\frac{Dv_i}{Dt} = \frac{1}{\rho} \frac{\partial S^{ij}}{\partial x_j} \quad (4.12)$$

$$\frac{Dp}{Dt} = \frac{g}{\rho} \sigma^{ij} \varepsilon^{ij} \quad (4.13)$$

$$\frac{DS}{Dt} = 2\mu \left( \dot{\varepsilon} - \frac{1}{d} \text{trace}(\dot{\varepsilon}) \right) \quad (4.14)$$

In the pressure equation, we have merged the two parts with factor  $g$  defined by (1.28) using the fact that  $\dot{\varepsilon} = \mathcal{V} + \mathcal{F}$ .

- **Rotation part:** Rotation of the stress tensor

$$\frac{D\rho}{Dt} = 0 \quad (4.15)$$

$$\frac{Dv_i}{Dt} = 0 \quad (4.16)$$

$$\frac{Dp}{Dt} = 0 \quad (4.17)$$

$$\frac{DS}{Dt} = RS - SR \quad (4.18)$$

We see that in this part only the stress tensor is rotated according to the discussion given in Section 1.2.3.

**Remark 4.2** *We have not yet stated the boundary conditions for the respective subsystems. This will be done in Chapter 5. According to the introduced splitting, these conditions have to be split up, too.*

In this context we refer to the work of Hujeirat and Rannacher in the field of astrophysics [17]. There, an operator splitting approach is applied to compressible, highly stratified flows in which the respective equations are integrated successively. In the work, Hujeirat and Rannacher discuss the order of integration and relate it to the governing physical processes. Moreover, they state the general rule for operator splittings that ill-conditioned subsystems should be solved before well-conditioned ones.

For the present work we interpret the statements presented in [17] as follows. The Finite Pointset Method is predestined to solve Euler equations. Various problems from the field of gas-dynamics have successfully been solved by means of this method. Therefore, we propose the following order of integration of the system. First, we solve the shear part, since this is the largest system. Then, we

integrate Euler equations which are well-known since long. Finally, we perform the rotation of the stress tensor. In Chapter 5 we present in detail how the respective subsystems are solved.

In analogy to the differential operator  $\mathcal{L}$  of the full system defined in (1.34) we introduce the operators  $\mathcal{L}_H$ ,  $\mathcal{L}_S$  and  $\mathcal{L}_R$  for the volumetric, deviatoric and rotation part, respectively.

### 4.2.2 Movement of the Particles

According to the previous discussion, we have to specify the motion of the particles. We consider the system of equations in quasi-linear form. In two space dimensions, the Eulerian and the Lagrangian description are given by

$$\frac{\partial \Phi}{\partial t} + \mathbf{v} \cdot \nabla \Phi + A^{(1)} \frac{\partial}{\partial x_1} \Phi + A^{(2)} \frac{\partial}{\partial x_2} \Phi = 0$$

and

$$\frac{D\Phi}{Dt} + A^{(1)} \frac{\partial}{\partial x_1} \Phi + A^{(2)} \frac{\partial}{\partial x_2} \Phi = 0 ,$$

respectively. The two formulations differ only by the transport part  $\mathbf{v} \cdot \nabla \Phi$ . The key to avoid the problem described above is to split this part up in a reasonable way.

#### Heuristic Splitting of the Transport Term

The standard way to do that is to assign the transport part completely to one of the subsystems. In fact, this is done in Chapter 7.

In the previous section we have split the original system (2.3) up into a volumetric, a deviatoric and a rotation part. We consider only one of the systems in a Lagrangian context. There, the particles are moved according to their velocity. The other two subsystems are treated as purely Eulerian systems and hence, the particles are not moved.

#### Other Splittings of the Transport Term

The velocity and thus the movement of the body changes because of different forces acting on the body. Therefore, the velocity can also be interpreted as superposition of different movements. These are rigid body motions, like translation and rotation, and motions due to internal stresses.

An alternative approach is to split the velocity  $\mathbf{v}$  up according to these different movements. It turns out that this is a difficult task since the contributions can not clearly be assigned to the different motions. Therefore, we apply the heuristic splitting of the system in our computations.

### 4.3 Time Integration

In Section 3.2.2 we have stated that our implementation of the finite pointset approximation is only first order. Furthermore, the presented operator splitting has the same order. Therefore, we apply a simple first order explicit time integration method:

$$\Phi^{k+1} = \Phi^k + \Delta t \cdot \Pi\mathcal{L}(\Phi^k), \quad (4.19)$$

where  $\Delta t$  is the time step and  $\Phi^k$  are the discrete values at time  $t = k \cdot \Delta t$ . In particular, we do not apply the Strang splitting presented above. Note that for an explicit method we have to ensure that the CFL-condition holds.

## Chapter 5

# Numerical Method

The Finite Pointset Method is essentially a finite difference method with inherent upwinding in direction of the velocity. In most cases this simple upwinding does not guaranty the stability of a naive scheme. This will be one of the results of Chapter 6. Therefore, each subsystem formulated in Chapter 4.2.1 will be investigated carefully. The insights thereby gained will be used to develop adequate numerical schemes for the respective systems.

**Convention** *In the following we assume constant system matrices for all subsystems indicated by the subscript "0" at the entries. Thereby, we consider linear systems.*

*In this chapter, we occasionally use the notation*

$$v_{x_j}^{(i)} := \frac{\partial v_i}{\partial x_j} \quad \text{and} \quad p_{x_j} := \frac{\partial p}{\partial x_j}$$

*for the velocity and the pressure gradient, respectively.*

### 5.1 Euler Part - Change of Volume

We consider the system (4.7) – (4.10) and rewrite it in quasi-linear form

$$\frac{D\Phi}{Dt} + A_H^{(1)} \frac{\partial \Phi}{\partial x_1} + A_H^{(2)} \frac{\partial \Phi}{\partial x_2} = 0, \quad (5.1)$$

where the system matrices  $A_H^{(i)}$  are given by

$$A_H^{(1)} = \begin{pmatrix} 0 & \rho_0 & 0 & 0 & 0 & 0 & 0 \\ 0 & 0 & 0 & \frac{1}{\rho_0} & 0 & 0 & 0 \\ 0 & 0 & 0 & 0 & 0 & 0 & 0 \\ 0 & \rho_0 c^2 & 0 & 0 & 0 & 0 & 0 \\ 0 & 0 & 0 & 0 & 0 & 0 & 0 \\ 0 & 0 & 0 & 0 & 0 & 0 & 0 \\ 0 & 0 & 0 & 0 & 0 & 0 & 0 \end{pmatrix}, \quad A_H^{(2)} = \begin{pmatrix} 0 & 0 & \rho_0 & 0 & 0 & 0 & 0 \\ 0 & 0 & 0 & 0 & 0 & 0 & 0 \\ 0 & 0 & 0 & \frac{1}{\rho_0} & 0 & 0 & 0 \\ 0 & 0 & \rho_0 c^2 & 0 & 0 & 0 & 0 \\ 0 & 0 & 0 & 0 & 0 & 0 & 0 \\ 0 & 0 & 0 & 0 & 0 & 0 & 0 \\ 0 & 0 & 0 & 0 & 0 & 0 & 0 \end{pmatrix}.$$

This system is at least weakly hyperbolic since the eigenvalues  $\lambda_i$  of the characteristic functional

$$\Sigma_H(\mathbf{n}) = n_1 A_H^{(1)} + n_2 A_H^{(2)}$$

are real for all normalized  $\mathbf{n} = (n_1, n_2)^T$ . We have

$$\begin{aligned} \lambda_{1,\dots,5} &= 0 \\ \lambda_6 &= c \\ \lambda_7 &= -c. \end{aligned} \tag{5.2}$$

**Remark 5.1** *From this, we see that some information travels with the velocity of the body and some with relative speed  $\pm c$ . In particular, the speed of propagation is independent of the direction  $\mathbf{n}$ . Information spreads out in a concentric, spherical way.*

Let  $L_H$  be the matrix containing the left eigenvectors of  $\Sigma_H(\mathbf{n})$  as row-vectors, then

$$L_H = \begin{pmatrix} 1 & 0 & 0 & -\frac{1}{c^2} & 0 & 0 & 0 \\ 0 & -n_2 & n_1 & 0 & 0 & 0 & 0 \\ 0 & 0 & 0 & 0 & 1 & 0 & 0 \\ 0 & 0 & 0 & 0 & 0 & 1 & 0 \\ 0 & 0 & 0 & 0 & 0 & 0 & 1 \\ 0 & n_1 c \rho_0 & n_2 c \rho_0 & 1 & 0 & 0 & 0 \\ 0 & -n_1 c \rho_0 & -n_2 c \rho_0 & 1 & 0 & 0 & 0 \end{pmatrix}. \tag{5.3}$$

$L_H$  is regular with  $\det(L_H) = -2c\rho_0$ . Hence, the Euler system is hyperbolic. To find the characteristic system, we multiply (5.1) from the left by  $L_H$  and obtain

$$\begin{aligned} 0 &= L_H \frac{D\Phi}{Dt} + L_H A_H^{(1)} \frac{\partial \Phi}{\partial x_1} + L_H A_H^{(2)} \frac{\partial \Phi}{\partial x_2} \\ &= L_H \frac{D\Phi}{Dt} + \bar{A}_H^{(1)} L_H \frac{\partial \Phi}{\partial x_1} + \bar{A}_H^{(2)} L_H \frac{\partial \Phi}{\partial x_2} \end{aligned}$$

with

$$\bar{A}_H^{(i)} := L_H A_H^{(i)} L_H^{-1}.$$

Note that  $L_H$  is constant for a given vector  $\mathbf{n}$ . Introducing the characteristic variables  $\mathbf{w}_H = L_H \Phi$ , we can formulate the characteristic system for the Euler part as

$$\frac{D}{Dt} \mathbf{w}_H + \bar{A}_H^{(1)} \frac{\partial}{\partial x_1} \mathbf{w}_H + \bar{A}_H^{(2)} \frac{\partial}{\partial x_2} \mathbf{w}_H = 0, \tag{5.4}$$

where the characteristic variables are given by

$$\mathbf{w}_H = \begin{pmatrix} \rho - \frac{p}{c^2} \\ -n_2 v_1 + n_1 v_2 \\ S^{11} \\ S^{22} \\ S^{21} \\ c\rho_0 \mathbf{n} \cdot \mathbf{v} + p \\ -c\rho_0 \mathbf{n} \cdot \mathbf{v} + p \end{pmatrix}. \tag{5.5}$$

**Remark 5.2** *The deviatoric stress  $S$  is constant in this subsystem. Furthermore, it does not appear in the equations for the remaining quantities. Therefore, we consider in the following a reduced system without the equations for  $S$  and obtain the usual Euler equations in two space dimensions.*

### 5.1.1 Characteristic System for Euler Equations

In 1986 Deconinck *et al.* presented in [7] and [8] an upwind-method for solving Euler equations. In Chapter 2 we have already seen the need to apply an appropriate scheme for hyperbolic systems in order to take the propagation of information into account. In general, information reaches a certain point from any direction. However, in a numerical scheme only a finite number of directions can be considered.

The basic idea of Deconinck is to write the system of equations in characteristic variables and to identify "system-inherent" directions. For the exact definition we refer to Definition 5.1.

In the following, we consider classical Euler equations in the mixed Eulerian-Lagrangian formulation:

$$\frac{D\rho}{Dt} + \rho \operatorname{div}(\mathbf{v}) = 0 \quad (5.6)$$

$$\frac{D\mathbf{v}}{Dt} + \frac{1}{\rho} \nabla p = 0 \quad (5.7)$$

$$\frac{Dp}{Dt} + \rho c^2 \operatorname{div}(\mathbf{v}) = 0. \quad (5.8)$$

Defining  $\Phi_h := (\rho, v_1, v_2, p)^T$ , the quasi-linear system reads

$$\frac{D}{Dt} \Phi_h + A_h^{(1)} \frac{\partial}{\partial x_1} \Phi_h + A_h^{(2)} \frac{\partial}{\partial x_2} \Phi_h = 0$$

with

$$A_h^{(1)} = \begin{pmatrix} 0 & \rho_0 & 0 & 0 \\ 0 & 0 & 0 & \frac{1}{\rho_0} \\ 0 & 0 & 0 & 0 \\ 0 & \rho_0 c^2 & 0 & 0 \end{pmatrix} \quad \text{and} \quad A_h^{(2)} = \begin{pmatrix} 0 & 0 & \rho_0 & 0 \\ 0 & 0 & 0 & 0 \\ 0 & 0 & 0 & \frac{1}{\rho_0} \\ 0 & 0 & \rho_0 c^2 & 0 \end{pmatrix} \quad (5.9)$$

which is simply the reduction of system (5.1). The characteristic functional  $\Sigma_h$  is defined analogously to  $\Sigma_H$  and has eigenvalues

$$\begin{aligned} \lambda_{1,2} &= 0 \\ \lambda_{3,4} &= \pm c. \end{aligned}$$

Let  $l_h^\alpha$  be the associated left eigenvector to the eigenvalue  $\lambda_\alpha$  and  $L_h$  the matrix consisting of  $l_h^\alpha$  as row vectors.

$$L_h = \begin{pmatrix} 1 & 0 & 0 & -\frac{1}{c^2} \\ 0 & -n_2 & n_1 & 0 \\ 0 & n_1 c \rho_0 & n_2 c \rho_0 & 1 \\ 0 & -n_1 c \rho_0 & -n_2 c \rho_0 & 1 \end{pmatrix} \quad (5.10)$$

Then the characteristic variables are

$$\mathbf{w}_h = \begin{pmatrix} \rho - \frac{p}{c^2} \\ \mathbf{s} \cdot \mathbf{v} \\ c\rho_0 \mathbf{n} \cdot \mathbf{v} + p \\ -c\rho_0 \mathbf{n} \cdot \mathbf{v} + p \end{pmatrix}, \quad (5.11)$$

where  $\mathbf{s}$  is normal to  $\mathbf{n}$  and henceforth defined as

$$\mathbf{s} := \begin{pmatrix} -n_2 \\ n_1 \end{pmatrix}.$$

$w_h^{(1)}$  and  $w_h^{(2)}$  are called *entropy waves*, whereas  $w_h^{(3)}$  and  $w_h^{(4)}$  can be interpreted as *sound waves* since they propagate just with the speed of sound  $c$ .

The characteristic system of Euler equations is given by

$$\begin{aligned} \frac{Dw_h^{(1)}}{Dt} &= 0 \\ \frac{Dw_h^{(2)}}{Dt} + \frac{c}{2} \mathbf{s} \cdot \nabla (w_h^{(3)} + w_h^{(4)}) &= 0 \\ \frac{Dw_h^{(3)}}{Dt} + c \mathbf{n} \cdot \nabla w_h^{(3)} + c \mathbf{s} \cdot \nabla w_h^{(2)} &= 0 \\ \frac{Dw_h^{(4)}}{Dt} - c \mathbf{n} \cdot \nabla w_h^{(4)} + c \mathbf{s} \cdot \nabla w_h^{(2)} &= 0. \end{aligned}$$

From (5.11) we see that  $\frac{1}{2}(w_h^{(3)} + w_h^{(4)}) = p$  and  $\mathbf{s} \cdot \nabla w_h^{(2)} = \mathbf{s} \cdot (\mathbf{s} \cdot \nabla) \mathbf{v}$  such that we can rewrite the system as

$$\frac{Dw_h^{(1)}}{Dt} = 0 \quad (5.12)$$

$$\frac{Dw_h^{(2)}}{Dt} + c \mathbf{s} \cdot \nabla p = 0 \quad (5.13)$$

$$\frac{Dw_h^{(3)}}{Dt} + c \mathbf{n} \cdot \nabla w_h^{(3)} + c \mathbf{s} \cdot (\mathbf{s} \cdot \nabla) \mathbf{v} = 0 \quad (5.14)$$

$$\frac{Dw_h^{(4)}}{Dt} - c \mathbf{n} \cdot \nabla w_h^{(4)} + c \mathbf{s} \cdot (\mathbf{s} \cdot \nabla) \mathbf{v} = 0. \quad (5.15)$$

Rewriting the set of equations in characteristic variables introduces an explicit dependence on the direction  $\mathbf{n}$ . In particular, the equations (5.14) and (5.15) have a convection term with transport in direction of  $\mathbf{n}$ .

We have seen in Section 2.2 that the transport terms need a careful treatment in any numerical scheme in order to represent non-smooth solutions correctly. However, let us first define *system-inherent* and make some remarks on the characteristic system.



**Definition 5.1 (System-inherent direction)** *We call a direction  $\mathbf{n}$  system-inherent to a system of PDEs if the corresponding characteristic system yields at least one homogeneous equation more than for an arbitrary direction.*

**Remark 5.3** *In general, finding system-inherent directions for all times is a highly nonlinear problem. However, in a time-discretized scheme the directions will be determined at the beginning of each time step and kept constant.*

In the sense of the above definition, the system (5.12) – (5.15) has two system-inherent directions. Recall that  $\mathbf{s}$  is defined normal to  $\mathbf{n}$ .

1. If  $\mathbf{n}$  is parallel to the pressure gradient, then the source term  $c\mathbf{s} \cdot \nabla p$  of equation (5.13) is equal to zero. Hence, the normalized pressure gradient is a system-inherent direction.
2. If  $\mathbf{s}$  solves the quadratic equation  $\mathbf{s} \cdot (\mathbf{s} \cdot \nabla)\mathbf{v} = 0$ , then the corresponding normal direction  $\mathbf{n}$  is system-inherent.

In general, the direction  $\mathbf{s}$  normal to the pressure gradient does not solve the quadratic equation  $\mathbf{s} \cdot (\mathbf{s} \cdot \nabla)\mathbf{v} = 0$ . Therefore, the source terms do not vanish simultaneously.

We will follow two different approaches. The first one considers the design of a scheme using one single upwind direction. This approach is described in Section 5.1.3. The second one takes both system-inherent directions into account simultaneously, see 5.1.6. For a detailed discussion about the quadratic form  $\mathbf{s} \cdot (\mathbf{s} \cdot \nabla)\mathbf{v}$  we refer to Section 5.1.4.

### 5.1.2 Boundary Conditions

The characteristic system (5.12) - (5.15) provides an easy way to determine the number of boundary values needed to describe a physical problem correctly. Consider the computational domain  $\Omega$  with boundary  $\partial\Omega$ . Let  $\mathbf{x} \in \partial\Omega$  be a

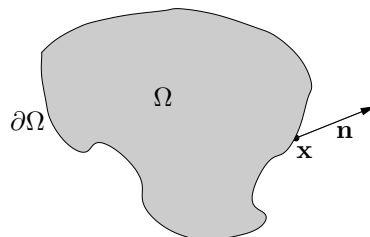


Figure 5.1: Boundary conditions

point on the boundary and  $\mathbf{n}$  an arbitrary vector of length one starting in  $\mathbf{x}$ .

The characteristic system for Euler equations written in  $\mathbf{n}$  has convection terms  $\mathcal{C}_i$  of the form

$$\begin{aligned}\mathcal{C}_3 &= \mathbf{n} \cdot \nabla w_h^{(3)} \\ \mathcal{C}_4 &= -\mathbf{n} \cdot \nabla w_h^{(4)}.\end{aligned}$$

That means independent of the direction  $\mathbf{n}$ , only for one characteristic variable information comes from the outside of the domain. Hence, we need to give one boundary condition on  $\partial\Omega$  for the Euler part.

**Remark 5.4** *It seems natural to fix either  $w_h^{(3)}$  or  $w_h^{(4)}$  at the boundary depending on the direction  $\mathbf{n}$  and the sign of  $c$ . Anyhow, we will equivalently describe either the pressure  $p$  or the normal velocity  $\mathbf{n} \cdot \mathbf{v}$ .*

### 5.1.3 Single Upwind Direction

We have already given the characteristic system for one single direction  $\mathbf{n}$ . Equations (5.14) and (5.15) have a transport term in this direction.

Convection is only in a single direction  $\mathbf{n}$ . Hence, we are able to apply the one-dimensional upwind approach described in 3.2.3. Recall that the upwinded particle approximations (3.16) and (3.17) are defined as

$$\begin{aligned}\Pi_{\mathbf{n}}^+ \phi(\mathbf{x}_i) &= \Pi \phi(\mathbf{x}_i - \delta c \mathbf{n}) \\ \Pi_{\mathbf{n}}^- \phi(\mathbf{x}_i) &= \Pi \phi(\mathbf{x}_i + \delta c \mathbf{n}).\end{aligned}$$

The transport terms in equation (5.14) and (5.15) are approximated by  $\Pi_{\mathbf{n}}^+$  and  $\Pi_{\mathbf{n}}^-$ , respectively. By this we allow for the propagation of information. Furthermore, the central approximations for the non-convective source terms are replaced by

$$\Pi_{\mathbf{n}}^c := \frac{1}{2} (\Pi_{\mathbf{n}}^+ + \Pi_{\mathbf{n}}^-) \quad (5.16)$$

in order to reduce the number of evaluations needed. Hence, the *upwinded finite pointset approximation* of the characteristic system (5.12) - (5.15) is

$$\begin{aligned}\frac{Dw_h^{(1)}}{Dt} &= 0 \\ \frac{Dw_h^{(2)}}{Dt} + c \mathbf{s} \cdot \Pi_{\mathbf{n}}^c \nabla p &= 0 \\ \frac{Dw_h^{(3)}}{Dt} + c \mathbf{n} \cdot \Pi_{\mathbf{n}}^+ \nabla w_h^{(3)} + c \mathbf{s} \cdot \Pi_{\mathbf{n}}^c \nabla w_h^{(2)} &= 0 \\ \frac{Dw_h^{(4)}}{Dt} - c \mathbf{n} \cdot \Pi_{\mathbf{n}}^- \nabla w_h^{(4)} + c \mathbf{s} \cdot \Pi_{\mathbf{n}}^c \nabla w_h^{(2)} &= 0.\end{aligned}$$

Having identified the appropriate approximations for the space derivatives, we are able to transform the system back into primitive variables. The reformulation of the system is done by multiplying the system from the left by  $L_h^{-1}$ . We

obtain

$$\frac{D\rho}{Dt} = -\rho \operatorname{div}(\mathbf{v}_{uw}) \quad (5.17)$$

$$\frac{D\mathbf{v}}{Dt} = -\frac{1}{\rho} \nabla p_{uw} \quad (5.18)$$

$$\frac{Dp}{Dt} = -\rho c^2 \operatorname{div}(\mathbf{v}_{uw}), \quad (5.19)$$

where

$$\frac{\partial v_{uw}^{(i)}}{\partial x_j} := \Pi_{\mathbf{n}}^c v_{x_j}^{(i)} + \frac{1}{\rho_0 c} \left( \frac{\Pi^+ p_{x_j} - \Pi^- p_{x_j}}{2} \right) n_j \quad (5.20)$$

$$\frac{\partial p_{uw}}{\partial x_j} := \Pi_{\mathbf{n}}^c p_{x_j} + c \rho_0 n_j \left( n_i n_k \frac{\Pi^+ v_{x_k}^{(i)} - \Pi^- v_{x_k}^{(i)}}{2} \right) \quad (5.21)$$

with summation over  $i$  and  $k$  in the last equation. For the following we introduce the notion of *upwind velocity*

$$\mathbf{v}_{uw} := \Pi_{\mathbf{n}}^c \mathbf{v} + \frac{1}{\rho_0 c} \left( \frac{\Pi^+ p - \Pi^- p}{2} \right) \mathbf{n} \quad (5.22)$$

and define formally the *upwind pressure*

$$p_{uw} := \Pi_{\mathbf{n}}^c p + \rho_0 c \left( \frac{\Pi^+ \mathbf{v} - \Pi^- \mathbf{v}}{2} \right) \cdot \mathbf{n}. \quad (5.23)$$

Note that the pressure gradient defined by equation (5.21) is the projection of the true gradient of  $p_{uw}$  onto the direction  $\mathbf{n}$ . Furthermore, this system neglects terms of the form

$$\frac{\Pi^+ \phi_{x_i} - 2\Pi \phi_{x_i} + \Pi^- \phi_{x_i}}{2}$$

which are assumed to be small. This assumption is reasonable since we use linear ansatz functions for the least squares approximation as stated in Section 3.2.2.

Both, the upwind velocity and the upwind pressure consist of the central approximation of the quantities plus a correction term due to upwinding. If the pressure and the velocity are constant in space, then the correction terms vanish.

**Convention** For the following, we introduce the notation of the upwinded particle approximation  $\Pi_{uw}^{\mathbf{n}}$  in direction  $\mathbf{n}$  of a system of partial differential equations

$$\frac{D\Phi}{Dt} = \Pi_{uw}^{\mathbf{n}} \mathcal{L}(\Phi). \quad (5.24)$$

This definition extends the particle approximation (3.12) by upwinding of the convection terms.

**Remark 5.5** System (5.17) - (5.19) can be rewritten in conservative variables mass, momentum and total energy. Kuhnert has shown in [24] that the scheme is conservative and stable provided that the particles are moved with the upwind velocity.

### 5.1.4 Minimization of the Quadratic Form

We consider the source term  $\mathbf{s} \cdot (\mathbf{s} \cdot \nabla) \mathbf{v}$  in the equations (5.14) and (5.15). In two space dimensions we may write

$$\begin{aligned} \mathbf{s} \cdot (\mathbf{s} \cdot \nabla) \mathbf{v} &= \mathbf{s} \cdot (\nabla \mathbf{v} \mathbf{s}) \\ &= s_1^2 \frac{\partial v_1}{\partial x} + s_1 s_2 \left( \frac{\partial v_1}{\partial y} + \frac{\partial v_2}{\partial x} \right) + s_2^2 \frac{\partial v_2}{\partial y} \\ &= s_1^2 \dot{\varepsilon}_{xx} + 2s_1 s_2 \dot{\varepsilon}_{xy} + s_2^2 \dot{\varepsilon}_{yy} \end{aligned}$$

using the strain rate tensor  $\dot{\varepsilon}$ . That means we can rewrite the above expression as

$$\mathbf{s} \cdot (\mathbf{s} \cdot \nabla) \mathbf{v} = \mathbf{s}^T \dot{\varepsilon} \mathbf{s} \quad (5.25)$$

which is a quadratic form in  $\mathbf{s}$ . Since  $\dot{\varepsilon}$  is symmetric we find an orthonormal basis (ONB)  $\mathcal{B} = \{\mathbf{b}_1, \mathbf{b}_2\}$  of right eigenvectors (EVs) of  $\dot{\varepsilon}$ . Let  $\lambda_1$  and  $\lambda_2$  be the corresponding eigenvalues. Any vector  $\mathbf{s}$  has a representation

$$\mathbf{s} = \sum \alpha_i \mathbf{b}_i$$

with respect to the basis  $\mathcal{B}$ . Let  $\mathbf{s}$  be an arbitrary vector of length one. Then

$$1 = \|\mathbf{s}\|^2 = \left( \sum \alpha_i \mathbf{b}_i \right) \cdot \left( \sum \alpha_i \mathbf{b}_i \right) \stackrel{ONB}{=} \sum \alpha_i^2$$

and

$$\mathbf{s}^T \dot{\varepsilon} \mathbf{s} = \left( \sum \alpha_i \mathbf{b}_i \right) \cdot \dot{\varepsilon} \left( \sum \alpha_i \mathbf{b}_i \right) \stackrel{EVs}{=} \left( \sum \alpha_i \mathbf{b}_i \right) \cdot \left( \sum \alpha_i \lambda_i \mathbf{b}_i \right)$$

such that

$$\mathbf{s}^T \dot{\varepsilon} \mathbf{s} = \sum \alpha_i^2 \lambda_i \quad \forall \|\mathbf{s}\| = 1. \quad (5.26)$$

Assume that  $\lambda_1 \leq \lambda_2$ . Then

$$\lambda_1 = \alpha_1^2 \lambda_1 + \alpha_2^2 \lambda_1 \leq \alpha_1^2 \lambda_1 + \alpha_2^2 \lambda_2 \leq \alpha_1^2 \lambda_2 + \alpha_2^2 \lambda_2 = \lambda_2$$

and hence, together with (5.26)

$$\lambda_1 \leq \mathbf{s}^T \dot{\varepsilon} \mathbf{s} \leq \lambda_2 \quad \forall \|\mathbf{s}\| = 1.$$

For the minimization problem this has some important consequences:

- Note that  $\mathbf{s}^T \dot{\varepsilon} \mathbf{s}$  can only become zero if the two eigenvalues of  $\dot{\varepsilon}$  have different signs, i.e.  $\lambda_1 \leq 0$  and  $\lambda_2 \geq 0$ , since we assumed that  $\lambda_1 \leq \lambda_2$ .
- In two dimensions we have  $\det(\dot{\varepsilon}) = \lambda_1 \lambda_2$  and hence, the condition that the eigenvalues have different sign is equivalent to  $\det(\dot{\varepsilon}) \leq 0$ .
- If  $\lambda_1$  and  $\lambda_2$  both are positive, we have to take  $\mathbf{s} = \mathbf{b}_1$  the eigenvector corresponding to  $\lambda_1$  to minimize  $|\mathbf{s}^T \dot{\varepsilon} \mathbf{s}|$ . In case that both eigenvalues are negative, we chose  $\mathbf{s} = \mathbf{b}_2$ .

- Hence, the minimum of  $|\mathbf{s}^T \dot{\boldsymbol{\varepsilon}} \mathbf{s}|$  is either zero for  $\det(\dot{\boldsymbol{\varepsilon}}) \leq 0$  or equal to  $\min(|\lambda_1|, |\lambda_2|)$  for  $\det(\dot{\boldsymbol{\varepsilon}}) > 0$ .

We extend the definition of system-inherent directions to directions which minimize the absolute value of the quadratic form  $\mathbf{s}^T \dot{\boldsymbol{\varepsilon}} \mathbf{s}$ .

In case that  $\det(\dot{\boldsymbol{\varepsilon}}) \leq 0$  the solution of  $\mathbf{s}^T \dot{\boldsymbol{\varepsilon}} \mathbf{s} = 0$  is given by

$$\mathbf{s} = \gamma \begin{pmatrix} -\dot{\varepsilon}_{xy} \pm \sqrt{-\det(\dot{\boldsymbol{\varepsilon}})} \\ \dot{\varepsilon}_{xx} \end{pmatrix}$$

where  $\gamma$  is a scaling coefficient to normalize  $\mathbf{s}$ . Here, we see again that the condition  $\det(\dot{\boldsymbol{\varepsilon}}) \leq 0$  is necessary to find an appropriate  $\mathbf{s}$ .

### 5.1.5 Remarks on Three Dimensions

The characteristic system for Euler equations has the same structure as in the two-dimensional case:

$$\begin{aligned} \frac{Dw_h^{(1)}}{Dt} &= 0 \\ \frac{Dw_h^{(2)}}{Dt} + \frac{c}{2} \mathbf{s} \cdot \nabla (w_h^{(4)} + w_h^{(5)}) &= 0 \\ \frac{Dw_h^{(3)}}{Dt} + \frac{c}{2} \mathbf{t} \cdot \nabla (w_h^{(4)} + w_h^{(5)}) &= 0 \\ \frac{Dw_h^{(4)}}{Dt} + c \mathbf{n} \cdot \nabla w_h^{(4)} + c \mathbf{s} \cdot \nabla w_h^{(2)} + c \mathbf{t} \cdot \nabla w_h^{(3)} &= 0 \\ \frac{Dw_h^{(5)}}{Dt} - c \mathbf{n} \cdot \nabla w_h^{(5)} + c \mathbf{s} \cdot \nabla w_h^{(2)} + c \mathbf{t} \cdot \nabla w_h^{(3)} &= 0, \end{aligned}$$

where the equation for  $w_h^{(3)}$  is an additional equation for the third space dimension. The characteristic variables are

$$\mathbf{w}_h = \begin{pmatrix} \rho - \frac{p}{c^2} \\ \mathbf{s} \cdot \mathbf{v} \\ \mathbf{t} \cdot \mathbf{v} \\ c\rho_0 \mathbf{n} \cdot \mathbf{v} + p \\ -c\rho_0 \mathbf{n} \cdot \mathbf{v} + p \end{pmatrix}.$$

In the equations,  $\mathbf{s}$  and  $\mathbf{t}$  denote vectors normal to  $\mathbf{n}$  such that  $\tilde{\mathcal{B}} = \{\mathbf{n}, \mathbf{s}, \mathbf{t}\}$  forms an orthonormal basis of  $\mathbb{R}^3$ . Again  $\frac{1}{2}(w_h^{(4)} + w_h^{(5)}) = p$  such that the equations for  $w_h^{(2)}$  and  $w_h^{(3)}$  reduce to

$$\begin{aligned} \frac{Dw_h^{(2)}}{Dt} + c \mathbf{s} \cdot \nabla p &= 0, \\ \frac{Dw_h^{(3)}}{Dt} + c \mathbf{t} \cdot \nabla p &= 0, \end{aligned}$$

respectively. The source terms in the last two equations of the system can be written as a quadratic form in  $\mathbf{n}$ , namely

$$\mathbf{s} \cdot \nabla w_h^{(2)} + \mathbf{t} \cdot \nabla w_h^{(3)} = \mathbf{n}^T \dot{\mathcal{E}} \mathbf{n} \quad (5.27)$$

where

$$\dot{\mathcal{E}} := \begin{pmatrix} \dot{\epsilon}_{22} + \dot{\epsilon}_{33} & -\dot{\epsilon}_{21} & -\dot{\epsilon}_{31} \\ -\dot{\epsilon}_{21} & \dot{\epsilon}_{11} + \dot{\epsilon}_{33} & -\dot{\epsilon}_{32} \\ -\dot{\epsilon}_{31} & -\dot{\epsilon}_{32} & \dot{\epsilon}_{11} + \dot{\epsilon}_{22} \end{pmatrix}.$$

The above equation forms the analogon of equation (5.25). The quadratic form  $\mathbf{n}^T \dot{\mathcal{E}} \mathbf{n}$  can only become zero if the largest and the smallest eigenvalue of  $\dot{\mathcal{E}}$  have different signs or if at least one eigenvalue is zero.

That means the Euler system in three space dimensions has also two system-inherent directions, namely the pressure gradient and the direction which minimizes the absolute value of  $\mathbf{n}^T \dot{\mathcal{E}} \mathbf{n}$ .

### 5.1.6 Multiple Upwind Directions

We have seen that Euler equations have to system-inherent directions which in general differ. Deconinck proposes in [8] to write the system of equations in a characteristic form depending on two different directions.

Let  $\mathbf{n}$  and  $\mathbf{m}$  be normalized vectors representing two directions. Furthermore, let  $\mathbf{s}$  and  $\mathbf{t}$  be vectors normal to  $\mathbf{n}$  and  $\mathbf{m}$ , respectively, that is

$$\mathbf{n} = \begin{pmatrix} n_1 \\ n_2 \end{pmatrix}, \quad \mathbf{s} = \begin{pmatrix} -n_2 \\ n_1 \end{pmatrix} \quad \text{and} \quad \mathbf{m} = \begin{pmatrix} m_1 \\ m_2 \end{pmatrix}, \quad \mathbf{t} = \begin{pmatrix} -m_2 \\ m_1 \end{pmatrix}$$

and define

$$L_{dec} = \begin{pmatrix} 1 & 0 & 0 & -\frac{1}{c^2} \\ 0 & s_1 & s_2 & 0 \\ 0 & m_1 c \rho_0 & m_2 c \rho_0 & 1 \\ 0 & -m_1 c \rho_0 & -m_2 c \rho_0 & 1 \end{pmatrix}.$$

Note that  $L_{dec}$  is invertible provided that  $\mathbf{n} \cdot \mathbf{m} \neq 0$ . The corresponding characteristic system in two independent directions is

$$\begin{aligned} \frac{Dw_{dec}^{(1)}}{Dt} &= 0 \\ \frac{Dw_{dec}^{(2)}}{Dt} + \frac{1}{\rho} \mathbf{s} \cdot \nabla p &= 0 \\ \frac{Dw_{dec}^{(3)}}{Dt} + c \mathbf{m} \cdot \nabla w_{dec}^{(3)} + c \mathbf{t} \cdot (\mathbf{t} \cdot \nabla) \mathbf{v} &= 0 \\ \frac{Dw_{dec}^{(4)}}{Dt} - c \mathbf{m} \cdot \nabla w_{dec}^{(4)} + c \mathbf{t} \cdot (\mathbf{t} \cdot \nabla) \mathbf{v} &= 0 \end{aligned}$$

with characteristic variables

$$\begin{aligned}
 w_{dec}^{(1)} &= \rho - \frac{p}{c^2} \\
 w_{dec}^{(2)} &= \mathbf{s} \cdot \mathbf{v} \\
 w_{dec}^{(3)} &= c\rho_0 \mathbf{m} \cdot \mathbf{v} + p \\
 w_{dec}^{(4)} &= -c\rho_0 \mathbf{m} \cdot \mathbf{v} + p.
 \end{aligned}$$

By writing the system in this form we are able to choose  $\mathbf{n}$  normal to the pressure gradient and  $\mathbf{m}$  in such a way that  $\mathbf{t}$  minimizes the absolute value of  $\mathbf{t}^T \varepsilon \mathbf{t}$ .

Note that in this case  $\mathbf{n}$  and  $\mathbf{m}$  are the system-inherent directions and all source terms vanish.

**Remark 5.6** *Although the characteristic system is written in two directions, convection is only in direction  $\mathbf{m}$ . Therefore, upwinding needs to be performed only in this single direction. We conclude that for Euler equations it is sufficient to establish the characteristic system for a single direction. Accordingly, results will only be given for one upwind direction in Section 6.1.*

## 5.2 Shear Part

The shear processes inside the body are described by the system (4.11) – (4.14) such that the quasi-linear form has the following system matrices

$$A_S^{(1)} = \begin{pmatrix} 0 & 0 & 0 & 0 & 0 & 0 & 0 \\ 0 & 0 & 0 & 0 & -\frac{1}{\rho_0} & 0 & 0 \\ 0 & 0 & 0 & 0 & 0 & 0 & -\frac{1}{\rho_0} \\ 0 & \frac{g}{\rho_0}(p_0 - S_0^{11}) & -\frac{g}{\rho_0}S_0^{21} & 0 & 0 & 0 & 0 \\ 0 & -\mu & 0 & 0 & 0 & 0 & 0 \\ 0 & \mu & 0 & 0 & 0 & 0 & 0 \\ 0 & 0 & -\mu & 0 & 0 & 0 & 0 \end{pmatrix} \quad (5.28)$$

and

$$A_S^{(2)} = \begin{pmatrix} 0 & 0 & 0 & 0 & 0 & 0 & 0 \\ 0 & 0 & 0 & 0 & 0 & 0 & -\frac{1}{\rho_0} \\ 0 & 0 & 0 & 0 & 0 & -\frac{1}{\rho_0} & 0 \\ 0 & -\frac{g}{\rho_0}S_0^{21} & \frac{g}{\rho_0}(p_0 - S_0^{22}) & 0 & 0 & 0 & 0 \\ 0 & 0 & \mu & 0 & 0 & 0 & 0 \\ 0 & 0 & -\mu & 0 & 0 & 0 & 0 \\ 0 & -\mu & 0 & 0 & 0 & 0 & 0 \end{pmatrix}. \quad (5.29)$$

The eigenvalues of the characteristic functional  $\Sigma_S(\mathbf{n}) = n_1 A_S^{(1)} + n_2 A_S^{(2)}$  are real for all  $\|\mathbf{n}\|_2 = 1$ . We have

$$\begin{aligned}\lambda_{1,2,3} &= 0 \\ \lambda_{4,5} &= \sqrt{\frac{\mu}{\rho_0}} \\ \lambda_{6,7} &= -\sqrt{\frac{\mu}{\rho_0}},\end{aligned}$$

where  $\mu$  is the shear modulus and  $\sqrt{\mu/\rho_0}$  is the propagation speed of transversal waves in solid bodies as given in any textbook on mechanics, e.g. [44].

### 5.2.1 Characteristic System

The aim of this section is to transfer the approach carried out for the Euler part to the shear part. Therefore, let  $L_S$  be the matrix of left eigenvectors of the characteristic functional  $\Sigma_S(\mathbf{n})$ . Then  $L_S$  is given by

$$L_S = \begin{pmatrix} 1 & 0 & 0 & 0 & 0 & 0 & 0 \\ 0 & 0 & 0 & 0 & 1 & 1 & 0 \\ 0 & 0 & 0 & \mu\rho_0 & \alpha_1 & 0 & \alpha_2 \\ 0 & -\sqrt{\mu\rho_0} & 0 & 0 & n_1 & 0 & n_2 \\ 0 & 0 & -\sqrt{\mu\rho_0} & 0 & 0 & n_2 & n_1 \\ 0 & \sqrt{\mu\rho_0} & 0 & 0 & n_1 & 0 & n_2 \\ 0 & 0 & \sqrt{\mu\rho_0} & 0 & 0 & n_2 & n_1 \end{pmatrix},$$

where  $\alpha_1$  and  $\alpha_2$  are defined as

$$\begin{aligned}\alpha_1 &:= -n_1^2 g \sigma_0^{11} + n_2^2 g \sigma_0^{22} \\ \alpha_2 &:= -g S_0^{21} - g n_1 n_2 (\sigma_0^{11} + \sigma_0^{22}).\end{aligned}$$

$L_S$  is a regular matrix with  $\det(L_S) = 4\mu\rho_0$ . Hence, the system is hyperbolic.

We find the characteristic variables  $w_S^{(i)}$  for the shear part by relation (2.11) such that

$$\begin{aligned}w_S^{(1)} &= \rho \\ w_S^{(2)} &= S^{11} + S^{22} \\ w_S^{(3)} &= \mu\rho_0 p + g [-n_1^2 \sigma_0^{11} + n_2^2 \sigma_0^{22}] S^{11} + g [2n_1 n_2 p_0 - S_0^{21}] S^{21} \\ w_S^{(4)} &= -\sqrt{\mu\rho_0} v_1 + n_1 S^{11} + n_2 S^{21} \\ w_S^{(5)} &= -\sqrt{\mu\rho_0} v_2 + n_2 S^{22} + n_1 S^{21} \\ w_S^{(6)} &= \sqrt{\mu\rho_0} v_1 + n_1 S^{11} + n_2 S^{21} \\ w_S^{(7)} &= \sqrt{\mu\rho_0} v_2 + n_2 S^{22} + n_1 S^{21}.\end{aligned}$$



The characteristic system is then given by

$$\frac{Dw_S^{(1)}}{Dt} = 0 \quad (5.30)$$

$$\frac{Dw_S^{(2)}}{Dt} = 0 \quad (5.31)$$

$$\frac{Dw_S^{(3)}}{Dt} + 2g\mu p_0 \mathbf{s} \cdot (\mathbf{s} \cdot \nabla) \mathbf{v} = 0 \quad (5.32)$$

$$\frac{Dw_S^{(4)}}{Dt} + \sqrt{\frac{\mu}{\rho_0}} \mathbf{n} \cdot \nabla w_S^{(4)} + \sqrt{\frac{\mu}{\rho_0}} \mathbf{s} \cdot \nabla w_S^{(7)} = 0 \quad (5.33)$$

$$\frac{Dw_S^{(5)}}{Dt} + \sqrt{\frac{\mu}{\rho_0}} \mathbf{n} \cdot \nabla w_S^{(5)} - \sqrt{\frac{\mu}{\rho_0}} \mathbf{s} \cdot \nabla w_S^{(6)} = 0 \quad (5.34)$$

$$\frac{Dw_S^{(6)}}{Dt} - \sqrt{\frac{\mu}{\rho_0}} \mathbf{n} \cdot \nabla w_S^{(6)} - \sqrt{\frac{\mu}{\rho_0}} \mathbf{s} \cdot \nabla w_S^{(5)} = 0 \quad (5.35)$$

$$\frac{Dw_S^{(7)}}{Dt} - \sqrt{\frac{\mu}{\rho_0}} \mathbf{n} \cdot \nabla w_S^{(7)} + \sqrt{\frac{\mu}{\rho_0}} \mathbf{s} \cdot \nabla w_S^{(4)} = 0. \quad (5.36)$$

Let us make some remarks on this system and look for system-inherent directions as in the Euler part.

- The density  $w_S^{(1)}$  and the trace of the deviatoric stress  $w_S^{(2)}$  do not change in this system.
- If  $g$  is equal to zero, i.e. if the pressure does not depend on the internal energy  $e$ , then the pressure also remains constant.
- In equation (5.32) the same quadratic form occurs as in the Euler part in (5.13). Hence, the direction which minimizes the absolute value of this form is system-inherent.
- Each of the equations (5.33) - (5.36) has a source term of the form  $\pm \sqrt{\mu/\rho_0} \mathbf{s} \cdot \nabla w^{(\cdot)}$ . Every direction which sets one of these source terms to zero is system-inherent.

Obviously it is not possible to choose a direction  $\mathbf{n}$  such that all source terms vanish simultaneously. Even when restricting on the source terms of the last four equations this is not possible although they have a very similar structure.

### 5.2.2 Technical Problems

Neglecting the direction which minimizes the quadratic form, we still need to consider four different ones among that all directions are of equal importance. *We conclude that it is not reasonable to state the finite pointset approximation for a single upwind direction.*

That means that this approach considers more upwind directions than a canonical dimensional splitting with one-dimensional upwinding for each subsystem. From this point of view it is doubtful whether it is reasonable to put much effort into establishing a finite pointset approximation similar to the one stated for the Euler equation.

Problems occur when trying to extend the previous concepts to the third space dimension. Remember that all computations in this thesis are performed fully three-dimensionally. Hence, we need to write the characteristic system in a form which allows the identification of the system-inherent directions. It turns out that this is a fundamental problem for the shear part.

The reason for this lies in equation (4.14) for the evolution of the deviatoric stress. Remember that

$$\frac{DS}{Dt} = 2\mu \left( \dot{\varepsilon} - \frac{1}{d} \text{trace}(\dot{\varepsilon}) \right),$$

where  $d$  is the space dimension. Consider for a moment the equations for  $DS^{11}/Dt$  in two and three space dimensions, that is

$$(2d) \quad \frac{DS^{11}}{Dt} = \mu \left( \frac{\partial v_1}{\partial x_1} - \frac{\partial v_2}{\partial x_2} \right),$$

$$(3d) \quad \frac{DS^{11}}{Dt} = \mu \left( \frac{4}{3} \frac{\partial v_1}{\partial x_1} - \frac{2}{3} \frac{\partial v_2}{\partial x_2} - \frac{2}{3} \frac{\partial v_3}{\partial x_3} \right),$$

respectively. The coefficients  $-2/3$  and  $4/3$  in three dimensions in contrast to  $\pm 1$  in the two-dimensional case lead to a tremendous increase of the number of non-zero elements in the eigenvectors of  $\Sigma_S(\mathbf{n})$  and thus in  $L_S$ .

For that reason we are not able to achieve the major objectives of the transformation into the characteristic system.

- For the shear part the different equations are much more coupled in the characteristic form than in the original one.
- The characteristic system is in such a complex form that it is not possible to identify system-inherent directions.

In particular, the second point is crucial for the further proceeding. Much effort has been put into investigating the characteristic system. Anyhow, we are still not able to extract information on the directions in which we should perform upwinding.

### 5.2.3 Dimensional Upwinding

Due to the problems arising from the application of the approach of Deconinck, we present an alternative way to treat the shear part. We start from the quasi-linear form

$$\frac{D}{Dt} \Phi_S + A_S^{(1)} \frac{\partial}{\partial x_1} \Phi_S + A_S^{(1)} \frac{\partial}{\partial x_2} \Phi_S = 0, \quad (5.37)$$

where the system matrices  $A_S^{(1)}$  and  $A_S^{(2)}$  are defined by (5.28) and (5.29), respectively. Instead of searching for system-inherent directions we propose to do upwinding in fixed directions. These directions are canonically the axes of the Cartesian coordinate system.

The following approach is *no* dimensional splitting in the usual sense as described for example in [28, 48]. A dimensional splitting for the shear part in two space dimensions would read

$$\begin{aligned} \frac{D}{Dt} \Phi^{(1)} + A_S^{(1)} \frac{\partial}{\partial x_1} \Phi_S^{(1)} &= 0 \\ \frac{D}{Dt} \Phi^{(2)} + A_S^{(2)} \frac{\partial}{\partial x_2} \Phi_S^{(2)} &= 0 \end{aligned}$$

with appropriate initial and boundary conditions for the subsystems. But there are well-known problems for shocks running in direction of the bisecting lines of the coordinate axes. Instead of the dimensional splitting we thus introduce the *dimensional upwinding*.

**Definition 5.2 (Dimensional Upwinding)** Let  $\mathbf{n}^{(i)}$  be the  $i$ -th unit vector and  $\Pi_{uw}^{\mathbf{n}^{(i)}} \mathcal{L}$  the finite pointset approximation of a system of PDEs with upwinding in direction  $\mathbf{n}^{(i)}$  according to (5.24). Then the dimensional upwinding is given by

$$\frac{D}{Dt} \Phi = \Pi_{uw}^D \mathcal{L}(\Phi) := \frac{1}{d} \sum_{i=1}^d \Pi_{uw}^{\mathbf{n}^{(i)}} \mathcal{L}(\Phi), \quad (5.38)$$

where  $d$  is the space dimension.

In the dimensional upwinding we state the finite pointset approximation for each  $\mathbf{n}^{(i)}$  and take the mean value of the results to obtain the update of the different quantities.

Let us apply this approach to the shear part in two dimensions and consider first the system for  $\mathbf{n}^{(1)}$ , where

$$\mathbf{n}^{(1)} = \begin{pmatrix} 1 \\ 0 \end{pmatrix}.$$

The characteristic functional  $\Sigma_S(\mathbf{n}^{(1)})$  is simply  $A_S^{(1)}$  and the left eigenvectors are thereby the eigenvectors of  $A_S^{(1)}$ . We have

$$L_S^{(1)} := L_S(\mathbf{n}^{(1)}) = \begin{pmatrix} 1 & 0 & 0 & 0 & 0 & 0 & 0 \\ 0 & 0 & 0 & 0 & 1 & 1 & 0 \\ 0 & 0 & 0 & \mu\rho_0 & -g\sigma_0^{11} & 0 & -gS^{21} \\ 0 & -\sqrt{\mu\rho_0} & 0 & 0 & 1 & 0 & 0 \\ 0 & 0 & -\sqrt{\mu\rho_0} & 0 & 0 & 0 & 1 \\ 0 & \sqrt{\mu\rho_0} & 0 & 0 & 1 & 0 & 0 \\ 0 & 0 & \sqrt{\mu\rho_0} & 0 & 0 & 0 & 1 \end{pmatrix}.$$

Hence, with characteristic variables  $\mathbf{w}_{S_1} := L_S^{(1)}\Phi_S$  the characteristic system for  $\mathbf{n}^{(1)}$  is given by

$$\frac{Dw_{S_1}^{(1)}}{Dt} = 0 \quad (5.39)$$

$$\frac{Dw_{S_1}^{(2)}}{Dt} = 0 \quad (5.40)$$

$$\frac{Dw_{S_1}^{(3)}}{Dt} + 2g\mu\rho_0 \frac{\partial v_2}{\partial x_2} = 0 \quad (5.41)$$

$$\frac{Dw_{S_1}^{(4)}}{Dt} + \sqrt{\frac{\mu}{\rho_0}} \frac{\partial w_{S_1}^{(4)}}{\partial x_1} + \sqrt{\frac{\mu}{\rho_0}} \frac{\partial w_{S_1}^{(7)}}{\partial x_2} = 0 \quad (5.42)$$

$$\frac{Dw_{S_1}^{(5)}}{Dt} + \sqrt{\frac{\mu}{\rho_0}} \frac{\partial w_{S_1}^{(5)}}{\partial x_1} - \sqrt{\frac{\mu}{\rho_0}} \frac{\partial w_{S_1}^{(6)}}{\partial x_2} = 0 \quad (5.43)$$

$$\frac{Dw_{S_1}^{(6)}}{Dt} - \sqrt{\frac{\mu}{\rho_0}} \frac{\partial w_{S_1}^{(6)}}{\partial x_1} - \sqrt{\frac{\mu}{\rho_0}} \frac{\partial w_{S_1}^{(5)}}{\partial x_2} = 0 \quad (5.44)$$

$$\frac{Dw_{S_1}^{(7)}}{Dt} - \sqrt{\frac{\mu}{\rho_0}} \frac{\partial w_{S_1}^{(7)}}{\partial x_1} + \sqrt{\frac{\mu}{\rho_0}} \frac{\partial w_{S_1}^{(4)}}{\partial x_2} = 0. \quad (5.45)$$

The source terms include derivatives with respect to  $x_2$  only. This is clear since  $L_S^{(1)}$  diagonalizes just  $A^{(1)}$ . Furthermore, transport happens only in the  $x_1$ -direction. Hence, we are able to apply the one-dimensional upwinding described in Section 3.2.3. In the following let

$$\begin{aligned} \Pi_i^+ \phi(\mathbf{x}) &:= \Pi \phi(\mathbf{x} - \delta \sqrt{\frac{\mu}{\rho_0}} \mathbf{n}^{(i)}), \\ \Pi_i^- \phi(\mathbf{x}) &:= \Pi \phi(\mathbf{x} + \delta \sqrt{\frac{\mu}{\rho_0}} \mathbf{n}^{(i)}) \quad \text{and} \\ \Pi_i^c &:= \frac{1}{2} (\Pi_i^+ + \Pi_i^-). \end{aligned}$$

The subscript  $i$  represents upwinding in direction of the  $i$ -th unit vector. The

finite pointset approximation for the shear part in direction  $\mathbf{n}^{(1)}$  reads then

$$\begin{aligned}
\frac{Dw_{S_1}^{(1)}}{Dt} &= 0 \\
\frac{Dw_{S_1}^{(2)}}{Dt} &= 0 \\
\frac{Dw_{S_1}^{(3)}}{Dt} + 2g\mu p_0 \Pi_1^c \frac{\partial v_2}{\partial x_2} &= 0 \\
\frac{Dw_{S_1}^{(4)}}{Dt} + \sqrt{\frac{\mu}{\rho_0}} \Pi_1^+ \frac{\partial w_{S_1}^{(4)}}{\partial x_1} + \sqrt{\frac{\mu}{\rho_0}} \Pi_1^c \frac{\partial w_{S_1}^{(7)}}{\partial x_2} &= 0 \\
\frac{Dw_{S_1}^{(5)}}{Dt} + \sqrt{\frac{\mu}{\rho_0}} \Pi_1^+ \frac{\partial w_{S_1}^{(5)}}{\partial x_1} - \sqrt{\frac{\mu}{\rho_0}} \Pi_1^c \frac{\partial w_{S_1}^{(6)}}{\partial x_2} &= 0 \\
\frac{Dw_{S_1}^{(6)}}{Dt} - \sqrt{\frac{\mu}{\rho_0}} \Pi_1^- \frac{\partial w_{S_1}^{(6)}}{\partial x_1} - \sqrt{\frac{\mu}{\rho_0}} \Pi_1^c \frac{\partial w_{S_1}^{(5)}}{\partial x_2} &= 0 \\
\frac{Dw_{S_1}^{(7)}}{Dt} - \sqrt{\frac{\mu}{\rho_0}} \Pi_1^- \frac{\partial w_{S_1}^{(7)}}{\partial x_1} + \sqrt{\frac{\mu}{\rho_0}} \Pi_1^c \frac{\partial w_{S_1}^{(4)}}{\partial x_2} &= 0.
\end{aligned}$$

Having identified the terms that need to be upwinded, the system is transformed back into its original form to obtain the appropriate approximation in direction  $\mathbf{n}^{(1)}$  for the primitive variables. Analogously, the upwinding is performed for the second direction  $\mathbf{n}^{(2)}$ .

The dimensional upwinding for the shear part in two dimensions is then given by

$$\frac{D\rho}{Dt} = 0 \quad (5.46)$$

$$\frac{Dv_i}{Dt} = \frac{1}{\rho_0} \frac{\partial S_{D_{uw}}^{ij}}{\partial x_j} \quad (5.47)$$

$$\frac{Dp}{Dt} = \sigma_0^{ij} \frac{g}{\rho_0} \frac{\partial v_{D_{uw}}^{(i)}}{\partial x_j} \quad (5.48)$$

$$\frac{DS^{ij}}{Dt} = \mu \left( \frac{\partial v_{D_{uw}}^{(i)}}{\partial x_j} + \frac{\partial v_{D_{uw}}^{(j)}}{\partial x_i} - \delta_{ij} \operatorname{div}(\mathbf{v}_{D_{uw}}) \right), \quad (5.49)$$

where  $\delta_{ij}$  is the Kronecker symbol and

$$\frac{\partial v_{D_{uw}}^{(i)}}{\partial x_j} := \frac{1}{2} \left( \Pi_1^c v_{x_j}^{(i)} + \Pi_2^c v_{x_j}^{(i)} \right) - \frac{1}{2\sqrt{\mu\rho_0}} \frac{\Pi_j^+ S_{x_j}^{ij} - \Pi_j^- S_{x_j}^{ij}}{2} \quad (5.50)$$

$$\frac{\partial S_{D_{uw}}^{ij}}{\partial x_j} := \frac{1}{2} \left( \Pi_1^c S_{x_j}^{ij} + \Pi_2^c S_{x_j}^{ij} \right) - \frac{\sqrt{\mu\rho_0}}{2} \frac{\Pi_j^+ v_{x_j}^{(i)} - \Pi_j^- v_{x_j}^{(i)}}{2}. \quad (5.51)$$

We observe the same structure as for the upwind velocity and the upwind pressure defined in (5.22) and (5.23), respectively. The central particle approximations are corrected by some terms due to the upwinding. In analogy to the

Euler part, we define the *dimensional velocity* and the *dimensional stress* by

$$v_{D_{uw}}^{(i)} := \frac{1}{2} \sum_{l=1}^2 \left( \frac{\Pi_l^+ v_i + \Pi_l^- v_i}{2} \right), \quad (5.52)$$

$$S_{D_{uw}}^{ij} := \frac{1}{2} \sum_{l=1}^2 \left( \frac{\Pi_l^+ S^{ij} + \Pi_l^- S^{ij}}{2} \right), \quad (5.53)$$

respectively.

**Remark 5.7** *The basic proceeding is just the same as in the Euler part. The difference is that in the shear case we use fixed directions and average over the results. In the Euler case, the upwinded approximations are formulated for arbitrary directions.*

### 5.2.4 Boundary Conditions

In analogy to Section 5.1.2, we use the characteristic system of the shear part to determine the number of boundary conditions needed. With the same argument we see from equations (5.33) to (5.36) that we have to prescribe two conditions for the two-dimensional case. In three dimensions, we have to provide three conditions.

For the shear part, we consider always problems having a free surface. Therefore, we prescribe the normal stress at the boundary, namely

$$\sigma \mathbf{n} = -p_o \mathbf{n},$$

where  $p_o$  is the outer pressure. This gives the desired number of boundary conditions for the respective dimensions.

## 5.3 Rotation Part - Jaumann Rate

We consider the subsystem describing the rotation of the deviatoric stress tensor  $S$  given by equations (4.15) – (4.18).

### 5.3.1 Reduced System for Rotation Part

The system matrices  $A_R^{(i)}$  of that part are given by

$$A_R^{(i)} = \begin{pmatrix} 0 & \cdots & 0 \\ \vdots & \ddots & \vdots \\ 0 & \cdots & 0 & \cdots & 0 \\ \tilde{A}_R^{(i)} & \vdots & \vdots \\ & 0 & \cdots & 0 \end{pmatrix},$$

where

$$\tilde{A}_R^{(1)} := \begin{pmatrix} 0 & 0 & S^{21} \\ 0 & 0 & -S^{21} \\ 0 & 0 & -S^{11} \end{pmatrix} \quad \text{and} \quad \tilde{A}_R^{(2)} := \begin{pmatrix} 0 & -S^{21} & 0 \\ 0 & S^{21} & 0 \\ 0 & S^{11} & 0 \end{pmatrix}.$$

The characteristic functional  $\Sigma_R(\mathbf{n})$  is singular and thus not diagonalizable. Since all eigenvalues are equal to zero, the system is weakly hyperbolic. Therefore, the characteristic approach described previously fails for the rotation part.

Except for the deviatoric stress, all quantities remain constant in this system. For this reason we consider a reduced system describing only the evolution of the stress. The velocity acts as source term and is assumed to be constant in each time step. The equations under consideration are simply the Jaumann rate

$$\frac{dS}{dt} = RS - SR, \quad (5.54)$$

where  $R$  is the skew-symmetric local rotation rate tensor defined by (1.22).

Assuming constant velocity in each time step, we are able to solve (5.54) analytically for these time steps. This will be the result of Lemma 5.3. But first we give some basic properties of pure rotations.

### 5.3.2 Basic Results for Rotations

Let the time-dependent matrix  $M(t) \in SO(d)$  for all time  $t$  and  $M(t_0)$  be the identity matrix, where  $SO(d)$  denotes the special orthogonal group over  $\mathbb{R}^{d \times d}$ , with properties  $MM^T = M^T M = I$  and  $\det(M) = 1$  for all  $M \in SO(d)$ . Furthermore, let  $M(t)$  be differentiable for all  $t$ . The pure rotation of any vector  $\mathbf{k}_0$  is given by

$$\mathbf{k}(t) = M(t)\mathbf{k}_0, \quad (5.55)$$

such that

$$\dot{\mathbf{k}}(t) = \dot{M}(t)\mathbf{k}_0 \quad (5.56)$$

since  $\mathbf{k}_0$  is constant in time, where the dot denotes total derivative with respect to time. Sometimes, we equivalently use  $d/dt$ .

**Lemma 5.1** *Let  $M(t) \in SO(d)$  be differentiable for all  $t$  with  $M(t_0) = I$ . Then there exists a skew-symmetric matrix  $R$  such that*

$$\dot{M} = RM. \quad (5.57)$$

*Proof:*

$$\begin{aligned} 0 &= \frac{d}{dt}I = \frac{d}{dt}(MM^T) = \dot{M}M^T + M\dot{M}^T \\ \Rightarrow \dot{M} &= -M\dot{M}^T M =: RM \end{aligned}$$

It remains to show that  $R^T = -R$  but

$$R^T = (-MM^T)^T = -\dot{M}M^T = MM^T = -R$$

□

In Section 1.2.3 we stated that in a pure rotation a vector  $\mathbf{k}$  obeys the ordinary differential equation  $\dot{\mathbf{k}} = R\mathbf{k}$ . This is true since Lemma 5.1 together with (5.56) gives

$$\dot{\mathbf{k}}(t) = \dot{M}(t)\mathbf{k}_0 = RM(t)\mathbf{k}_0 = R\mathbf{k}(t).$$

Conversely, for a given skew-symmetric matrix  $R$ , Lemma 5.1 allows us to define a rotation matrix  $M(t) \in SO(d)$ .

**Lemma 5.2** *Let  $R \in \mathbb{R}^{d \times d}$  be a skew-symmetric matrix and  $M_0 \in SO(d)$ . Furthermore, let  $R$  be constant. Then*

1.

$$M(t) := e^{tR}M_0 \in SO(d)$$

2.  $M(t)$  obeys the differential equation

$$\frac{d}{dt}M(t) = RM(t)$$

*Proof*

1. In order to show that  $M(t) \in SO(d)$  we first show that  $MM^T = I$ , since then  $\det(M) = \pm 1$ . We have

$$\begin{aligned} MM^T &= (e^{tR}M_0)(e^{tR}M_0)^T = e^{tR}M_0M_0^T(e^{tR})^T \\ &\stackrel{M_0 \in SO(d)}{=} e^{tR}e^{tR^T} \\ &= e^{tR}e^{-tR} = I. \end{aligned}$$

Furthermore, since  $M(t)$  is continuous in  $t$  and  $M(t=0) = M_0 \in SO(d)$ , it follows that  $\det(M(t)) = 1$  and thus  $M(t) \in SO(d)$  for all  $t$ .

2. The statement is clear since  $R$  and  $M_0$  are constant.

□



### 5.3.3 Rotation of the Stress Tensor

But now let us come back to the equation for the stress tensor (5.54). The following lemma will provide the basis for the treatment of the Jaumann rate.

**Lemma 5.3** *Let  $R \in \mathbb{R}^{d \times d}$  be a skew-symmetric matrix and define  $M(t)$  as given in Lemma 5.2. Then*

$$S(t) = M(t)S_0M^T(t) \quad (5.58)$$

solves (5.54).

*Proof:*

$$\begin{aligned} \dot{S} &= \dot{M}S_0M^T + MS_0\dot{M}^T \\ &= RMS_0M^T + MS_0(RM)^T \\ &= RMS_0M^T + MS_0M^TR^T \\ &\stackrel{R^T = -R}{=} RS - SR \end{aligned}$$

□

This means that the tensor  $S$  at time  $t$  is simply the initial tensor  $S_0$  given in a rotated coordinate system. We will use (5.58) to compute the stress tensor analytically in the rotation part. The rotation rate tensor is defined locally. Hence, equation (5.58) describes the local rotation of the stress tensor  $S$ . The actual form of  $M(t)$  in two dimensions is given by

$$M(t) = \begin{pmatrix} \cos(r_{21}t) & -\sin(r_{21}t) \\ \sin(r_{21}t) & \cos(r_{21}t) \end{pmatrix},$$

where  $r_{ij}$  is the  $ij$ -th entry of the rotation rate matrix  $R$ . In three dimensions we can write

$$M(t) = I + \frac{1}{\omega}R \sin(\omega t) - \frac{1}{\omega^2}(1 - \cos(\omega t))RR^T, \quad (5.59)$$

where  $\omega^2 = r_{21}^2 + r_{31}^2 + r_{32}^2$ . One can easily show that  $M(0) = I$  and  $\dot{M} = RM$ .

## 5.4 Coupling of Systems

In Section 4.2 we discussed that in case of operator splitting the particles must not be moved in each subsystem. Therefore, we have to specify the system in which the update of the position is performed. The coupling of the respective schemes is done as follows.

1. The shear part is solved using the dimensional upwinding as specified by equation (5.38). The particles are moved with the dimensional velocity (5.52).
2. On the basis of the intermediate results of the shear part, the Euler part is solved using the upwinded particle approximation (5.24) in direction of the pressure gradient. The particles are moved with the correction term of the upwind velocity (5.22).
3. On the basis of the intermediate results of the Euler part, the rotation part is solved analytically by equation (5.58). The particles are not moved.

The boundary conditions of the different subsystems corresponds to those already specified in the respective sections.

## Chapter 6

# Results for the Subsystems

In this chapter we present results of the respective numerical schemes developed in the previous chapter. The particles are moved with the velocity field in each subsystem and are thereby considered in a Lagrangian framework.

We compare the results of the computations performed using the central particle approximation operator (3.12) with those obtained using the respective schemes for each subsystem. In the rotation part the stress, the velocity and the position of the particles are analytically integrated according to (5.58) and (5.55), respectively.

The Finite Pointset Method has successfully been applied to a wide range of industrial problems at the Fraunhofer ITWM in Kaiserslautern. The code was mainly developed by Dr. Kuhnert and Dr. Tiwari.

In the present work, we have implemented additional routines to simulate elastic solids. The particle organization is based on the code provided by Kuhnert and is described in [24]. Therefore, we do not go into organizational details.

**Remark 6.1** *Due to the complexity of the considered system and the resulting lack of some theoretical aspects of the mixed formulation of the systems, we validate the respective schemes by qualitatively comparing the results with the physically expected behavior. In this sense, stability is not to be understood in a mathematically strict sense but in the ability to reproduce the physical processes correctly.*

We are mainly interested in the pressure and the stress distribution within the solid. Therefore in each picture, the color map is adjusted in such a way that these structures are visualized at the best.

**Convention** *If nothing else is specified the pictures have the  $x_3$ -axis as view direction, that means that the reader looks onto the  $x_1$ - $x_2$ -plane.*

## 6.1 Results for the Euler Part

The results presented in this section are computed using one single upwind direction according to the discussions given in Section 5.1.3.

For testing the Euler part, we apply the equation of state for ideal gas

$$p(\rho, e) = \frac{R_g}{c_v} \rho e,$$

where  $R_g$  is the gas constant and  $c_v$  the specific heat.

The particles are moved according to their upwind velocity (5.22) instead of their physical velocity  $\mathbf{v}$ .

### 6.1.1 Three-Dimensional Shock Tube Problem

As a first test of the method derived for Euler equations we consider a three-dimensional shock tube problem. We compare the results of the upwinded scheme with those of the central scheme using the particle approximation operator (3.12).

#### Geometry of the Computational Domain

The computational domain  $\Omega$  is a cuboid with edge lengths  $a = 20$ ,  $b = 4$  and  $c = 4$  as sketched in Figure 6.1 such that

$$\Omega = \{\mathbf{x} \in \mathbb{R}^3 : x_1 \in (-10, 10), x_2 \in (-2, 2), x_3 \in (-2, 2)\}$$

with boundary  $\partial\Omega$ .

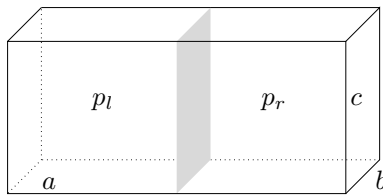


Figure 6.1: Geometry

#### Computational Settings

We give the basic computational settings of the calculations. These are the *smoothing length*  $h$ , i.e. the interaction radius of the particles, the *initial particle distribution*  $r$ , i.e. the initial average relative distance of the particles with respect to  $h$ , and the *time step*  $\Delta t$ .

- Smoothing length:  $h = 1.5$
- Initial particle distribution:  $r = 0.5$
- Time step:  $\Delta t = 0.001$

### Boundary Conditions

The boundary  $\partial\Omega$  is the surface of the cuboid and is assumed to be a solid wall. From that we derive the boundary condition for the problem

$$\mathbf{v}(\mathbf{x}, t) \cdot \mathbf{n}(\mathbf{x}) = 0 \quad \forall \mathbf{x} \in \partial\Omega,$$

where  $\mathbf{n}(\mathbf{x})$  is the inward normal to the boundary in point  $\mathbf{x} \in \partial\Omega$ . Furthermore, we assume slip condition, that means that the tangential component of the velocity is not influenced at the boundary.

### Initial Conditions

In order to complete the description of the considered problem we need to give the initial conditions for the quantities. For the density and the velocity we have

$$\begin{aligned} \rho_0(\mathbf{x}) &:= \rho(\mathbf{x}, 0) = 1 \\ \mathbf{v}_0(\mathbf{x}) &:= \mathbf{v}(\mathbf{x}, 0) = 0 \end{aligned}$$

for all  $\mathbf{x} \in \Omega$ , respectively. Furthermore, we assume that the initial pressure has a jump, i.e.

$$p_0(\mathbf{x}) := p(\mathbf{x}, 0) = \begin{cases} p_l = 10 & x_1 < 0 \\ p_r = 1 & x_1 \geq 0, \end{cases}$$

as sketched in Figure 6.1.

### Results Using Central Differences

In order to motivate upwinding techniques, we first present results using the central least squares operator (3.11). We expect instabilities because of the jump in the initial pressure.

Figure 6.2 shows a sequence of pictures visualizing the pressure for different times. The first one shows the initial pressure. The following pictures are taken every 500 time steps. Note that the color bar changes with each picture.

We see already in the second picture that the scheme is not stable. The highest pressure can be found on the right of the shock. This instability amplifies such that at time  $t = 1.0$  s the pressure of single particles increases up to more than 20 or decreases down to well below -5. These extreme pressures occur in the direct neighborhood of the initial discontinuity.

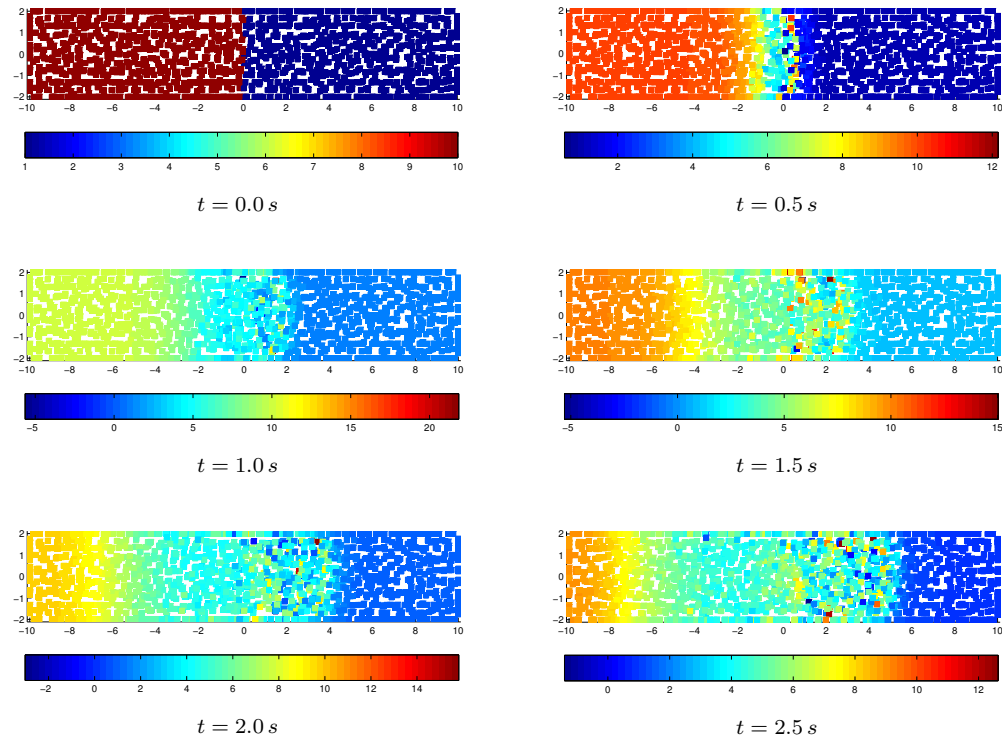


Figure 6.2: Pressure without upwinding

Furthermore, it seems that in the pictures for time  $t = 0.5 s$  and  $t = 1.5 s$  to  $t = 2.5 s$  the pressure exhibits some vertical pattern. This pattern reminds of waves running to the right. These oscillations are a further indication of the instability of the scheme. The computation breaks after approximately 3.5 s.

*We conclude that upwinding in direction of the velocity field inherent to the Finite Pointset Method does not suffice to stabilize Euler equations.*

### Upwinding in Minimization Direction

We have seen that Euler equations have two system-inherent directions. We present now the results for upwinding in the direction which minimizes (5.27).

The sequence of pictures in Figure 6.3 shows again the pressure for different times. At time  $t = 0.5 s$  it seems that this method handles the shock better than the naive approach.

However, at time  $t = 1.0 s$  we notice single particles with high pressure oscillations. This continues such that we conclude that this form of upwinding does not stabilize the method. In the present example the computation breaks after 2.2 seconds.

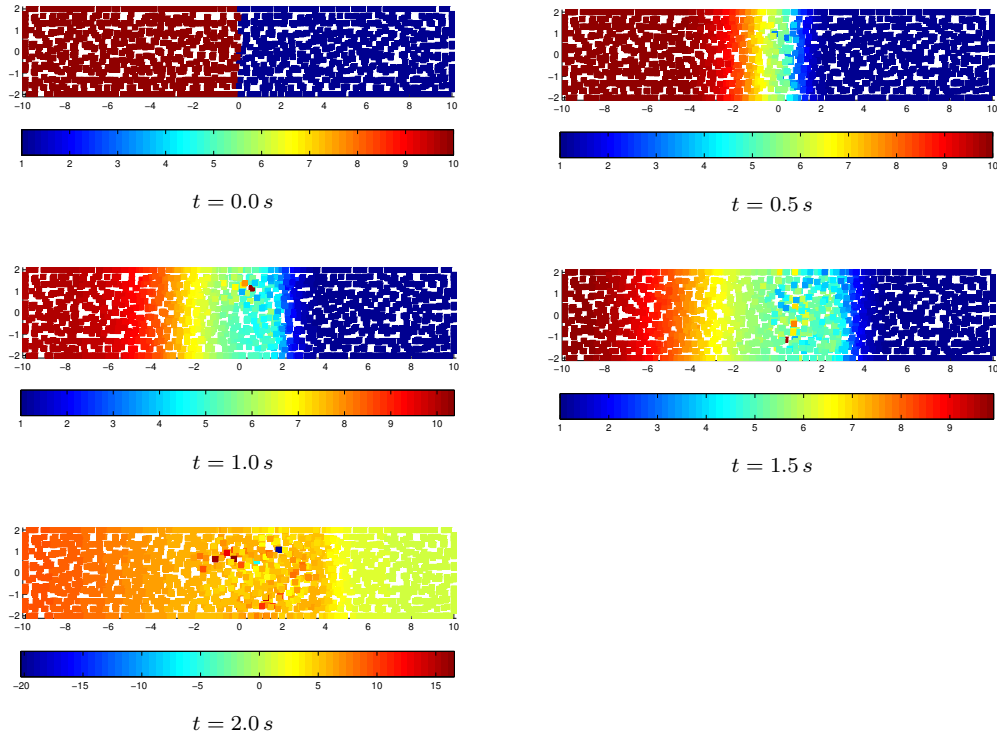


Figure 6.3: Pressure with upwinding in minimization direction

### Upwinding in Pressure Gradient Direction

The final computation for the shock-tube problem is done with upwinding in direction of the pressure gradient which is the second system-inherent direction.

Figure 6.4 shows the pressure distribution for different times. In order to compare the results with the other computations, the first four pictures display the situation at time  $t = 0.0\text{ s}$  to  $t = 1.5\text{ s}$ .

First, we note that no visible instabilities occur. There are fronts running in both directions of the discontinuity which is consistent with equations (5.14) and (5.15). In particular, we see that the two fronts propagate with the same relative speed.

The last four pictures show the situation for later times. We have chosen the points in time in such a way that the shock front reaches either the walls or approximately travels through its original location. We make the following observations.

- The maximum pressure at time  $t = 5.0\text{ s}$  is notably higher than the initial one. This is due to the fact that the particles are accelerated to the right and then reflected by the solid wall.

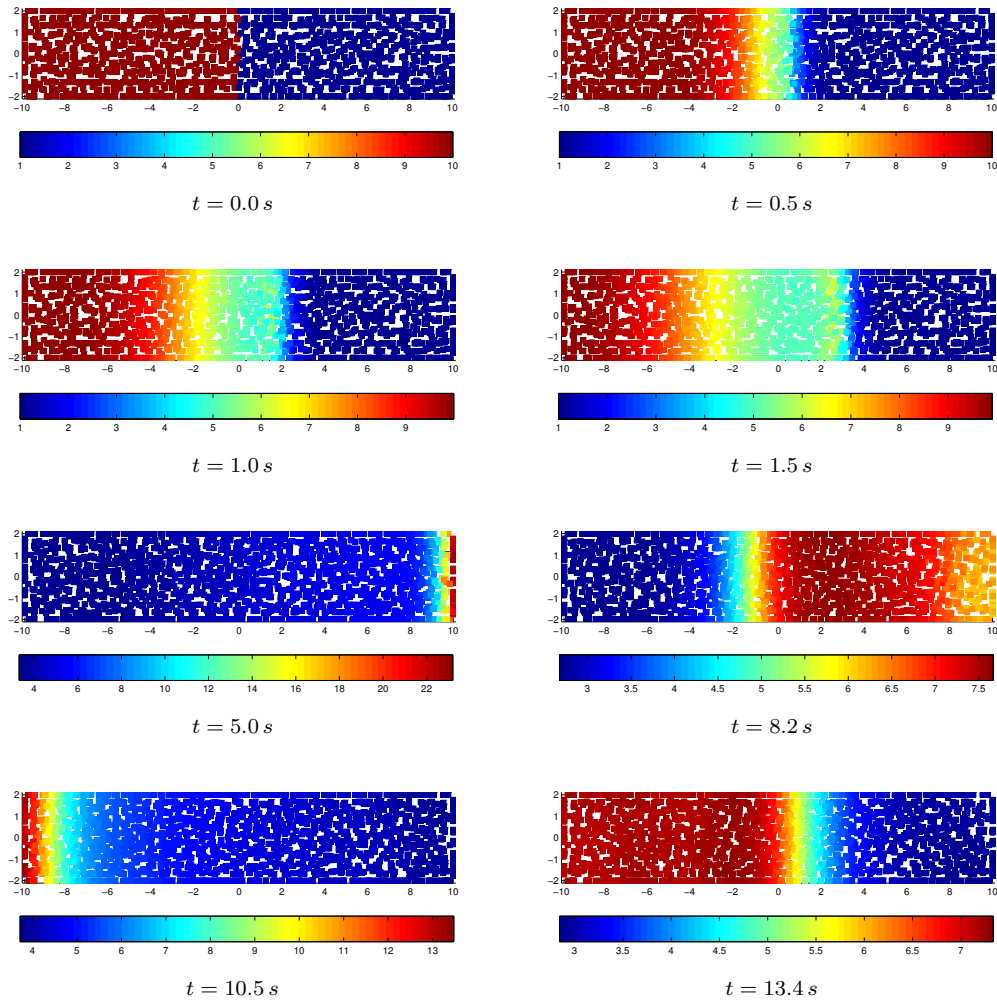


Figure 6.4: Pressure with upwinding in direction of pressure gradient

- The same behavior can be observed at time  $t = 10.5$  s. Anyhow, the pressure is not as high as in the previous case which is a consequence of the numerical dissipation.
- The shock front needs a certain time to travel through the domain. This time increases throughout the computation. That means that the speed of propagation decreases. The reason for this is a reduction of the shock speed according to the Rankine-Hugoniot-condition due to the dissipation.
- During the computation, the shock front stays comparatively sharp such that the shock can easily be located. That means in spite of the numerical viscosity the smearing out is restricted to a narrow band in space.

Most numerical schemes introduce a certain viscosity. In FPM the adjustment of the upwind offset  $\delta$  included in equations (3.16) and (3.17) provides a tool to reduce this viscosity. It turns out that  $\delta = 0.3$  is an advisable choice.



*Upwinding in direction of the pressure gradient yields satisfying results for the shock tube problem provided the particles are moved with their upwind velocity. This coincides with the results given in [24].*

### 6.1.2 Pulsation of a Sphere

As a further example we test our code with a free-boundary problem. We consider a sphere filled with ideal gas and prescribe a radial initial velocity.

**Remark 6.2** *The geometry and the computational settings of this section will be used for all following computations.*

#### Geometry of the Computational Domain

We consider a sphere with radius  $r_S = 5$  as shown in Figure 6.5, we have

$$\Omega := \{\mathbf{x} \in \mathbb{R}^3 : \|\mathbf{x}\| < 5\}.$$

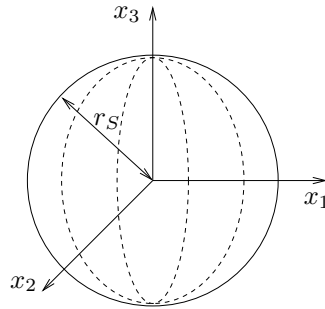


Figure 6.5: Geometry

#### Computational Settings

- Smoothing length:  $h = 1.5$
- Initial particle distribution:  $r = 0.5$
- Initial particle distribution on the boundary:  $r_b = 0.3$
- Time step:  $\Delta t = 0.001$

For the free-boundary problems we place more particles on the boundary to get better approximation results. This is not necessary for the shock problem with solid walls.

Altogether, this gives approximately an initial number of 4500 particles. Depending on the expansion or contraction of the sphere this number may change in time.

### Boundary Conditions

As stated in Section 5.1.2 we need to prescribe one boundary condition for the Euler part. In the free-boundary problem we specify the pressure, i.e.

$$p(\mathbf{x}, t) = p_o \quad \forall \mathbf{x} \in \partial\Omega,$$

where  $p_o$  is the outer pressure.

### Initial Conditions

The body under consideration has initially constant pressure and density. The particles are equipped with a diverging velocity. We have

$$\begin{aligned} \rho_0(\mathbf{x}) &:= \rho(\mathbf{x}, 0) = 1, \\ p_0(\mathbf{x}) &:= p_o = 1, \\ \mathbf{v}_0(\mathbf{x}) &:= \mathbf{v}(\mathbf{x}, 0) = 0.5 \cdot \mathbf{x} \end{aligned}$$

for all  $\mathbf{x} \in \Omega$ .

### Upwinding in Pressure Gradient Direction

Figure 6.6 is a sequence of pictures presenting the pressure for different times. The first one shows the initial situation with constant pressure.

The remaining pictures are arranged in the following way: The left column corresponds to minimal circumferences, whereas the right column visualizes the maximal ones.

The initial divergence of the particles uniformly decreases the pressure inside the sphere. The boundary conditions lead to a gradient in pressure resulting in an acceleration towards the center of the sphere. This situation is shown in the right of Figure 6.6. The initial motion of the particles is decelerated and finally reversed.

Due to the resulting motion of the particles towards the origin, the volume reduces and the pressure increases inside the body. This pressure distribution is presented in the pictures for time  $t = 2.1 s$  and  $t = 4.8 s$ . The pressure gradient provokes the re-swelling of the sphere. Euler equations have no viscous term. Therefore, we theoretically expect that this oscillation goes on forever. Anyhow, in Figure 6.6 we observe the following:

- The difference between highest and lowest pressure within the solid decreases in each column.
- The maximal radius decreases while the minimal increases. That means that the amplitude of the oscillation reduces in time.

Both observations are due to the numerical viscosity. This effect becomes even more obvious when considering the course of the radius in time.

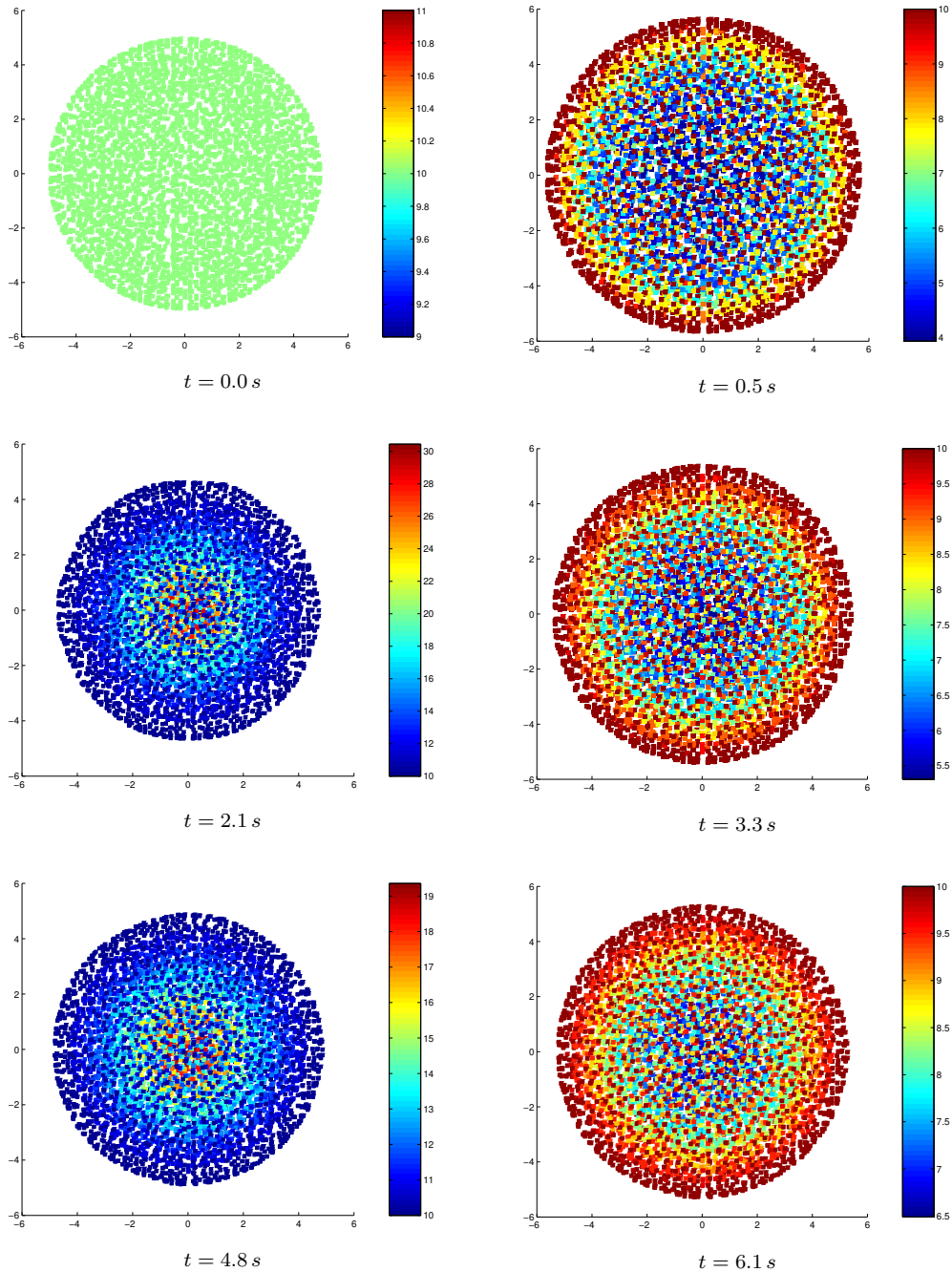


Figure 6.6: Pressure with upwinding in direction of pressure gradient

Figure 6.7 visualizes the evolution of the radius within 15 seconds. The vertical lines display the points in time of the pictures in Figure 6.6 where red and black correspond to the left and the right column, respectively.

The radius obviously fulfills a damped oscillation due to the numerical viscosity. But keep in mind that a high number of time steps (15000) has already been performed such that even a very small numerical viscosity sums up to this significant damping.

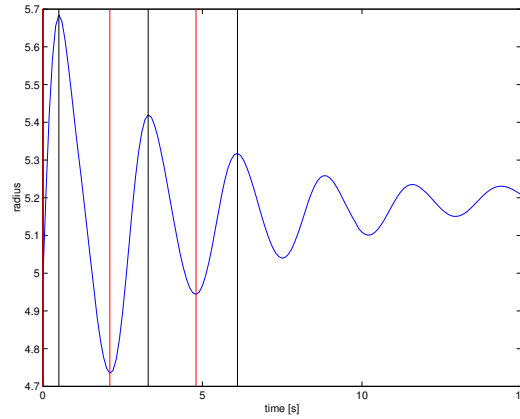


Figure 6.7: Course of radius

*Apart from the viscosity, the presented results are concordant with the expected physical behavior. Hence, we conclude that upwinding in direction of the pressure is also reliable for the free-boundary problem.*

### Results without Upwinding in Pressure Gradient Direction

The naive scheme and the upwinding in the direction minimizing (5.27) did not show good results for the shock tube problem. We expect the same for the present example. Indeed, the following two pictures confirm this supposition.

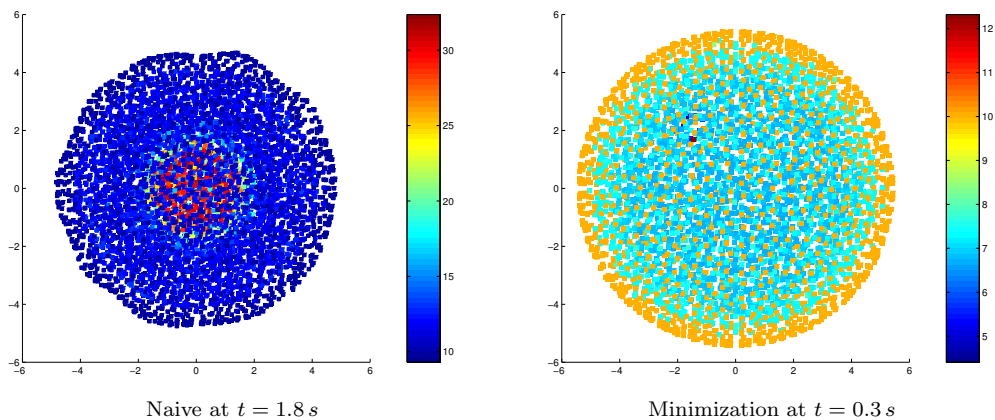


Figure 6.8: Pressure for other methods

On the left hand side of Figure 6.8 the pressure at time  $t = 1.8 s$  is displayed for the naive scheme without additional upwinding. The initial motion of the

particles is already reversed such that the high pressure inside the body is reasonable. Anyhow, the naive scheme is not able to handle the free boundary. After 1.8 seconds the computation breaks.

The right picture of the figure displays the pressure at time  $t = 0.3 s$  obtained using upwinding in the minimization direction of (5.27). Already at that early time, single particles have a pressure much higher than the surrounding ones. We conclude that this kind of upwinding is not stable.

**Convention** *Due to the results discussed above we will restrict ourselves to upwinding in direction of the pressure gradient in the following.*

### 6.1.3 Flattening of a Sphere

The last example in this context provides some additional information on the Euler part. These information will prove useful in the discussion of the results for the coupled system.

We reconsider the previous test with a slightly different initial velocity. In particular, the geometrical and computational settings remain unchanged. Furthermore, we prescribe the same boundary conditions as in Section 6.1.2.

#### Initial Conditions

For the density and the pressure, we have  $\rho_0(\mathbf{x}) = 1$  and  $p_0(\mathbf{x}) = p_o = 10$ , respectively, and the initial velocity is

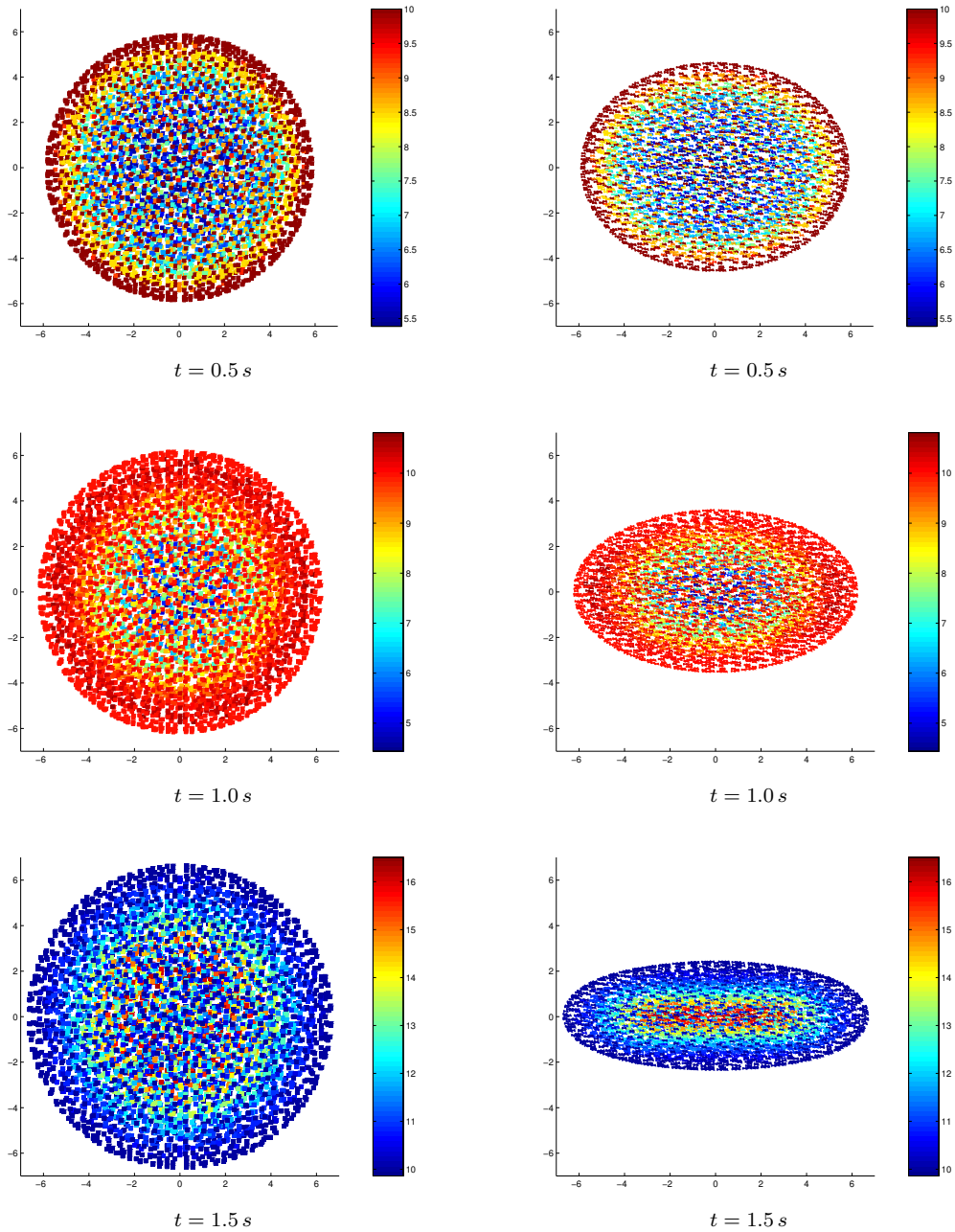
$$\mathbf{v}_0(\mathbf{x}) = 0.5 \cdot \begin{pmatrix} x_1 \\ x_2 \\ 0 \end{pmatrix}$$

for all  $\mathbf{x} \in \Omega$ . That means that the initial motion of each particle lies in a plane normal to the  $x_3$ -axis.

#### Results

Figure 6.9 displays the pressure distribution for different times. The left column displays the  $x_1$ - $x_2$ -plane and the right column shows the  $x_2$ - $x_3$ -plane. One row corresponds to one point in time.

We make the following observations: Due to the initial velocity, the radius of the sphere increases. Thereby, the pressure inside the body decreases. This situation is shown in the pictures for time  $t = 0.5 s$ . Euler equations tend to preserve the volume. Therefore, the increase of the radius is compensated by the flattening of the sphere as displayed in the right picture.

Figure 6.9: left:  $x_3$ -view, right:  $x_1$ -view

The reason for the flattening is the following: The low pressure inside the volume together with the Dirichlet boundary condition yields a pressure gradient near the surface. As a consequence the particles are accelerated in the direction opposite to the pressure gradient. In the  $x_1$ - $x_2$ -plane the initial velocity is reduced and in  $x_3$ -direction the particles start moving towards the plane. The flatter the sphere becomes the more the boundary condition gains influence in  $x_3$ -direction.

However, the situation changes with time. At time  $t = 1.5$  s the highest pressure is inside the solid. The reason for that is similar to the one for the high pressure in the shock-tube problem. The particles approach each other in the  $x_1$ - $x_2$ -plane leading to an increase in pressure. In terms of an imaginary control volume inside the solid, the flux into the control volume in  $x_3$ -direction is higher than the flux out of it in  $x_1$ - and  $x_2$ -direction.

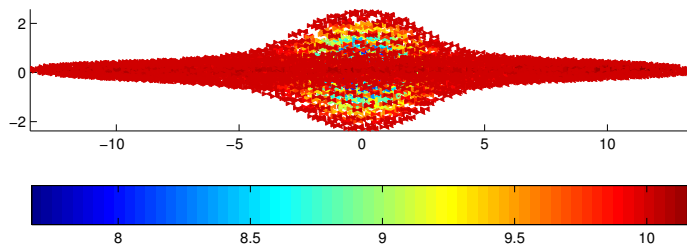


Figure 6.10: Pressure at time  $t = 6.5$  s

Figure 6.10 shows the body at time  $t = 6.5$  s. The sphere is totally flat except for the center of the disk. The high pressure within the body leading to a pressure gradient towards the center of the disk is responsible for the swelling of the body.

The Euler equations tend to keep the volume constant. This is the reason for the flattening of the sphere. There is no mechanism in the equations being able to force the body back to its original shape.

#### 6.1.4 Validation

We test the method derived for the Euler part with an academic example. The reference body is the sphere with corresponding computational settings. We consider a rotation and divergence free velocity field

$$\mathbf{v}_0(\mathbf{x}) = 0.1 \cdot \begin{pmatrix} x_1 \\ -0.5x_2 \\ -0.5x_3 \end{pmatrix} \quad \forall \mathbf{x} \in \Omega.$$

Moreover, we assume that the density and the pressure are initially constant, i.e.  $\rho_0(\mathbf{x}) = 1.0$  and  $p_0(\mathbf{x}) = 2.0$  for all  $\mathbf{x} \in \Omega$ . Furthermore, we prescribe the pressure  $p(\mathbf{x}, t) = 2.0$  for all  $\mathbf{x} \in \partial\Omega$  at the boundary.

These initial and boundary conditions describe a solution  $\phi_e$  of the system (4.7) – (4.9). In particular, the solution is an equilibrium of the system, i.e.

$$\begin{aligned} \frac{D\rho_e}{Dt} &= 0.0 \\ \frac{D\mathbf{v}_e}{Dt} &= 0.0 \\ \frac{Dp_e}{Dt} &= 0.0, \end{aligned}$$

where the subscript  $e$  refers to solution  $\phi_e$ . Therefore, the density, the velocity and the pressure theoretically remain constant in time.

In Figure 6.11 we compare the analytical solution with the computed one over a period of 5.0 seconds. In the picture blue and red corresponds to density  $\rho$  and pressure  $p$ , respectively. The solid lines show the correct constant solutions of the respective quantities and the crosses show their approximations for an interior particle.

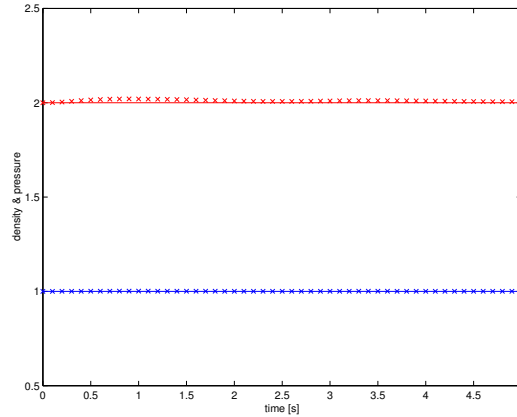


Figure 6.11: blue: density  $\rho$ , red: pressure  $p$

The constant functions are very well approximated. In this resolution, there is no visible difference between the approximation of the density and its true value. Moreover, the pressure computed with our method lies very close to the analytical one.

**Remark 6.3** *In this section we have basically confirmed the results of Kuhnert given in [24]. The observations have shown that the pressure gradient is the only system-inherent direction that leads to satisfying results.*

## 6.2 Results for the Shear Part

In this section we test the implementation of the dimensional upwinding given in Definition 5.2. For this purpose we apply an equation of state which is linear with respect to the internal energy and assume that

$$g = \left. \frac{\partial p}{\partial e} \right|_{\rho} = 10.$$

Furthermore, we have to specify the shear modulus  $\mu$  applied in equation (1.33). For testing, we assume that

$$\mu = 50.$$

The pictures in this section show in most cases the *maximal principle stress*  $\sigma_p$ , i.e. the largest eigenvalue of the stress tensor  $\sigma$ .



### 6.2.1 Shearing of a Sphere

We reconsider the geometry and the computational settings given in Section 6.1.2. Hence, the computational domain is a sphere of radius 5.

#### Boundary Conditions

According to the considerations in Section 5.2.4, we need to determine three boundary conditions. In the free-boundary problem we prescribe the normal stress. Let  $\mathbf{n}(\mathbf{x})$  be the outer normal vector to the surface in point  $\mathbf{x} \in \partial\Omega$  then

$$\sigma(\mathbf{x})\mathbf{n}(\mathbf{x}) = -p_o\mathbf{n}(\mathbf{x}) \quad \forall \mathbf{x} \in \partial\Omega,$$

where  $p_o = 10$  is the outer pressure.

#### Initial Conditions

The initial density is constant in space with  $\rho_0(\mathbf{x}) = 1$  for all  $\mathbf{x} \in \Omega$ . Furthermore, we prescribe a divergence- and rotation-free velocity field, namely

$$\mathbf{v}_0(\mathbf{x}) = 0.5 \cdot \begin{pmatrix} x_2 \\ x_1 \\ 0 \end{pmatrix} \quad \forall \mathbf{x} \in \Omega.$$

Additionally, we have to provide initial conditions for the stress  $\sigma$  which we assume to be constant in space. We require that

$$\sigma_0(\mathbf{x}) = -p_o I,$$

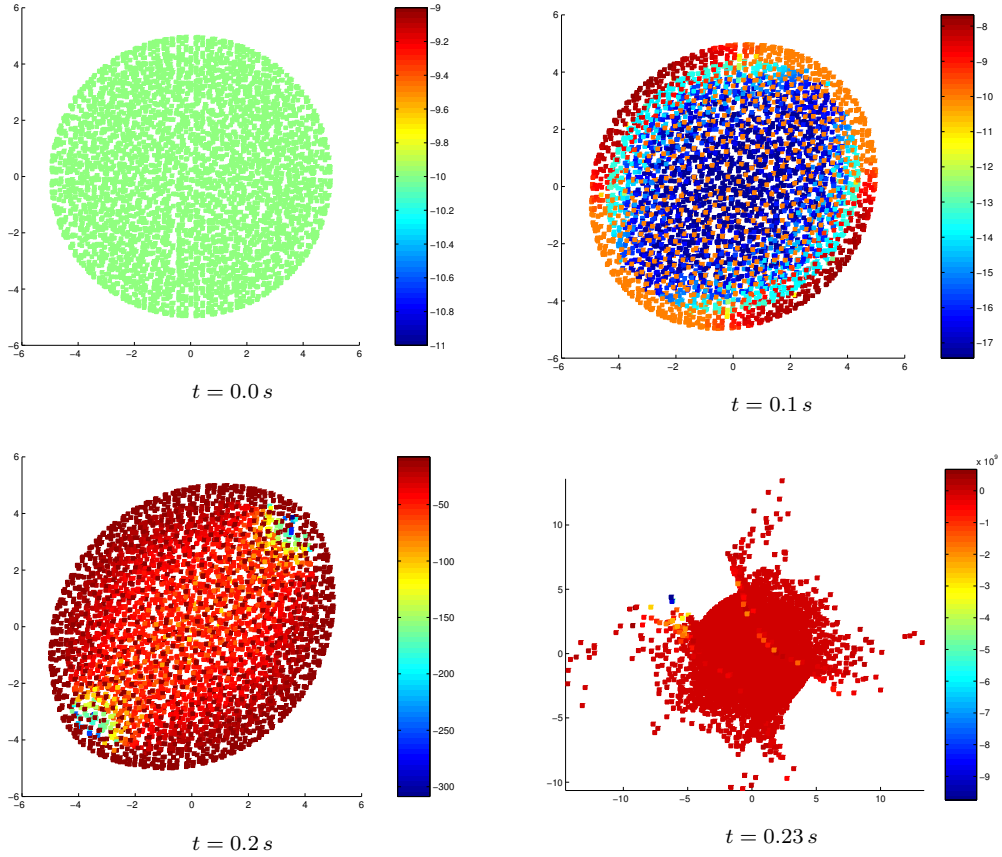
where  $p_o$  is again the outer pressure. Hence, the initial deviatoric stress  $S_0$  is equal to zero and  $\sigma_{p_0} = -10$ .

#### Results Using Central Differences

We first present the results for this setting using the central least squares approximation operator (3.11).

Figure 6.12 shows a sequence of pictures visualizing the maximal principal stress  $\sigma_p$ . The first picture displays the initial state with  $\sigma_p \equiv -10$ . The last picture shows  $\sigma_p$  at time  $t = 0.22$  s, where the computation breaks.

Already in the second picture we observe that the naive particle approximation is not able to correctly reproduce the physical processes. Due to the initial motion the body is stretched in direction of the velocity. This leads to a decrease of pressure and thus to an increase of the maximal principal stress. But in the picture the highest stress can be found at the boundary.

Figure 6.12:  $\sigma_p$  without upwinding

At time  $t = 0.2 s$ , the maximal tensile strength has already started to explode and ranges from below  $-300$  to above  $60$ . We conclude that this approach yields no stable method for the free-boundary problem. As a logical consequence the body goes to pieces at time  $t = 0.22 s$ .

### Results Using a Single Upwind Direction

In Section 5.2 we discussed the problems finding system-inherent directions for the shear part. However, we identified at least one such direction, namely the one which minimizes the quadratic form (5.27). Here, we present the results using the upwinded particle approximation in this direction.

Again, Figure 6.13 is a sequence of pictures showing the maximal principal stress. The pictures are taken every 0.1 second starting with the initial state.

In contrast to the previous computation, this approach is able to reproduce the increase of the maximal principal stress inside the body. The pictures at time  $t = 0.1 s$  and  $t = 0.2 s$  qualitatively show the behavior we expect from physics. However, the stress is noticeable high at time  $t = 0.2 s$ . A careful investigation

of the picture reveals a ring of high principal stresses around the light red core of the body. This is a first indication of beginning instabilities.

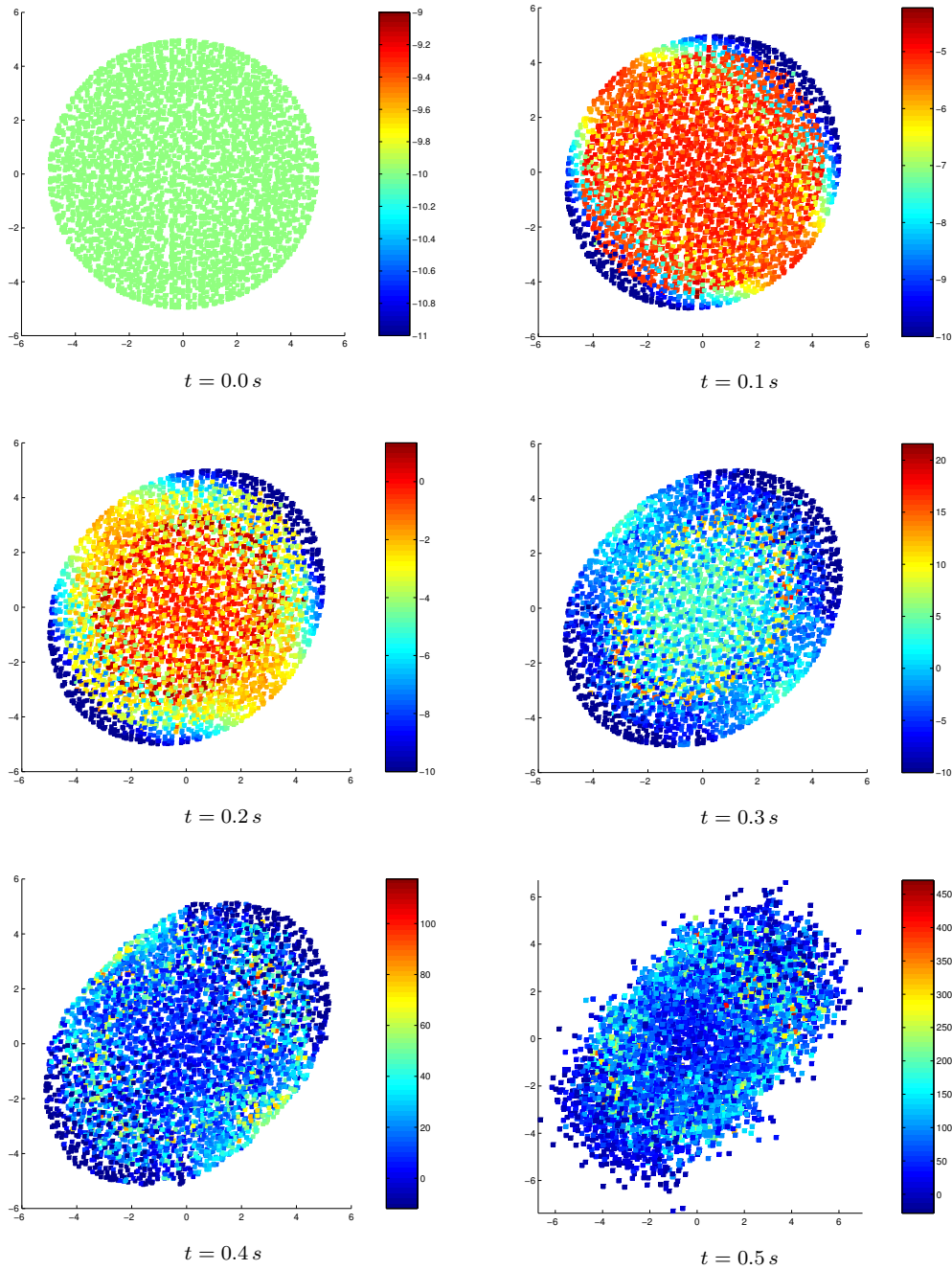


Figure 6.13:  $\sigma_p$  with upwinding in minimization direction

This impression proves true in the following picture. The maximal stress has increased up to more than 20 in the previously discovered ring. The last two pictures of Figure 6.13 display the breaking of the solid. We conclude, that upwinding in minimization direction is not stable for the shear part.

**Remark 6.4** *Additionally to this direction, we have tested the implementation of the one-directional upwinding method for other upwind directions. These are for example the principal stress directions and the gradient of the maximal principal stress. Unfortunately, none of them yield satisfying results.*

### Results Using Dimensional Upwinding

Finally, we present the results of the dimensional upwinding as stated in Section 5.2.3. The left column of Figure 6.14 displays the course of the maximal principal stresses for different times and the right column shows the corresponding pressures.

The pictures present the elastic sphere at times where the elongation is maximal. Due to the initial velocity the body is stretched in direction of the bisecting line of the  $x_1$ - and  $x_2$ -axis. The stresses within the ball revert the initial velocity such that the body is stretched in the direction normal to the bisecting line. This situation is shown in the picture for time  $t = 1.2$  s. At time  $t = 1.9$  s the expansion of the body is again in the original direction.

We note that the considerably high pressure shown in the right column of Figure 6.14 has no influence on the movement of the elastic body. But this is clearly a consequence of the applied splitting, since in the equation for the velocity (4.12) the pressure gradient is absent.

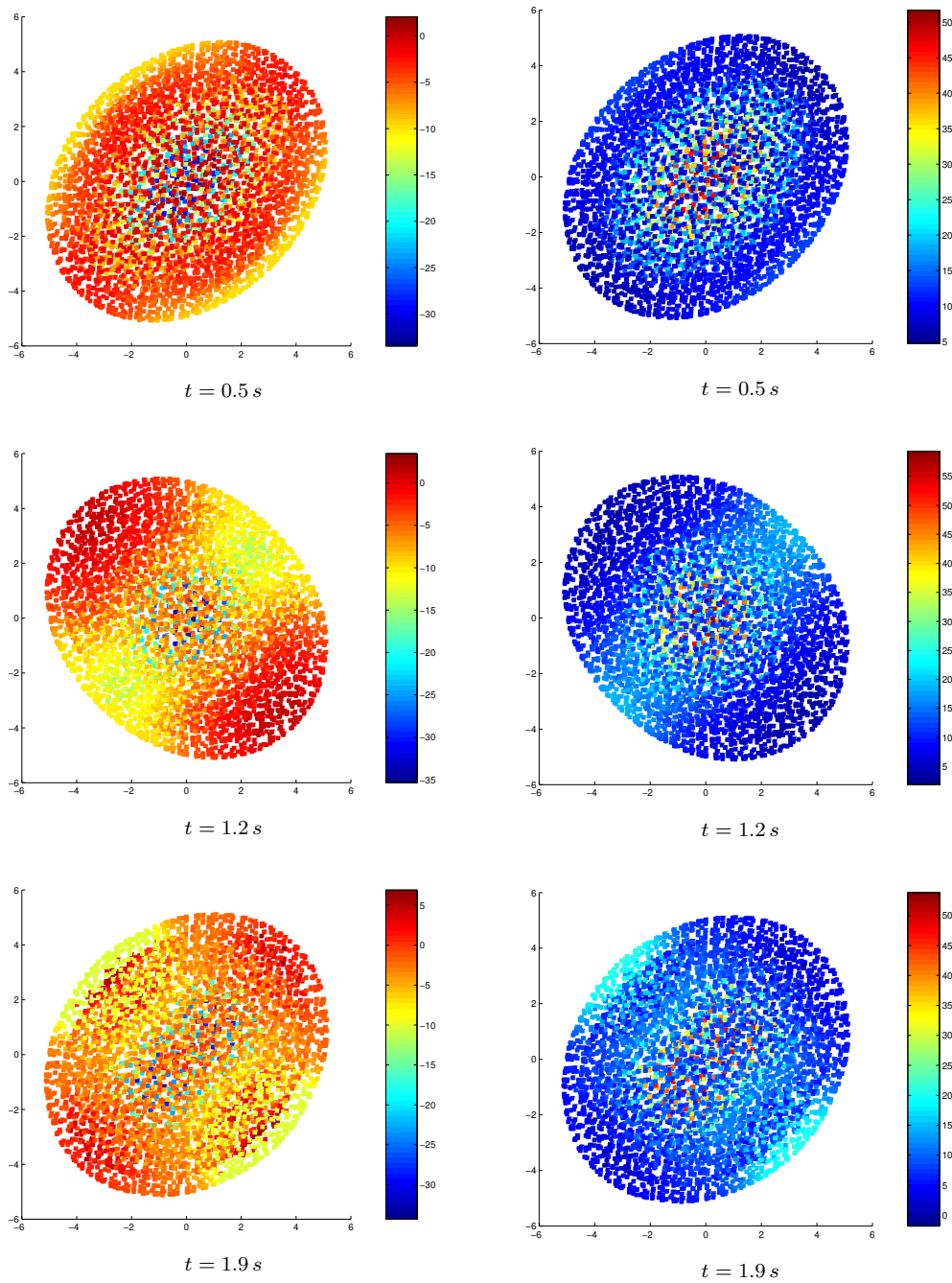
We have seen in Section 6.1.3 that the Euler part is not able to prevent the sphere from deforming. The equations only tend to keep the volume constant. In contrast to that, the shear part acts against the deformation of the initial configuration.

Let us investigate in detail the processes inside the solid. In Figure 6.15, the components  $S^{11}$ ,  $S^{22}$  and  $S^{33}$  of the deviatoric stress are shown for time  $t = 0.5$  s. Let  $\mathbf{n}^{(i)}$  be the  $i$ -th unit vector, then

$$S^{ii} = \mathbf{n}^{(i)T} S \mathbf{n}^{(i)} .$$

That means,  $S^{ii}$  is the force acting on a plane with normal  $\mathbf{n}^{(i)}$  in direction  $\mathbf{n}^{(i)}$ , reduced by the pressure contribution.

Let us consider the red region in the upper left of the pictures for  $S^{11}$  and  $S^{22}$ . The gradient of the components  $S^{11}$  and  $S^{22}$  of the deviatoric stress causes an acceleration of the solid in direction  $-\mathbf{n}^{(1)}$  and  $\mathbf{n}^{(2)}$ , respectively. Analogously, the other regions accelerate the particles into the corresponding directions. The stress acts against the deformation provoked by the initial velocity such that the solid attempts to regain its original shape.

Figure 6.14:  $\sigma_p$  and pressure with dimensional upwinding

At this stage the velocity points in the opposite direction than the initial velocity. Due to the inertia of the particles the solid does not stay in its original shape and is stretched in the direction normal to the bisecting line of the  $x_1$ - and  $x_2$ -axis. Thereby, the elastic body develops an oscillation.

Remarkable in Figure 6.15 is the fact that the motion of the solid leaves the initial  $x_1$ - $x_2$ -plane due to the contribution of  $S^{33}$ . Additionally to the oscillation

in the plane, the body starts vibrating in  $x_3$ -direction.

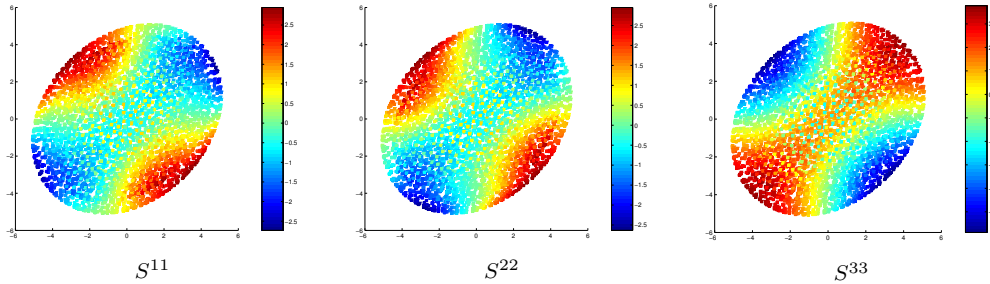


Figure 6.15:  $S^{11}$ ,  $S^{22}$  and  $S^{33}$  at time  $t = 0.5 s$

One could expect that the oscillation of the elastic solid stays in direction of the bisecting line and the direction normal to it. However, after some time other eigenmodes of the sphere are stimulated. This is shown in Figure 6.16 where the maximal principal stresses are displayed for time  $t = 2.8 s$  and time  $t = 3.5 s$ .

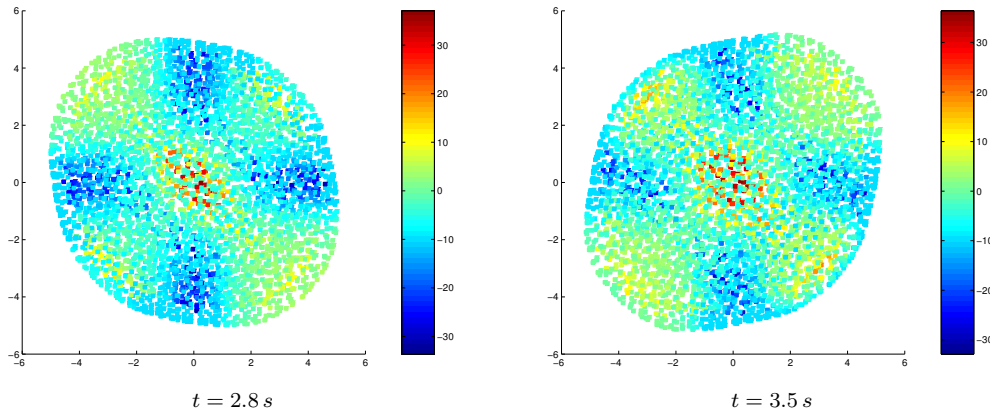


Figure 6.16:  $\sigma_p$  at time  $t = 2.8 s$  and  $t = 3.5 s$

The red core of the elastic solid in Figure 6.16 is due to the pressure having no influence on the motion of the body. In the coupled system we do not expect this behavior. Furthermore, we observe that the volume increases with time. This is also a consequence of the missing pressure term in the momentum equation.

*We conclude that the dimensional upwinding defined by (5.38) is reliable for the shear part.*

### 6.2.2 Validation

We test the method derived for the shear part with a further example. The reference body is the sphere with corresponding computational settings. For

this academic example we set  $g = 0$ . We consider a rotation and divergence free velocity field

$$\mathbf{v}_0(\mathbf{x}) = 0.1 \cdot \begin{pmatrix} x_2 \\ x_1 \\ 0.0 \end{pmatrix} \quad \forall \mathbf{x} \in \Omega.$$

Moreover, we assume that pressure, density and deviatoric stress are initially constant, i.e.  $\rho_0(\mathbf{x}) = 1.0$ ,  $p_0(\mathbf{x}) = 0.0$  and  $S_0(\mathbf{x}) = 0.0$  for all  $\mathbf{x} \in \Omega$ . Note that by this the initial strain rate tensor is constant. In this example, we prescribe the velocity at the boundary

$$\mathbf{v}(\mathbf{x}, t) = \mathbf{v}_0(\mathbf{x}) \quad \forall \mathbf{x} \in \partial\Omega.$$

The solution of the system (4.11) – (4.14) that corresponds to these initial and boundary conditions is given by

$$\begin{aligned} \rho(\mathbf{x}, t) &= \rho_0(\mathbf{x}) \\ \mathbf{v}(\mathbf{x}, t) &= \mathbf{v}_0(\mathbf{x}) \\ p(\mathbf{x}, t) &= p_0(\mathbf{x}) \\ S(\mathbf{x}, t) &= \begin{pmatrix} 0 & 0.2\mu t & 0 \\ 0.2\mu t & 0 & 0 \\ 0 & 0 & 0 \end{pmatrix}. \end{aligned}$$

Hence, except for  $S^{21}$  and thus  $S^{12}$ , all quantities are constant in time and space. The picture on the left of Figure 6.17 displays the evolution of  $S^{21}$  during 5.0 seconds. The solid line represents the analytical solution and the crosses its approximation.

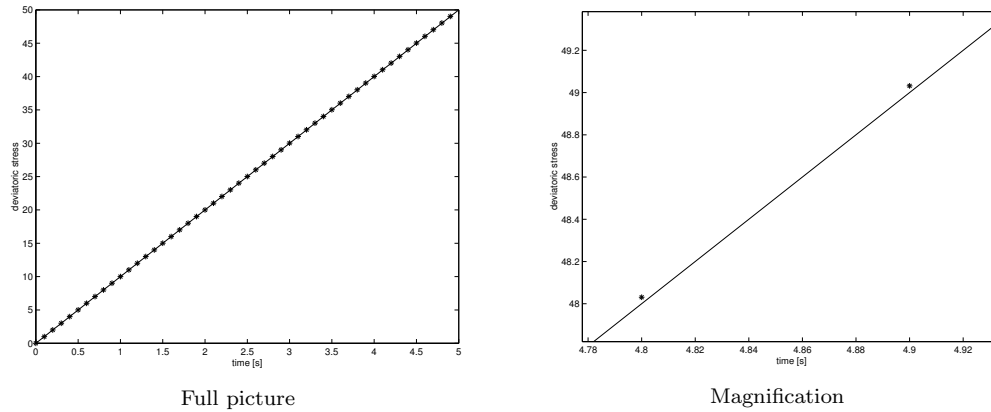


Figure 6.17: Evolution of  $S^{21}$

The proposed scheme shows very good approximation results for this academic example. The picture on the left suggest that the approximation and the true solution are identical. On the right of Figure 6.17 a magnification of a part of the curve is presented. Here, we can observe that the numerical solution is only very close to the true one.

**Remark 6.5** *The further validation turns out to be a difficult task since the system of equations describes only parts of a real solid. Consequently, comparative data are not available.*

### 6.3 Results for the Rotation Part

To close this chapter of results for the different subsystems, we consider the rotation of the deviatoric stress tensor. For each time step we assume a constant underlying velocity field. Thus, we are able to compute the stress  $S$  analytically by equation (5.58). In this section we compute the positions and velocities according to (5.55).

#### 6.3.1 Rotation of a Sphere

The geometry of the sphere and the computational settings are given in Section 6.1.2. We compute the evolution of the position, the velocity and the stress analytically. Hence, we do not prescribe any boundary conditions.

##### Initial Conditions

We assume that the initial density is constant with  $\rho_0(\mathbf{x}) = 1$  for all  $\mathbf{x} \in \Omega$ . Additionally, we prescribe a pure rotation around the  $x_3$ -axis, that is

$$\mathbf{v}_0(\mathbf{x}) = \begin{pmatrix} x_2 \\ -x_1 \\ 0 \end{pmatrix} \quad \forall \mathbf{x} \in \Omega.$$

We choose the initial stress  $\sigma_0$  in a way to visualize its rotation. The stress itself has no influence on the motion of the body.

$$\sigma_0(\mathbf{x}) = \begin{cases} \begin{pmatrix} 10 & 0 & 0 \\ 0 & -10 & 0 \\ 0 & 0 & 0 \end{pmatrix} & \text{for } x_1 < 0 \\ \bar{0} & \text{for } x_1 \geq 0, \end{cases}$$

where  $\bar{0}$  is a  $3 \times 3$ -matrix whose entries are equal to zero. Note that by this definition the initial pressure is equal to zero.

##### Results

In Figure 6.18 the maximal principal stresses are shown for different times. The last picture is taken at time  $t = 3.1$  s and corresponds approximately to half a rotation.



Obviously, the stress is rotated with the sphere as expected. The angular velocity is equal to 1 such that a complete rotation is fulfilled after  $T = 2\pi \approx 6.3$  s which corresponds to 6300 time steps.

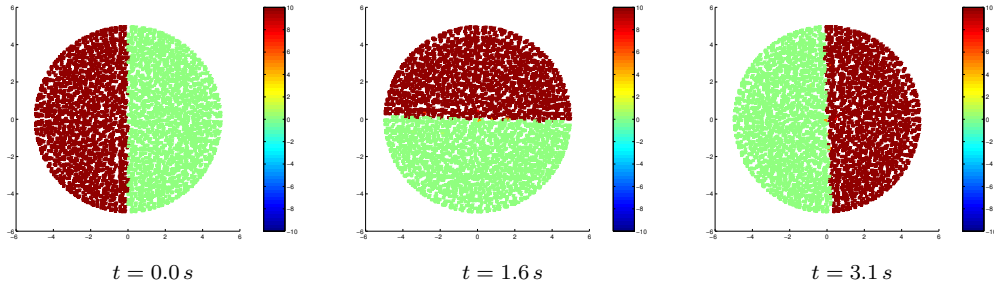


Figure 6.18: Rotation of the initial stress

To validate the computations we investigate the evolution of  $S^{11}$  and  $S^{21}$ . Let us consider the deviatoric stress  $S$  computed by (5.58) with  $M(t) = e^{Rt}$  for a particle with non-zero initial stress. Then  $S$  is given by

$$S(t) = M(t)S_0M^T(t) = 10 \cdot \begin{pmatrix} \cos(2\omega t) & -\sin(2\omega t) & 0 \\ -\sin(2\omega t) & -\cos(2\omega t) & 0 \\ 0 & 0 & 0 \end{pmatrix}, \quad (6.1)$$

where  $\omega = \sqrt{r_{21}^2 + r_{31}^2 + r_{32}^2} = 1$ . Hence,  $S^{11}$ ,  $S^{22}$  and  $S^{21}$  describe waves with an amplitude of 10 and double frequency.

Figure 6.19 shows the course of the two quantities within 12.5 seconds. The blue and the red curve correspond to  $S^{11}$  and  $S^{21}$ , respectively. The black vertical lines indicate the points in time of the pictures in Figure 6.18.

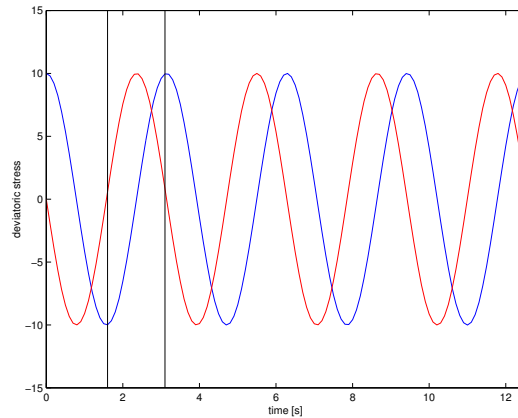


Figure 6.19: Evolution of  $S^{11}$  and  $S^{21}$

The stress shows exactly the behavior we expect from equation (6.1). The first vertical line from the right corresponds to half a rotation of the sphere. At that time the stress has already fulfilled a complete turn. Furthermore, the amplitude of the waves is equal to 10 and stays constant in time.



## Chapter 7

# Results for Coupled System

In this chapter we investigate the interaction of the different subsystems. We start with a rotation free example and consider the shear part together with the Euler part. After that we present the rotation of an elastic ball computed with the fully coupled system. The coupling of the subsystems has already been described in Section 5.4.

### Linear Equation of State

For iron and aluminum, the order of magnitude of  $c$  and  $g$  computed by the Tillotson equation of state (2.9) approximately is  $10^4$  as shown in Table 2.2, i.e.  $c, g \sim \mathcal{O}(10^4)$ . Furthermore, we have  $\sqrt{\mu/\rho} \sim \mathcal{O}(10^4)$ . Because of these magnitudes, the CFL-condition puts a severe restriction on the time step. For testing our implementation of the coupled system, we apply a linear equation with smaller sound speeds.

The assumption of a linear equation of state is motivated by Figure 7.1 showing the Tillotson pressure for iron for

$$\begin{aligned}\rho &\in [0.9 \cdot \rho_0, \dots, 1.1 \cdot \rho_0] \\ e &\in [0, \dots, 0.1 \cdot E_0],\end{aligned}$$

where  $E_0$  is one of the Tillotson parameters specified in Table 2.1. For small variations of the density and small internal energies the pressure shows approximately a linear behavior. Therefore, we apply the following equation of state:

$$p(\rho, e) := c^2 \rho + ge + p_0 - c^2 \rho_0, \quad (7.1)$$

where  $p_0$  is the normal pressure and  $\rho_0$  the corresponding density. Later, we will assume that  $p_0$  is equal to zero which corresponds to a stress-free reference configuration.

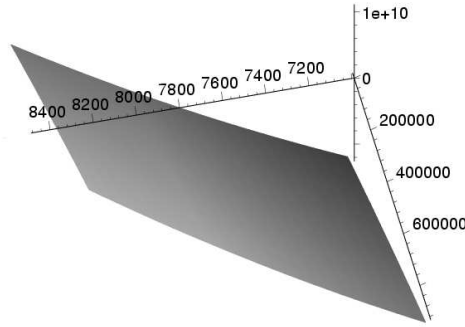


Figure 7.1: Equation of state for iron

The pressure equation (1.32) imposes restrictions on  $c$  and  $g$ . Recall that

$$\frac{Dp}{Dt} = - \left( \rho c^2 + \frac{g}{\rho} p \right) \operatorname{div}(\mathbf{v}) + \frac{g}{\rho} S^{ij} \varepsilon^{ij} \quad (7.2)$$

and consider a pure increase of volume. Then  $S$  remains zero and the pressure decreases. Note that in a solid the pressure can become negative. If at some time the expression in the brackets became negative then the pressure would increase despite the increase of volume. Therefore, we have to insure by a suitable choice of  $c$  and  $g$  that the expression remains positive during the whole computation.

**Remark 7.1** *In Section 6.2.1 we have only considered the shear part. In this case  $\rho c^2$  is missing in equation (7.2). Therefore, we have chosen an initial and outer pressure of 10 to prevent the term from becoming negative.*

## Geometry, Computational Settings and Boundary Conditions

We consider the sphere specified in Section 6.1.2 together with the corresponding computational settings. Furthermore, the boundary conditions for the Euler and the shear part are given in Section 6.1.2 and Section 6.2.1, respectively. We assume that the outer pressure  $p_o$  is equal to zero.

### 7.1 Shearing of a Sphere

In this section we reconsider the shearing of an elastic sphere already discussed in Section 6.2.1. In particular, we study the influence of the coupling with the Euler part on the results. The rotation of the stress tensor is neglected.

### Initial Conditions

The initial conditions for density, stress and velocity are

$$\begin{aligned}\rho_0(\mathbf{x}) &= 1, \\ \sigma_0(\mathbf{x}) &= -p_o I, \\ \mathbf{v}_0(\mathbf{x}) &= 0.5 \cdot \begin{pmatrix} x_2 \\ x_1 \\ 0 \end{pmatrix}\end{aligned}$$

for all  $\mathbf{x} \in \Omega$ , respectively, where the outer pressure  $p_o$  is equal to zero. Furthermore, it turns out that

$$c = 4.0 \quad \text{and} \quad g = 1.0$$

assures that the bracketed expression in (7.2) remains greater than zero during the whole computation. Furthermore, we study the influence of the size of the different parameters. Table 7.1 is a collection of different settings, where  $\mu$  is the shear modulus.

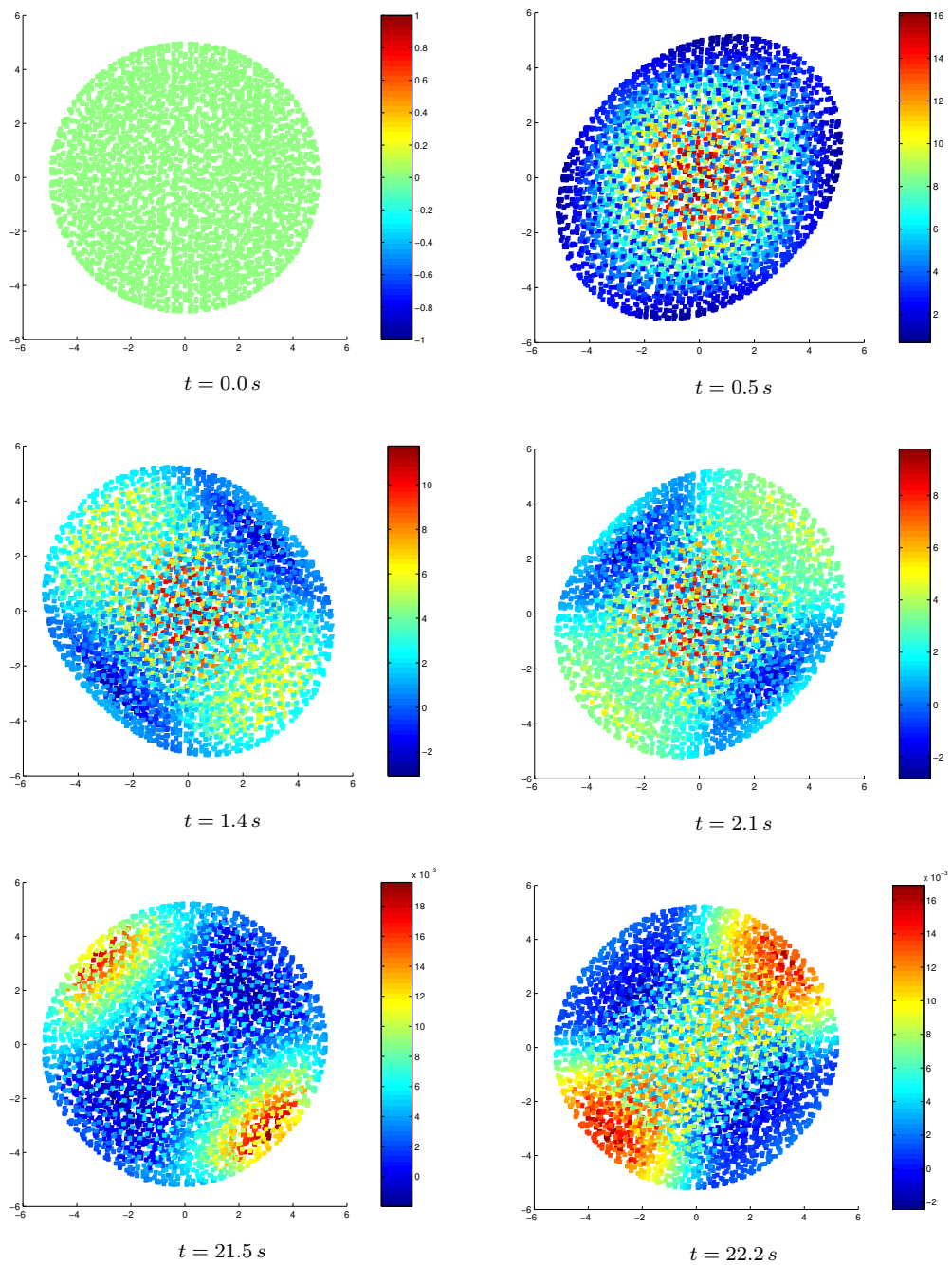
	$\mu$	$g$	$c$
Setting 1	50.0	1.0	4.0
Setting 2	10.0	1.0	4.0
Setting 3	50.0	1.0	10.0
Setting 4	50.0	1.0	1.0

Table 7.1: Parameters for (7.1)

### Results for Setting 1

We start with the results for the first setting. Figure 7.2 shows the maximum principal stress for different times. The first picture shows the initial state with  $\sigma_p \equiv 0$ . The following images are taken at times with maximal elongation of the body.

Due to the initial velocity the body is stretched in direction of the bisecting line of the  $x_1$ - and the  $x_2$ -axis. This situation is shown in the picture for time  $t = 0.5 s$ . The stress is maximal inside the body and reaches up to 16. As already described in Section 6.2.1 the stresses invert the initial motion leading to the situation visualized for time  $t = 1.4 s$ .

Figure 7.2:  $\sigma_p$  for setting 1

A first comparison with the results for the shear part given in Figure 6.14 reveals the following:

- The maximal absolute value of the principal stress is remarkably higher in the shear system than in the coupled system. The reason for this is that the pressure has no influence on the other

equations in system (4.11) – (4.14). In particular, the pressure gradient causes no acceleration of the particles. The pressure itself increases in an "undisturbed" way.

- In Figure 6.14 the maximal elongation of the solid is larger than in Figure 7.2. Furthermore, the stretched body is much thinner in the first case. Due to the stretching of the solid, the pressure decreases within the solid. Because of the boundary conditions, this results in a pressure gradient pointing outside the body. In the coupled system this gradient additionally acts against the initial motion. Therefore, the solid is not elongated as much as in Section 6.2.1, where the pressure term does not occur in the equations for the velocity.

This means that there are more terms in the coupled system that act against the deformation than in the subsystem considering exclusively the shear part.

The last row of Figure 7.2 shows the stress for later times. At these times the solid has approximately its original shape. The stresses are much smaller than in the beginning of the computation. The radius of the sphere is larger than the one of the original configuration.

The numerical viscosity of the system has used the initial velocity up. At this stage the particles fulfill nearly no motion. The initial kinetic energy of the body has been transformed to elastic energy. But the stress still oscillates as visualized by the two pictures.

Furthermore, we remark that in the shear example presented in Section 6.2.1 higher eigenmodes have been stimulated as shown in Figure 6.16. These modes can not be observed in the coupled system. Instead, the oscillation remains in the lowest natural frequency of the sphere.

### Comparison of the Different Settings

In the following we study the dependence of the results on the parameters  $c$ ,  $g$  and  $\mu$ . In Figure 7.3 and 7.4 the maximal principal stresses are displayed. The various settings stated in Table 7.1 are denoted by S1 – S4.

### Influence of the Shear Modulus $\mu$

We investigate the influence of the shear modulus  $\mu$  on the computation. In Figure 7.3 we compare the results for setting 1 with the ones for setting 2. The parameters  $c$  and  $g$  are the same for both settings.

The left picture shows the situation previously described for  $\mu = 50$ . The solid has the shape of a sphere whose radius is larger than the one of the initial geometry.

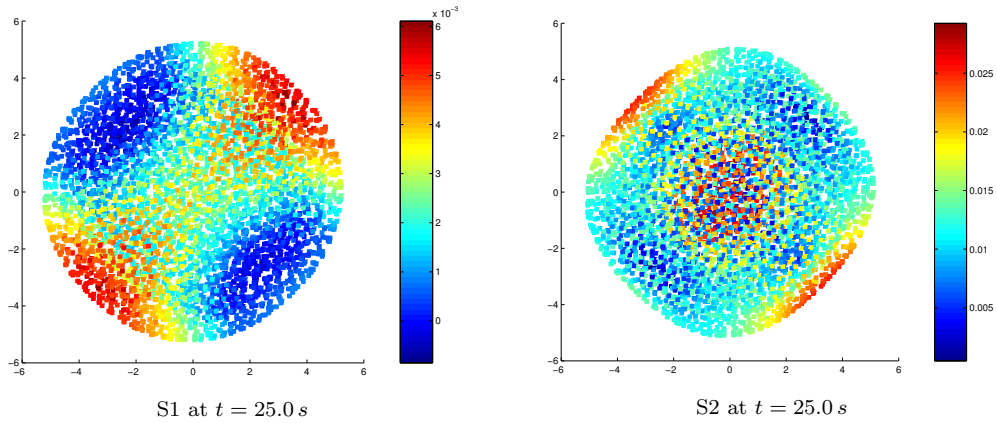


Figure 7.3: Comparison of setting 1 and 2

The deviatoric part of the stress tensor acts against any deformation of the reference configuration. In case of setting 2, the deviatoric stress is not large enough to compensate the deformation of the sphere. This is a consequence of the reduced shear modulus. From this results the shape of the elastic solid which is not completely circular.

### Influence of the Speed of Sound $c$

We keep  $\mu$  and  $g$  constant and vary  $c$  to investigate its influence on the motion of the solid. We consider the settings 1, 3 and 4 as specified in Table 7.1.

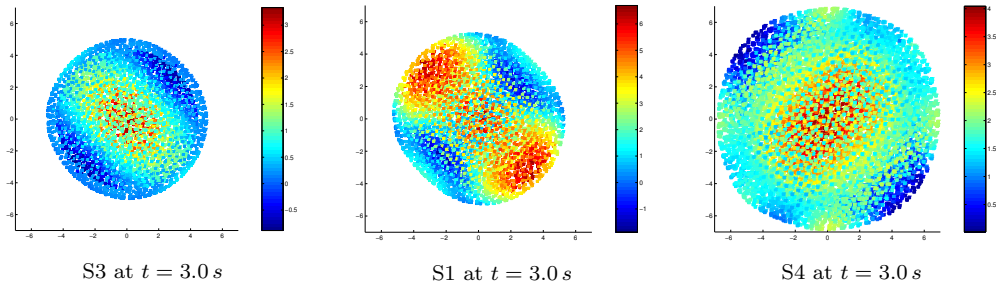


Figure 7.4: Comparison of setting 3, 1 and 4

Figure 7.4 shows the maximal principal stresses at time  $t = 3.0 s$  computed for the different settings. The sound speed  $c$  decreases from the left to the right.

In Section 6.1 we have investigated the behavior of the Euler part. Thereby, we have concluded that this subsystem acts against the changing of the volume of the body under consideration. This ambition to keep the volume constant can be seen in the above figure.

The influence of the Euler part increases with the speed of sound. Therefore, the sphere stays in a very compact form in case of setting 3. Consequently, the volume of the elastic body is higher in the remaining pictures in Figure 7.4.



The picture on the right of the figure is an exception. In this case the settings do not guarantee that the bracketed term in equation (7.2) is always greater than zero. Therefore, the body starts to gain more and more volume at later time.

*However, we conclude that the presented coupling of the different subsystems provides a numerical method being capable to simulate the shearing of an elastic ball. It has turned out that setting 1 given in Table 7.1 defines a suitable choice of parameters for testing the implementation.*

## 7.2 Rotation of a Sphere

In this section we consider the rotation of an elastic ball around the  $x_3$ -axis. Like in the previous example, the particles are moved in the shear part. We present the results for the fully coupled system.

### Initial Conditions and Equation of State

We prescribe a pure rotation. The density and the stress are initially constant throughout the solid. We have

$$\begin{aligned}\rho_0(\mathbf{x}) &= 1, \\ \sigma_0(\mathbf{x}) &= -p_o I, \\ \mathbf{v}_0(\mathbf{x}) &= 0.5 \cdot \begin{pmatrix} x_2 \\ -x_1 \\ 0 \end{pmatrix}\end{aligned}$$

for all  $\mathbf{x} \in \Omega$ , where the outer pressure  $p_o$  is equal to zero. We apply the linear equation of state (7.1) with coefficients

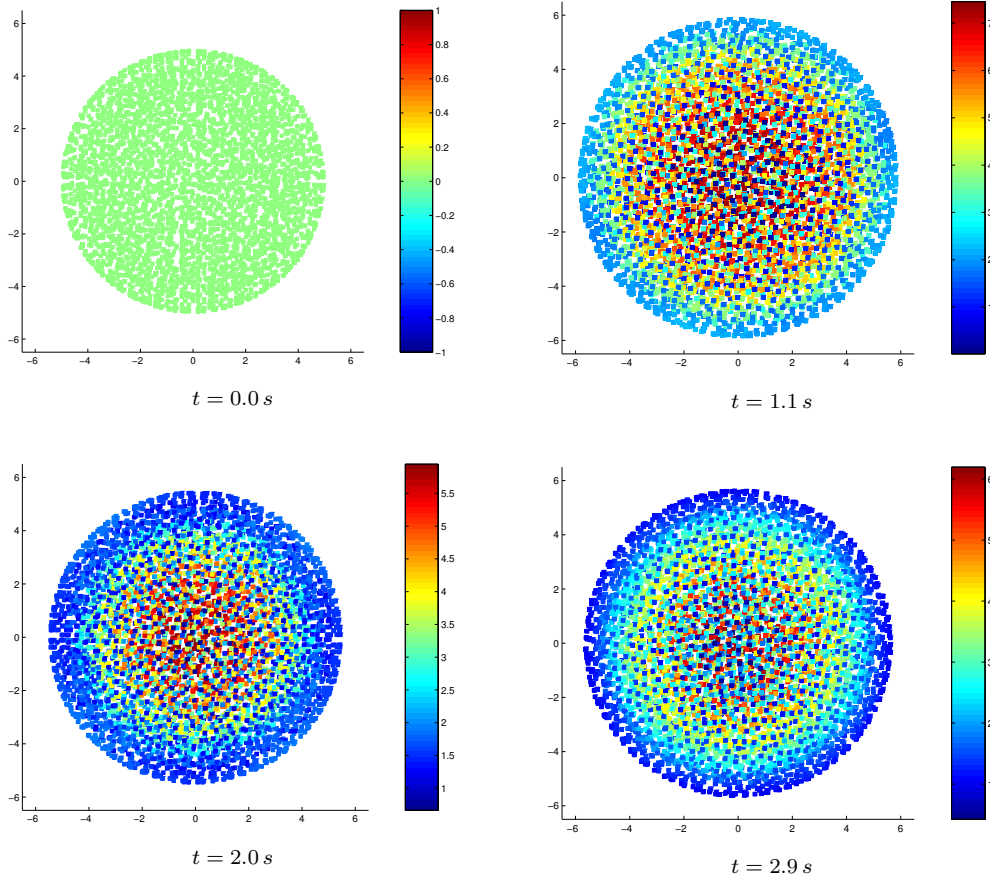
$$c = 4.0 \quad \text{and} \quad g = 1.0.$$

Furthermore, we assume that the shear modulus  $\mu$  is equal to 50.

### 7.2.1 Results

The pictures display the maximal principal stresses for different time. In Figure 7.5 we look onto the plane of rotation. The first picture displays the initial state.

In this view the initial velocity is tangential to the surface of the sphere. Because of the inertia of the particles the radius of the ball increases. Therefore, the stresses increase inside the body. At a certain point the stresses match the centrifugal forces and the swelling of the circumference is stopped. This situation is shown in the picture for time  $t = 1.1$  s.

Figure 7.5:  $\sigma_p$  for setting 1, top-view

Due to the high stresses the body is forced back to its original form. But the rotation prevents the solid from reaching its original size. The picture for time  $t = 2.0$  s displays the minimum of the circumference.

At time  $t = 2.9$  s the oscillation reaches another extremum, but the radius is not as large as for time  $t = 1.1$  s. In the  $x_1$ - $x_2$ -plane, the radius fulfills a damped oscillation. The reason for the decreasing amplitude is the viscosity introduced by the scheme. The damped oscillation will become better observable in Figure 7.8, where we present the course of the radius.

Figure 7.6 shows the results of the same computation but from a different viewpoint. We look in  $x_1$ -direction onto the rotating ball.

At first glance we observe that in the beginning the sphere extends in the  $x_3$ -direction. This surprises insofar as we expect that the swelling in the  $x_1$ - $x_2$ -plane comes along with a flattening in the  $x_3$ -direction. However, the picture for time  $t = 1.5$  s shows a different situation.

The stresses inside the solid are responsible for the stretching in direction of the rotation axis. More precisely, the off-diagonal elements of the stress tensor

disperse the sphere normal to the plane of rotation. We have already seen that the Euler part acts against the increase of the volume. It seems that the volumetric part can not "react fast enough" to compensate the elongation in  $x_3$ -direction.

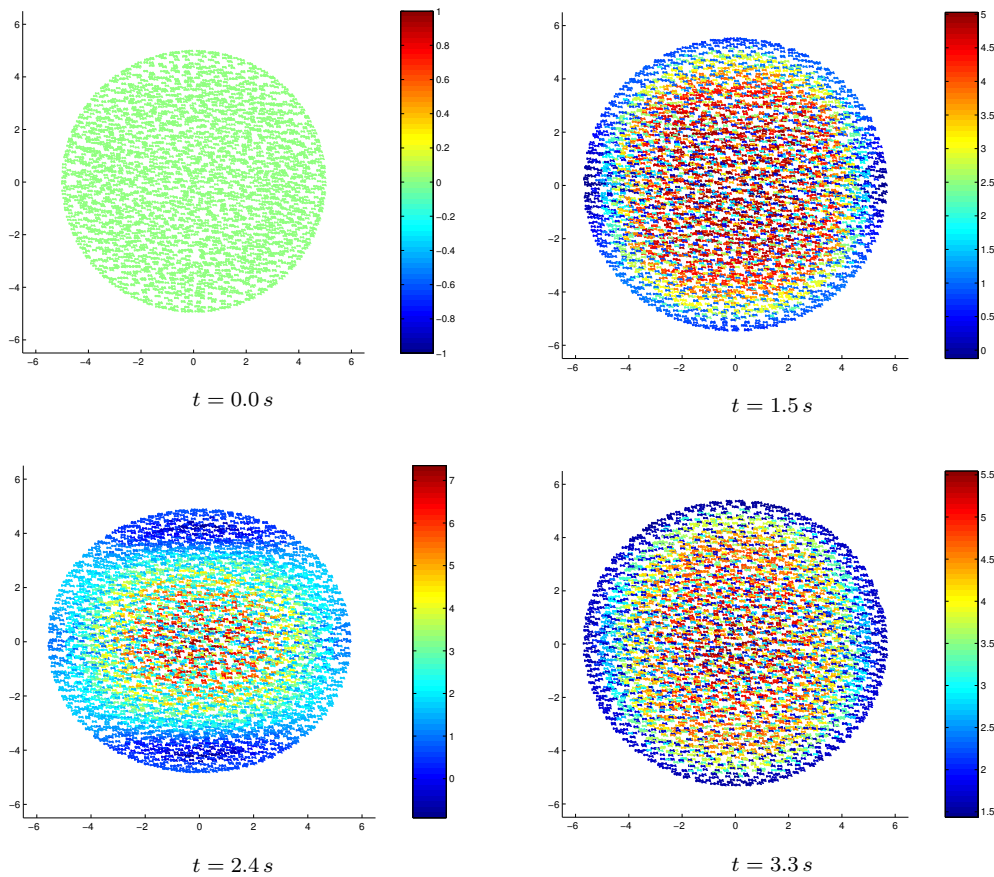
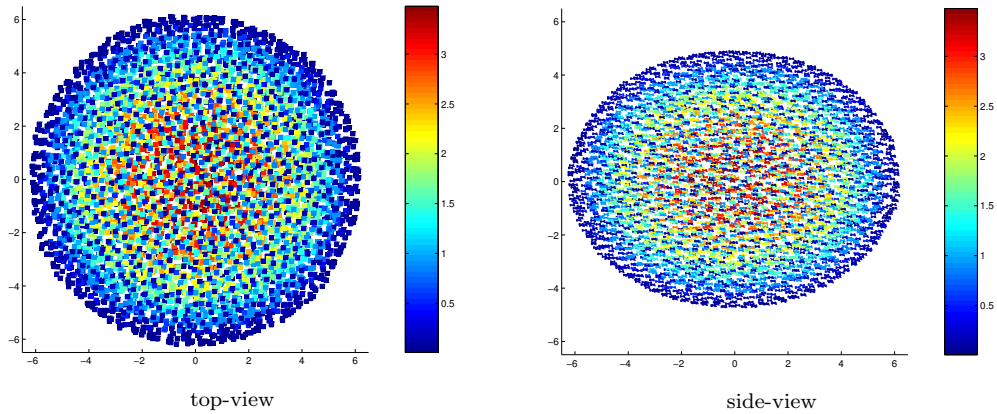


Figure 7.6:  $\sigma_p$  for setting 1, side-view

Anyhow, in the picture for time  $t = 2.4\text{ s}$  the solid has the form of an ellipse. The flattening of the sphere is due to the influence of the Euler part. Exactly like the radius in the  $x_1$ - $x_2$ -plane, the expansion in  $x_3$ -direction fulfills a damped oscillation.

As mentioned before, the damping of the oscillation is a consequence of the numerical viscosity. We expect therefore that the amplitudes decrease and that a stationary state is reached after some time. In particular, we suppose that the circumference of the sphere is smaller than the maximal one in Figure 7.5.

We will see that this supposition is only theoretically correct. Figure 7.7 shows the maximal principal stress  $\sigma_p$  for time  $t = 20.0\text{ s}$ . The left picture presents the look onto the plane of rotation whereas the right one shows the side of the solid. We make the following observations:

Figure 7.7:  $\sigma_p$  at  $t = 20.0 s$ 

- The circumference of the body is notably higher than the maximal one in Figure 7.5.
- The ellipse is much flatter than the one in Figure 7.6 at time  $t = 2.4 s$ .
- The surface of the body is not smooth. Single particles start to leave the particle ensemble.

**Remark 7.2** *The last point is a consequence of the fact, that in the present implementation FPM is only first order accurate in space. But computing the normal to a surface means essentially computing its gradient. Therefore, the approximation of the normals is zeroth order. In most cases, this does not influence the computations. Anyhow, in Figure 7.7, the surface partly shows a high curvature causing the instabilities at the boundary.*

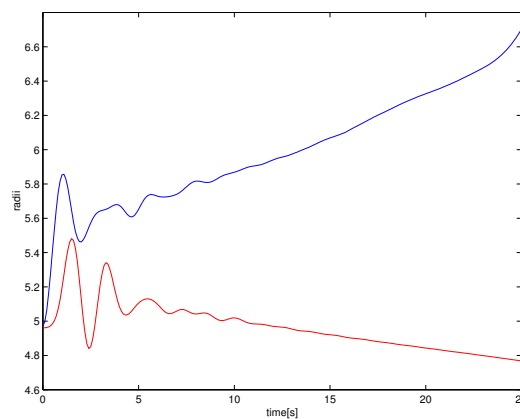


Figure 7.8: Course of radii

We study the first two points in more detail. For this purpose we consider the course of the radius of the sphere plotted in Figure 7.8. The blue line represents

the radius of the solid in the  $x_1$ - $x_2$ -plane. The red line shows the expansion of the body in  $x_3$ -direction. The picture displays 25 seconds.

In the figure, we clearly observe the initial oscillations. However, the blue curve exhibits a disturbance after approximately 4 seconds. At the moment, we are not sure about the reason for this behavior. In particular, we are not able to see whether this disturbance of the oscillation has a physical cause or not.

But the crucial observation is that the radius increases and the height decreases in time. In other words, the elastic solid becomes more and more flat and does not reach a stationary stage. This drastically conflicts with our expectation and requires further investigations. We describe two possible sources for this behavior:

1. We solve the rotation of the stress tensor analytically by equation (5.58). The velocity field and the particle positions are numerically integrated. But there are well-known problems concerning the integration of so-called *Hamiltonian systems* which need a special numerical treatment (see [38]).
2. In a pure rotation the stress exhibits a quadratic profile. Figure 7.9 shows the pressure for time  $t = 4.5$  s. The  $x$ -axis coincides with the  $x_1$ -axis and the  $y$ -axis displays the corresponding pressure. Our implementation is only first order accurate leading to an error in the approximation of the pressure gradient and of the divergence of the stress tensor.

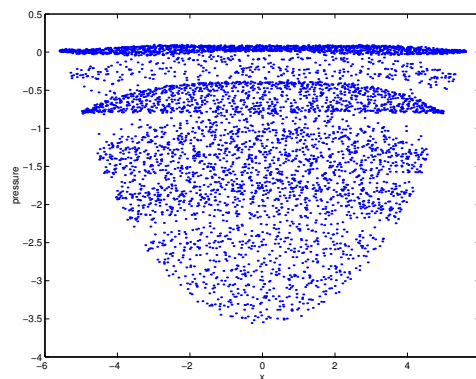


Figure 7.9: Pressure profile

**Remark 7.3** *In Figure 7.9 we notice a dark blue region on top of the picture. These are the boundary particles which all approximately have the same pressure due to the boundary conditions.*

## 7.2.2 Correction Strategies

In the following we want to investigate which of the two aspects mentioned before is responsible for the behavior observed in Figure 7.8.

### Analytical Computation of Rotation

The equation describing the update of the velocity is given by equation (5.47) in the shear part. Recall that

$$\frac{Dv_i}{Dt} = \frac{1}{\rho_0} \Pi_{uw}^D \frac{\partial S^{ij}}{\partial x_j}.$$

This relation includes the rotation of the velocity. Furthermore, the particles are moved with the dimensional velocity  $\mathbf{v}_{D_{uw}}$  in (5.52), that is

$$\frac{D\mathbf{x}}{Dt} = \mathbf{v}_{D_{uw}}.$$

To test whether the first point in the enumeration is responsible for the unphysical behavior we rewrite the equations as

$$\begin{aligned} \frac{Dv_i}{Dt} &= \left( \frac{1}{\rho_0} \Pi_{uw}^D \frac{\partial S^{ij}}{\partial x_j} - (R\mathbf{v})_i \right) + (R\mathbf{v})_i \\ \frac{D\mathbf{x}}{Dt} &= (\mathbf{v}_{D_{uw}} - R\mathbf{v}) + R\mathbf{v}, \end{aligned}$$

where  $(R\mathbf{v})_i$  is the  $i$ -th component of  $R\mathbf{v}$ . By this we separate the rotation of the velocity and the position from the other updates. This approach allows us to analytically rotate the vectors according to equation (5.55). The remaining updates of the quantities in brackets are performed numerically.

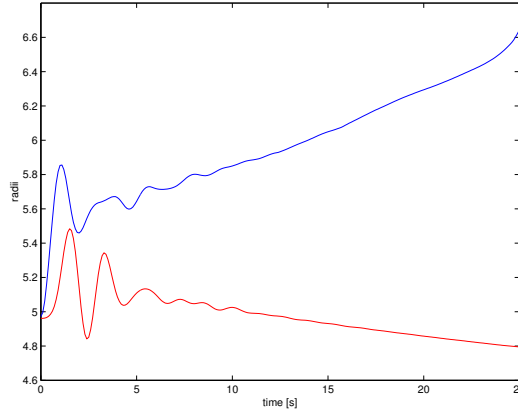


Figure 7.10: Course of radii, analytical correction

Figure 7.10 shows the course of the radii during 25 seconds. We observe no noticeable difference to the results of the previous computations. In particular, the two curves have the same slope as the ones in Figure 7.8.

*We conclude that the numerical time integration of the rotation is not the reason for the unphysical behavior of the body.*

### Correction of the Pressure Gradient

We investigate the influence of the pressure gradient on the results of the computations. In Figure 7.9 we have seen already that the pressure exhibits a parabolic profile. We consider an one-dimensional quadratic pressure distribution in  $x$  as sketched in Figure 7.11. In the picture  $\mathbf{s}$  denotes the secant through the points  $P_1 = (x_1, p(x_1))$  and  $P_2 = (x_2, p(x_2))$ .  $\mathbf{t}$  is a tangent in some point  $x_t$  parallel to  $\mathbf{s}$ .

We can interpret the secant as a first order approximation of the pressure. The secant has a constant slope, that means that its derivative is constant. In contrast to that the gradient of the true pressure increases from  $x_1$  to  $x_2$ . Only in the point  $x_t$ ,  $\mathbf{s}$  and  $\mathbf{t}$  have the same slope.

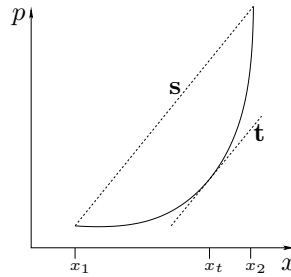


Figure 7.11: Approximation of pressure gradient

From the picture we see, that the approximation of the gradient is always too large in the interval  $(x_1, x_t)$  and too small in  $(x_t, x_2)$ . Transferring this observation to the pressure distribution in a rotating solid as displayed in Figure 7.9, we conclude that the approximation of the gradient is too small near the boundary.

We suspect that this effect causes the increase of the radius of the sphere. The height of the solid indicated by the red curve decreases due to the influence of the volumetric part.

To support this presumption, we modify the pressure gradient in the momentum equation of the Euler part (5.18) by

$$\nabla p_{uw}^m := \nabla p_{uw} \pm \delta_p h \|\nabla p_{uw}\| \frac{\mathbf{x}}{\|\mathbf{x}\|},$$

where  $\delta_p$  is a tuning parameter for the correction and  $h$  is the smoothing length. The sign of the correction depends on the kind of error we make in the approximation of the pressure gradient according to Figure 7.11.

**Remark 7.4** *Note that the presented correction term is not the result of a straightforward mathematical analysis. It is intuitively chosen to check whether the first order approximation is responsible for the observed phenomenon*

Figure 7.12 shows the course of the radii with modification of the pressure gradient. In this example we have chosen  $\delta_p = 0.5$  and observe the following:

- The correction acts against the numerical viscosity. The oscillation shows a much lower damping. In particular, the red curve has notably higher amplitudes.
- By this choice of correction, we do not succeed to prevent the solid from diverging. Anyhow, the circumference of the initial sphere increases much slower than in the uncorrected case.

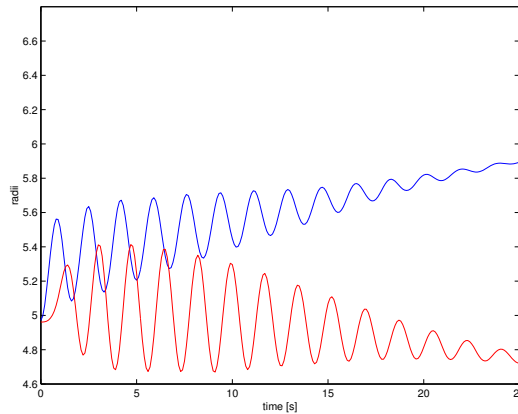


Figure 7.12: Course of radii, pressure modification

These observations confirm the presumption that the first order approximation of pressure and of stress causes the observed phenomenon. To give a numerical proof of the statement, a second order implementation is required which is not available at the moment.

**Remark 7.5** *In consideration of the fact that a simple first-order explicit time integration has been applied, the results are very satisfactory. We have shown already in [35] that a central particle approximation is not able to simulate even one single rotation. We assume that the results become even better with higher order approximations of the spatial derivatives.*

### 7.2.3 Approximation Properties

For the present example, no analytical solution is available at the moment. However, to study the approximation properties we describe an approach based on asymptotic expansion as discussed in [9]. Consider a fixed equidistant mesh with mesh-size  $\Delta x$ .

Let  $\phi^{exact}(\mathbf{x})$  be the analytical solution of a partial differential equation. Let  $\phi^{num}(\Delta x)$  be the vector of discrete values of the numerical solution of the equation on the mesh and  $\phi^{num}(\mathbf{x}, \Delta x)$  be its smooth approximation. We assume



that the approximation error has an asymptotic expansion of the form

$$e(\mathbf{x}, \Delta x) = e_1(\mathbf{x})\Delta x^{p_1} + \mathcal{O}(\Delta x^{p_2}) \quad \text{with} \quad p_1 < p_2, \quad (7.3)$$

where  $e_1$  is independent of  $\Delta x$ . For the following, let

$$e_2(\mathbf{x}, \Delta x) := e(\mathbf{x}, \Delta x) - e_1(\mathbf{x})\Delta x^{p_1},$$

then we know by equation (7.3) that  $e_2(\mathbf{x}, \Delta x)$  can be uniformly estimated by

$$|e_2(\mathbf{x}, \Delta x)| \leq C\Delta x^{p_2}, \quad (7.4)$$

where  $C$  is a constant that is independent of  $\mathbf{x}$  and  $\Delta x$ . We rewrite the numerical solution of the differential equation as

$$\phi^{num}(\mathbf{x}, \Delta x) = \phi^{exact}(\mathbf{x}) + \underbrace{e_1(\mathbf{x})\Delta x^{p_1} + e_2(\mathbf{x}, \Delta x^{p_1})}_{e(\mathbf{x}, \Delta x)}.$$

Let  $\Delta x_1 < \Delta x_2 < \Delta x_3$  be three different spatial discretizations and  $\mathcal{G}_i$  be an index set of all nodes of the mesh corresponding to mesh-size  $\Delta x_i$ . We define vectors of discrete values  $\phi^{num}(\mathcal{G}_i, \Delta x_j)$  and  $\mathbf{e}_2(\mathcal{G}_i, \Delta x_j)$  as

$$\begin{aligned} \phi_k^{num}(\mathcal{G}_i, \Delta x_j) &:= \phi^{num}(\mathbf{x}_k, \Delta x_j) & \text{with} \quad k \in \mathcal{G}_i. \\ \mathbf{e}_{2k}(\mathcal{G}_i, \Delta x_j) &:= \mathbf{e}_2(\mathbf{x}_k, \Delta x_j) \end{aligned}$$

That means that  $\phi^{num}(\mathcal{G}_i, \Delta x_j)$  is the numerical solution obtained using the mesh  $j$  evaluated at the nodes of mesh  $i$ . Analogously, we define  $\phi^{exact}(\mathcal{G}_i)$  and  $\mathbf{e}_1(\mathcal{G}_i)$  component-wise as

$$\begin{aligned} \phi_k^{exact}(\mathcal{G}_i) &:= \phi^{exact}(\mathbf{x}_k) & \text{with} \quad k \in \mathcal{G}_i \\ \mathbf{e}_{1k}(\mathcal{G}_i) &:= \mathbf{e}_1(\mathbf{x}_k) \end{aligned}$$

Hence, the analytical solution is evaluated at the nodes of mesh  $i$ . The following diagram visualizes this proceeding.

$$\begin{array}{ccccc} \phi^{num}(\Delta x_j) & \longrightarrow & \phi^{num}(\mathbf{x}, \Delta x_j) & \longrightarrow & \phi^{num}(\mathcal{G}_i, \Delta x_j) \\ & & \mathbf{e}_2(\mathbf{x}, \Delta x_j) & \longrightarrow & \mathbf{e}_2(\mathcal{G}_i, \Delta x_j) \\ & & \phi^{exact}(\mathbf{x}) & \longrightarrow & \phi^{exact}(\mathcal{G}_i) \\ & & \mathbf{e}_1(\mathbf{x}) & \longrightarrow & \mathbf{e}_1(\mathcal{G}_i) \\ \text{discrete on } \mathcal{G}_j & & \text{continuous} & & \text{discrete on } \mathcal{G}_i \end{array}$$

By this we are able to compare the analytical and the respective numerical solutions on the coarsest grid  $\mathcal{G}_3$ . The order of approximation can be computed by means of the following lemma.

**Lemma 7.1** *Let  $\Delta x_1 < \Delta x_2 < \Delta x_3$  be three different mesh-sizes with fixed ratios, let  $\phi^{num}(\mathcal{G}_3, \Delta x_j)$  be defined as above and let  $\|\mathbf{e}_1(\mathcal{G}_3)\|_q > e_1^0 > 0$  for all  $\Delta x_3$ . Then*

$$\frac{\|\phi^{num}(\mathcal{G}_3, \Delta x_3) - \phi^{num}(\mathcal{G}_3, \Delta x_2)\|_q}{\|\phi^{num}(\mathcal{G}_3, \Delta x_2) - \phi^{num}(\mathcal{G}_3, \Delta x_1)\|_q} = \frac{(\Delta x_3^{p_1} - \Delta x_2^{p_1})}{(\Delta x_2^{p_1} - \Delta x_1^{p_1})} + \mathcal{O}(\Delta x_3^{p_2-p_1}) \quad (7.5)$$

where  $\|\cdot\|_q$  is a norm fulfilling the normalization condition

$$\|\mathbb{I}\|_q = 1 \quad \text{with} \quad \mathbb{I} := \{\mathbf{1}\}^N,$$

where  $N$  is the number of nodes of grid  $\mathcal{G}_3$ .

*Proof:*

The proof is divided into two steps: estimation of the norm  $\|\cdot\|_q$  and the error estimation on the right of equation (7.5).

- Step 1:

We show that

$$\|\phi^{num}(\mathcal{G}_3, \Delta x_3) - \phi^{num}(\mathcal{G}_3, \Delta x_2)\|_q = r_e(\Delta x_3^{p_1} - \Delta x_2^{p_1}) + \mathcal{O}(\Delta x_3^{p_2}),$$

where  $r_e := \|\mathbf{e}_1(\mathcal{G}_3)\|_q$ .

*Proof:*

$$\begin{aligned} & \|\phi^{num}(\mathcal{G}_3, \Delta x_3) - \phi^{num}(\mathcal{G}_3, \Delta x_2)\|_q \\ &= \|\mathbf{e}_1(\mathcal{G}_3)(\Delta x_3^{p_1} - \Delta x_2^{p_1}) + \mathbf{e}_2(\mathcal{G}_3, \Delta x_3) + \mathbf{e}_2(\mathcal{G}_3, \Delta x_2)\|_q \\ &\leq \|\mathbf{e}_1(\mathcal{G}_3)(\Delta x_3^{p_1} - \Delta x_2^{p_1})\|_q + \|\mathbf{e}_2(\mathcal{G}_3, \Delta x_3)\|_q + \|\mathbf{e}_2(\mathcal{G}_3, \Delta x_2)\|_q \\ &= (\Delta x_3^{p_1} - \Delta x_2^{p_1})\|\mathbf{e}_1(\mathcal{G}_3)\|_q + \|\mathbf{e}_2(\mathcal{G}_3, \Delta x_3)\|_q + \|\mathbf{e}_2(\mathcal{G}_3, \Delta x_2)\|_q \\ &= r_e(\Delta x_3^{p_1} - \Delta x_2^{p_1}) + \|\mathbf{e}_2(\mathcal{G}_3, \Delta x_3)\|_q + \|\mathbf{e}_2(\mathcal{G}_3, \Delta x_2)\|_q \end{aligned}$$

According to equation (7.4),  $\|\mathbf{e}_2(\mathcal{G}_3, \Delta x_i)\|_q$  can be estimated by

$$\|\mathbf{e}_2(\mathcal{G}_3, \Delta x_i)\|_q \leq C\|\Delta x_i^{p_2}\mathbb{I}\|_q = C\Delta x_i^{p_2}$$

where  $C$  is independent of  $\mathcal{G}_3$ . Hence,  $\|\mathbf{e}_2(\mathcal{G}_3, \Delta x_i)\|_q \sim \mathcal{O}(\Delta x_i^{p_2})$ . From that derives

$$\|\mathcal{O}(\mathcal{G}_3, \Delta x_3^{p_2})\|_q + \|\mathcal{O}(\mathcal{G}_3, \Delta x_2^{p_2})\|_q = \mathcal{O}(\Delta x_3^{p_2}),$$

since  $\Delta x_3^{p_2} > \Delta x_2^{p_2}$ . This concludes this part of the proof.  $\square$

Analogously, we can show that

$$\|\phi^{num}(\mathcal{G}_3, \Delta x_2) - \phi^{num}(\mathcal{G}_3, \Delta x_1)\|_q = r_e(\Delta x_2^{p_1} - \Delta x_1^{p_1}) + \mathcal{O}(\Delta x_2^{p_2}).$$

Hence,

$$\frac{\|\phi^{num}(\mathcal{G}_3, \Delta x_3) - \phi^{num}(\mathcal{G}_3, \Delta x_2)\|_q}{\|\phi^{num}(\mathcal{G}_3, \Delta x_2) - \phi^{num}(\mathcal{G}_3, \Delta x_1)\|_q} = \frac{r_e(\Delta x_3^{p_1} - \Delta x_2^{p_1}) + \mathcal{O}(\Delta x_3^{p_2})}{r_e(\Delta x_2^{p_1} - \Delta x_1^{p_1}) + \mathcal{O}(\Delta x_2^{p_2})}.$$

Furthermore, we note that

$$0 < e_1^0 < r_e = \|\mathbf{e}_1(\mathcal{G}_3)\|_q \leq \|\|\mathbf{e}_1(\mathcal{G}_3)\|_\infty \mathbb{I}\|_q = \|\mathbf{e}_1(\mathcal{G}_3)\|_\infty,$$

where the first two inequalities is due to assumption. Hence,  $r_e \sim \mathcal{O}(1)$ , since all entries of  $\mathbf{e}_1(\mathcal{G}_3)$  are independent of the mesh-sizes  $\Delta x_i$ .

- Step 2:

We show that

$$\frac{r_e(\Delta x_3^{p_1} - \Delta x_2^{p_1}) + \mathcal{O}(\Delta x_3^{p_2})}{r_e(\Delta x_2^{p_1} - \Delta x_1^{p_1}) + \mathcal{O}(\Delta x_2^{p_2})} = \frac{\Delta x_3^{p_1} - \Delta x_2^{p_1}}{\Delta x_2^{p_1} - \Delta x_1^{p_1}} + \mathcal{O}(\Delta x_3^{p_2-p_1}).$$

Proof:

Let

$$err := \frac{r_e(\Delta x_3^{p_1} - \Delta x_2^{p_1}) + \mathcal{O}(\Delta x_3^{p_2})}{r_e(\Delta x_2^{p_1} - \Delta x_1^{p_1}) + \mathcal{O}(\Delta x_2^{p_2})} - \frac{\Delta x_3^{p_1} - \Delta x_2^{p_1}}{\Delta x_2^{p_1} - \Delta x_1^{p_1}},$$

then we have to show that  $err \sim \mathcal{O}(\Delta x_3^{p_2-p_1})$ . We consider fixed ratios of the mesh-sizes  $\Delta x_i$ . Hence, we find positive numbers  $a_1, a_2 \in \mathbb{R}^+$  such that

$$\Delta x_3 = a_1 \Delta x_2 \quad \text{and} \quad \Delta x_1 = a_2 \Delta x_2$$

with  $a_1 > 1$  and  $a_2 < 1$ . Therefore, we can conclude that  $\mathcal{O}(\Delta x_3^{p_2}) = \mathcal{O}(\Delta x_2^{p_2})$ . We have

$$\begin{aligned} err &= \frac{r_e(\Delta x_3^{p_1} - \Delta x_2^{p_1}) + \mathcal{O}(\Delta x_3^{p_2})}{r_e(\Delta x_2^{p_1} - \Delta x_1^{p_1}) + \mathcal{O}(\Delta x_2^{p_2})} - \frac{\Delta x_3^{p_1} - \Delta x_2^{p_1}}{\Delta x_2^{p_1} - \Delta x_1^{p_1}} \\ &= \frac{r_e \Delta x_2^{p_1} (a_1^{p_1} - 1) + \mathcal{O}(\Delta x_2^{p_2})}{r_e \Delta x_2^{p_1} (1 - a_2^{p_1}) + \mathcal{O}(\Delta x_2^{p_2})} - \frac{\Delta x_2^{p_1} (a_1^{p_1} - 1)}{\Delta x_2^{p_1} (1 - a_2^{p_1})} \\ &= \frac{r_e (a_1^{p_1} - 1) + \mathcal{O}(\Delta x_2^{p_2-p_1})}{r_e (1 - a_2^{p_1}) + \mathcal{O}(\Delta x_2^{p_2-p_1})} - \frac{a_1^{p_1} - 1}{1 - a_2^{p_1}} \end{aligned}$$

Note that  $\mathcal{O}(\Delta x^p)$  defines a class of functions with the same asymptotic behavior for  $\Delta x^p \rightarrow 0$ . Hence, we find functions

$$g_1(\Delta x_2), g_2(\Delta x_2) \sim \mathcal{O}(\Delta x_2^{p_2-p_1})$$

such that

$$\begin{aligned} err &= \frac{r_e (a_1^{p_1} - 1) + g_1(\Delta x_2)}{r_e (1 - a_2^{p_1}) + g_2(\Delta x_2)} - \frac{a_1^{p_1} - 1}{1 - a_2^{p_1}} \\ &= \frac{g_1(\Delta x_2)(1 - a_2^{p_1}) - g_2(\Delta x_2)(a_1^{p_1} - 1)}{[r_e (1 - a_2^{p_1}) + g_2(\Delta x_2)](1 - a_2^{p_1})} \\ &= \frac{g_1(\Delta x_2) - g_2(\Delta x_2)(a_1^{p_1} - 1)/(1 - a_2^{p_1})}{r_e (1 - a_2^{p_1}) + g_2(\Delta x_2)}. \end{aligned}$$

We know by assumption that  $r_e > e_1^0 > 0$  for all  $\Delta x_2$ . Therefore,  $r_e \geq e_1^0$  in the limit  $\Delta x_2 \rightarrow 0$  due to continuity reasons. Hence, the asymptotic behavior of the denominator is determined by  $r_e(1 - a_2^{p_1})$ . We conclude that

$$\frac{1}{r_e(1 - a_2^{p_1}) + g_2(\Delta x_2)} \sim \mathcal{O}(1) \quad \implies \quad \left| \frac{1}{r_e(1 - a_2^{p_1}) + g_2(\Delta x_2)} \right| \leq M$$

for  $\Delta x_2$  small enough, where  $M \in \mathbb{R}^+$  is some positive constant. The desired result follows from the asymptotic behavior of the respective terms. We have

$$\begin{aligned} err &= \left| \left( g_1(\Delta x_2) - g_1(\Delta x_2) \cdot \frac{a_1^{p_1} - 1}{1 - a_2^{p_1}} \right) \cdot \frac{1}{r_e(1 - a_2^{p_1}) + g_2(\Delta x_2)} \right| \\ &\leq \left( |g_1(\Delta x_2)| + |g_1(\Delta x_2)| \cdot \left| \frac{a_1^{p_1} - 1}{1 - a_2^{p_1}} \right| \right) \cdot \left| \frac{1}{r_e(1 - a_2^{p_1}) + g_2(\Delta x_2)} \right| \\ &\leq M \left( c_1 \Delta x_2^{p_2 - p_1} + c_2 \Delta x_2^{p_2 - p_1} \right) = \tilde{M} \Delta x_2^{p_2 - p_1}, \end{aligned}$$

where  $c_1$ ,  $c_2$  and  $\tilde{M}$  are positive constants. Hence,  $err \sim \mathcal{O}(\Delta x_2^{p_2 - p_1})$  or equivalently  $err \sim \mathcal{O}(\Delta x_3^{p_2 - p_1})$ . This concludes the second part of the proof.  $\square$

Combining the results of the two steps proves equation (7.5) and thus the lemma.  $\square$

Thereby, we are able to compute approximately the order  $p_1$  with the help of three different numerical solutions corresponding to the respective mesh-sizes. Let

$$\alpha(p_1) := \frac{(\Delta x_3^{p_1} - \Delta x_2^{p_1})}{(\Delta x_2^{p_1} - \Delta x_1^{p_1})},$$

then

$$\frac{d\alpha(p_1)}{dp_1} > 0 \quad \forall p_1 > 0.$$

That means that  $\alpha(p_1)$  is strictly monotonously increasing with  $p_1$ . For a given  $\alpha(p_1)$  we thus are able to determine the order of approximation. Thereby, it is important that the approximation of  $\phi^{num}(\Delta x_j)$  by a smooth function  $\phi^{num}(\mathbf{x}, \Delta x_j)$  is of higher order than  $p_1$ .

So far, the error estimate has been derived for a fixed equidistant grid, where  $\alpha(p_1)$  can be evaluated at the nodes of the coarsest grid  $\mathcal{G}_3$ . This is not possible in the case of a meshless method. In particular, we cannot guarantee that the respective particles occupy the same points in space. Furthermore, the discretization is not completely described by a single parameter. Hence, the mesh-size is not appropriate to represent the particle distribution.

Therefore, we introduce for non-uniform meshes the *mean mesh-size*  $\Delta x$ . Assume that the body initially occupies a volume  $V$ . We assign to each particle an averaged volume in the form of a sphere. The mean mesh-size is then defined as the radius of the sphere, i.e.

$$\Delta x = \sqrt[3]{\frac{3}{4\pi} \frac{V}{N}},$$

where  $N$  is the number of particles in volume  $V$ . Let  $\Delta x_i$  be the mean mesh-size corresponding to a number of  $N_i$  particles, then we can compute  $\alpha$  by

$$\alpha(p_1) = \frac{(\Delta x_3^{p_1} - \Delta x_2^{p_1})}{(\Delta x_2^{p_1} - \Delta x_1^{p_1})} = \frac{\left(\frac{\Delta x_3}{\Delta x_2}\right)^{p_1} - 1}{1 - \left(\frac{\Delta x_1}{\Delta x_2}\right)^{p_1}} = \frac{\left(\sqrt[3]{\frac{N_2}{N_3}}\right)^{p_1} - 1}{1 - \left(\sqrt[3]{\frac{N_2}{N_1}}\right)^{p_1}}.$$

This representation is independent of the shape of the small volume assigned to each particle but depends only on the number of particles. To compare the results of the different computations we introduce an artificial regular grid  $\mathcal{G}$  and consider  $\phi^{num}(\mathcal{G}, \Delta x_j)$ .

The applied implementation of FPM provides the possibility to add and to remove particles during the computations if needed. However, this gives only an indirect way to control the number of particles. For a better comparability of the respective results, this feature is switched off in the following. Hence, we consider a fixed number of particles.

Figure 7.13 shows the computed order of approximation  $p_1$  for the density  $\rho$  and the pressure  $p$  denoted by blue and red, respectively, within 20 seconds. The black solid line represents first order accuracy which is the expected value. The colored lines are the mean approximation orders for  $\rho$  and  $p$  averaged over time. The results are obtained applying the infinity-norm  $\|\phi\|_\infty := \max_i |\phi_i|$  to control the maximal errors.

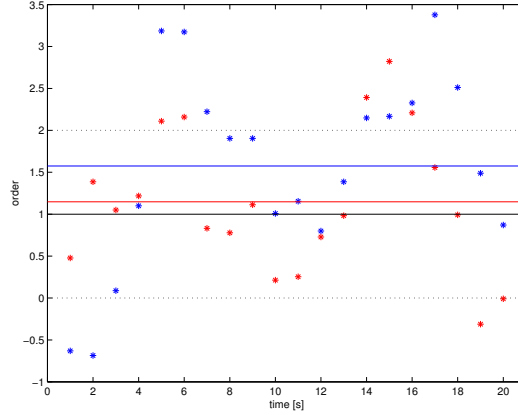


Figure 7.13: Approximation order for density and pressure

We observe a high variation of the computed order of approximation. The time dependent order seems to fulfill an oscillation. This requires further investigations. In particular, we have to discuss the cases where the order is close to or even beneath zero.

- The initial conditions describe a purely rotating, stress-free sphere. This state is far away from an equilibrium and the start-up phase is highly non-stationary. We suppose that in the beginning, the high change rates are responsible for the poor approximation properties.

- According to Figure 7.5, the ball has its largest expansion after approximately 11 seconds. At this time, there are the fewest number of particles within the support of the weighting function  $W^n$ , since we do not add additional particles. Hence, the least squares approximation is only based on few particles and thus becomes worse. In particular, the quadratic pressure profile is approximated poorly.
- On the right hand side of Figure 7.13, the order of accuracy is again very low. Comparing the picture with Figure 7.5 we notice that at this time the circumference of the ball is locally minimal. We suspect two possible reasons for the poor approximation of the pressure. The pressure shows a quadratic profile. In the compressed state,  $p$  is additionally very high such that we suppose that the first order approximation of the quantities is responsible for the observed phenomena. On the other hand, the particle density is very high in the compressed state. Too much particles within the support of  $W^n$  can lead to ill-conditioned matrices in the least squares approximation.

Apart from these regions with low order of approximation, the results are very good. In particular, the averaged order of both quantities lies above the expected order. In most cases the density is better approximated than the pressure due to the problems discussed in the previous section. Anyhow, the presented order of approximation serves only as a rough estimate, since the relative distances of the particles may strongly vary in space.

### 7.3 Validation

To validate the coupled scheme we consider a simple example. The reference body is the sphere with corresponding computational settings. We consider a rotation and divergence free velocity field

$$\mathbf{v}_0(\mathbf{x}) = 0.01 \cdot \begin{pmatrix} x_2 \\ x_1 \\ 0.0 \end{pmatrix} \quad \forall \mathbf{x} \in \Omega.$$

Moreover, we assume that pressure, density and deviatoric stress are initially constant, i.e.  $\rho_0(\mathbf{x}) = 1.0$ ,  $p_0(\mathbf{x}) = 0.0$  and  $S_0(\mathbf{x}) = 0.0$  for all  $\mathbf{x} \in \Omega$ . Note that by this the initial strain rate tensor is constant. The boundary condition are the pressure

$$p(\mathbf{x}, t) = 0.02 \mu t^2$$

for the Euler part and the velocity

$$\mathbf{v}(\mathbf{x}, t) = \mathbf{v}_0(\mathbf{x})$$

for the shear part, for all  $\mathbf{x} \in \partial\Omega$ . The solution of the system (1.30) – (1.33) that corresponds to these initial and boundary conditions is given by

$$\begin{aligned}\rho(\mathbf{x}, t) &= \rho_0(\mathbf{x}) \\ \mathbf{v}(\mathbf{x}, t) &= \mathbf{v}_0(\mathbf{x}) \\ p(\mathbf{x}, t) &= 2.0 \cdot 10^{-4} \mu t^2 \\ S(\mathbf{x}, t) &= \begin{pmatrix} 0 & 0.02\mu t & 0 \\ 0.02\mu t & 0 & 0 \\ 0 & 0 & 0 \end{pmatrix}.\end{aligned}$$

Hence, except for  $S^{21}$  and the pressure  $p$ , all quantities are constant in time and space. The picture on the left of Figure 7.14 displays the evolution of  $\rho$  and  $p$  during 5.0 seconds, where blue and red correspond to density and pressure, respectively. The picture on the right visualizes the course of  $S^{21}$  in time. In the figure, solid lines represent the analytical solutions and the crosses their approximations.

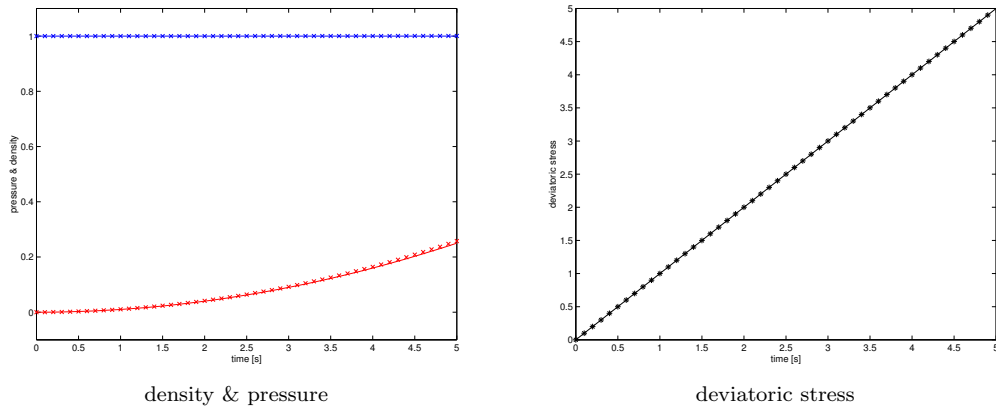


Figure 7.14: Approximation of left:  $\rho$ ,  $p$ , right:  $S^{21}$

The results of the coupled scheme are very satisfying for this academic example. For the density  $\rho$  and the deviatoric stress  $S^{21}$ , we observe no perceivable difference between analytical and numerical solution. After some time, the approximation of the pressure differs from the exact solution. Anyhow, the true pressure is still approximated very well by the scheme.

## 7.4 Discussion

We have numerically shown that the central approximation operators of the respective subsystems yield no stable schemes, whereas the proposed upwind techniques show satisfying results for all systems. The integration of the Jaumann rate forms an exception since it is done analytically.

In case of the Euler part the system-inherent directions can easily be identified. The simulations have shown that the upwinded particle approximation (5.24) in direction of the pressure gradient yields contenting results. The results comply with the ones given in [24].

Due to the complexity of the characteristic system, the situation is different for the shear part. Important system-inherent directions could not be identified. The proposed dimensional upwinding (5.38) shows satisfying results. Thereby, the structure of the dimensional quantities  $\mathbf{v}_{D_{uw}}$  and  $S_{D_{uw}}$  is similar to the one of the upwind quantities  $\mathbf{v}_{uw}$  and  $p_{uw}$ .

The interaction of the subsystems has been investigated considering as an example the dynamic of an elastic sphere. In particular, the influence of the parameters  $c$  and  $g$  of the equation of state has been investigated. The rotation of the sphere has given promising results with regard to known problems.

In all computations except for the shock-tube problem we have considered the behavior of an elastic ball. The reason for this is that a high degree of symmetry is desirable to emphasize the occurring effects. For the free-boundary problems, we have decided against a cube as computational domain in order to avoid possible problems concerning the computation of the surface normals near the corners of the body. However, the Finite Pointset Method has also been applied to complex geometries such as an airbag that is presented in the following picture.

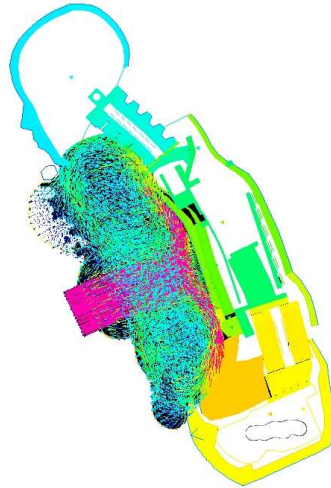


Figure 7.15: Inflation of an airbag

This example is taken from computations done in collaboration with the French software company ESI GROUP, its results can be found in [45]. The aim of the cooperation was the simulation of the inflation of an airbag. For this purpose the FPM implementation has been coupled with PAM-CRASH, a commercial tool developed by the ESI GROUP. The flow inside the initially folded airbag is



computed by means of FPM. This is a highly dynamical problem with a very rapidly changing and complex geometry.



# Conclusion

In this thesis, a numerical scheme on the basis of the *Finite Pointset Method* has been developed to simulate the dynamics of elastic solid bodies. In order to achieve this we have proceeded as follows.

A physical model for elastic solids has been presented. In order to include dynamical processes in a time discretized numerical method the constitutive law has been split up and equations for the update of the deviatoric part of the stress tensor have been stated. A thorough investigation of the physical model and the constitutive law has been given.

It has been shown that the resulting system of partial differential equations is hyperbolic. Important features of that class of systems have been recalled. In particular, we have pointed out the need for a careful numerical treatment of hyperbolic systems. Therefore, the Finite Pointset Method has been equipped with upwinding in one or more directions.

Different physical processes bring forth the motion of an elastic solid. We have provided an operator splitting according to these processes. Thereby, we have been able to consider each of the subsystems in an adequate way.

- For the volumetric part, we have formulated the upwinded particle approximation of the differential system. We have argued that it is not necessary to consider more than one upwind direction. To narrow the number of possible upwind directions down we have introduced the definition of *system-inherent directions*. Euler equations have two system-inherent directions which are the pressure gradient and a direction minimizing a certain quadratic form.

The numerical results have shown that upwinding in direction of the pressure gradient yields a stable numerical scheme provided the particles are moved with the upwind velocity. Thereby, we have validated the results of Kuhnert given in [24] and [25].

- Because of the size of the system and the resulting complexity of the characteristic formulation only one system-inherent direction has been identified for the shear part. From considerations of the two-dimensional case, we have concluded that one upwind direction is not sufficient to

stabilize the method. Therefore, we have introduced the *dimensional upwinding*. In analogy to the Euler part, we have defined the *dimensional velocity* and the *dimensional stress*.

We have numerically shown that the derived scheme is stable provided that the particles are moved with the dimensional velocity.

- The rotation of the stress tensor has been performed analytically on the basis of the local rotation rate matrices.

Results for the fully coupled system have been presented. The simulation of shearing elastic bodies has shown that the scheme is reliable for free-surface problems. Further tests have implied that the consideration of a pure rotation requires a higher order particle approximation to reproduce the stress profile correctly.

The tests have also revealed limitations of the present implementation. Industrially interesting materials such as all kinds of metals have sound speeds much higher than fluids. Due to the explicit time integration, the CFL-condition puts severe restrictions on the size of the time step. In some special applications, a higher order approximation is desirable. The treatment of these aspects should be one element of future work. Moreover, the insertion of plasticity and failure criteria into the physical model is desirable to simulate the whole range of industrial applications connected with solid materials.

*The numerical method derived in the present thesis is capable of simulating the behavior of elastic solid bodies. Thereby, we have provided a tool to study dynamical processes. In particular, the simulation of pure rotations exhibits promising results. Due to the explicit time integration, the present implementation mainly finds its application in the field of high-speed dynamics with rapidly changing geometries.*

# Appendix A

## Proof of Lemma 3.1

We show the equivalence of the two minimization problems (3.6) and (3.8) of Section 3.2 by comparing the  $d_{ij}$ . We restrict ourselves to the two-dimensional case.

Let  $x_j$  and  $y_j$  be the first and the second component of  $\mathbf{x}_j$ , respectively, then

$$p_{\mathbf{x}_i}(\mathbf{x}_j) = c_0(\mathbf{x}_i) + c_1(\mathbf{x}_i)(x_j - x_i) + c_2(\mathbf{x}_i)(y_j - y_i).$$

We consider the solution of the minimization problems for a fixed particle  $i$ .

### Minimization problem (3.6)

Remember that the minimization problem is given by

$$\min_{\mathbf{C}} \|A\mathbf{C} - \mathbf{F}\|^2, \quad (\text{A.1})$$

where  $F_j = W_{ij}f_j$  (no summation) and

$$A = \begin{pmatrix} W_{i1} & W_{i1}(x_1 - x_i) & W_{i1}(y_1 - y_i) \\ \vdots & \vdots & \vdots \\ W_{iN} & W_{iN}(x_N - x_i) & W_{iN}(y_N - y_i) \end{pmatrix}$$

with solution  $\mathbf{C} = (A^T A)^{-1} A^T \mathbf{F}$ . Let  $M := A^T A$ , then  $M$  is symmetric with entries

$$\begin{aligned} m_{11} &= \sum_{j \in P} W_{ij}^2 & m_{21} &= \sum_{j \in P} W_{ij}^2 (x_j - x_i) \\ m_{22} &= \sum_{j \in P} W_{ij}^2 (x_j - x_i)^2 & m_{31} &= \sum_{j \in P} W_{ij}^2 (y_j - y_i) \\ m_{33} &= \sum_{j \in P} W_{ij}^2 (y_j - y_i)^2 & m_{32} &= \sum_{j \in P} W_{ij}^2 (x_j - x_i)(y_j - y_i), \end{aligned}$$

where  $P$  is the index set of all particles. Provided that  $M$  is regular the inverse  $\tilde{M} := M^{-1}$  with entries  $\tilde{m}_{ij}$  exists. We are interested in  $c_0(\mathbf{x}_i)$  which is the first component of  $\mathbf{C}$ . We find that

$$c_0(\mathbf{x}_i) = \sum_{j \in P} (\tilde{m}_{11}W_{ij} + \tilde{m}_{21}W_{ij}(x_j - x_i) + \tilde{m}_{31}W_{ij}(y_j - y_i))F_j$$

such that we can write  $c_0(\mathbf{x}_i) = \sum_j d_{ij}F_j$  with coefficients

$$d_{ij} = \tilde{m}_{11}W_{ij} + \tilde{m}_{21}W_{ij}(x_j - x_i) + \tilde{m}_{31}W_{ij}(y_j - y_i). \quad (\text{A.2})$$

### Minimization problem (3.8)

We minimize the functional

$$\mathcal{G} := \sum_{j \in P} (d_{ij})^2 \quad (\text{A.3})$$

subjected to

$$\begin{aligned} \sum_{j \in P} W_{ij}d_{ij} &= 1 \\ \sum_{j \in P} W_{ij}d_{ij}(x_j - x_i) &= 0 \\ \sum_{j \in P} W_{ij}d_{ij}(y_j - y_i) &= 0. \end{aligned}$$

We solve this minimization problem using Lagrange multipliers. Hence, we write the constraints as

$$\begin{aligned} g_1 &:= \sum_{j \in P} W_{ij}d_{ij} - 1 \\ g_2 &:= \sum_{j \in P} W_{ij}d_{ij}(x_j - x_i) \\ g_3 &:= \sum_{j \in P} W_{ij}d_{ij}(y_j - y_i) \end{aligned}$$

and search for  $\lambda_i$  such that

$$\nabla_d \mathcal{G} + \lambda_1 \nabla_d g_1 + \lambda_2 \nabla_d g_2 + \lambda_3 \nabla_d g_3 = 0. \quad (\text{A.4})$$

The subscript "d" denotes the gradient with respect to the  $d_{ij}$  for fixed  $i$ . Hence, we obtain

$$2 \begin{pmatrix} d_{i1} \\ \vdots \\ d_{iN} \end{pmatrix} + \lambda_1 \begin{pmatrix} W_{i1} \\ \vdots \\ W_{iN} \end{pmatrix} + \lambda_2 \begin{pmatrix} W_{i1}(x_1 - x_i) \\ \vdots \\ W_{iN}(x_N - x_i) \end{pmatrix} + \lambda_3 \begin{pmatrix} W_{i1}(y_1 - y_i) \\ \vdots \\ W_{iN}(y_N - y_i) \end{pmatrix} = 0$$

Multiplying the system by left successively with

- 1)  $(W_{i1}, \dots, W_{iN})$ ,
- 2)  $(W_{i1}(x_1 - x_i), \dots, W_{iN}(x_N - x_i))$  and
- 3)  $(W_{i1}(y_1 - y_i), \dots, W_{iN}(y_N - y_i))$

gives together with  $g_1$  to  $g_3$  a new system

$$M \begin{pmatrix} \lambda_1 \\ \lambda_2 \\ \lambda_3 \end{pmatrix} = \begin{pmatrix} -2 \\ 0 \\ 0 \end{pmatrix}$$

with  $M = A^T A$  as defined before. Again let  $\tilde{M}$  be the inverse matrix, then the  $\lambda_i$  are given by

$$\begin{pmatrix} \lambda_1 \\ \lambda_2 \\ \lambda_3 \end{pmatrix} = -2 \begin{pmatrix} \tilde{m}_{11} \\ \tilde{m}_{21} \\ \tilde{m}_{31} \end{pmatrix}.$$

Hence with (A.4), the  $d_{ij}$  are given by

$$d_{ij} = \tilde{m}_{11} W_{ij} + \tilde{m}_{21} W_{ij}(x_j - x_i) + \tilde{m}_{31} W_{ij}(y_j - y_i) \quad (\text{A.5})$$

which is exactly the same as in equation (A.2). This concludes the proof.

□





# Nomenclature

Throughout this thesis, we have denoted scalar-valued quantities by normal-sized letters ( $c$ ), vectors by bold face letters ( $\mathbf{n}$ ) and matrices by capital letters ( $A$ ). Components of vectors ( $\mathbf{n}$ ) have been distinguished by subscripts ( $n_i$ ). The subscripts  $H$ ,  $S$  and  $R$  refer to volumetric, deviatoric and rotation part, respectively. Furthermore, we have used the following notations:

## Variables and Coordinates

$\mathbf{x}$	Eulerian or actual coordinates
$\xi$	Lagrangian or material coordinates
$\mathbf{n}^{(i)}$	$i$ -th unit vector
$\mathbf{w}$	characteristic variables
$\rho$	density
$\mathbf{v}$	velocity
$\rho E$	total energy
$e$	specific internal energy
$\sigma$	stress tensor
$S$	deviatoric part of the stress tensor
$p$	pressure, volumetric part of the stress tensor
$\mathbf{v}_{uw}$	upwind velocity
$p_{uw}$	upwind pressure
$\mathbf{v}_{D_{uw}}$	dimensional velocity
$S_{D_{uw}}$	dimensional stress

## Elements of the Constitutive Law

$\Omega$	reference configuration
$\Omega_t$	actual configuration at time $t$
$\mathcal{B}$	body under consideration
$X$	motion
$X_t$	motion for fixed time $t$
$X_t^{-1}$	inverse of motion for fixed time $t$
$\mathbf{u}$	displacement
$C$	Green-St.Venant strain tensor

$\varepsilon_\xi$	linearized strain tensor with respect to Lagrangian coordinates
$\varepsilon$	linearized strain tensor with respect to Eulerian coordinates
$\dot{\varepsilon}_\xi$	strain rate tensor with respect to Lagrangian coordinates
$\dot{\varepsilon}$	strain rate tensor with respect to Eulerian coordinates
$R_\xi$	rotation rate matrix with respect to Lagrangian coordinates
$R$	rotation rate matrix with respect to Eulerian coordinates
$\lambda$	Lamé constant
$\mu$	Lamé constant, shear modulus
$\sigma_Y$	yield stress
$\sigma_p$	maximal principal stress
$c$	sound speed
$g$	derivative of pressure with respect to internal energy for constant volume
$\ \cdot\ $	Euclidean norm
$\ \cdot\ _\infty$	infinity norm

### Operators and Functionals

$\partial/\partial t$	partial derivative with respect to time
$d/dt$	total derivative with respect to time
$D/Dt$	material derivative
$\mathcal{L}$	differential operator of the full system
$\tilde{\Sigma}$	characteristic functional with respect to Eulerian coordinates
$\Sigma$	characteristic functional with respect to Lagrangian coordinates
$L$	matrix of left eigenvectors of $\Sigma$
$\Pi$	(least squares) particle approximation operator
$\Pi^h$	smoothed particle approximation operator (SPH)
$\Pi^\pm$	upwinded approximation operator in direction $\pm \mathbf{n}$
$\Pi^c$	mean upwinded particle approximation in direction $\mathbf{n}$
$\Pi_i^\pm$	upwinded approximation operator in direction $\pm \mathbf{n}^{(i)}$
$\Pi_i^c$	mean upwinded particle approximation in direction $\mathbf{n}^{(i)}$
$\Pi_{uv}^{\mathbf{n}}$	particle approximation operator of systems with upwinded convection terms in direction $\mathbf{n}$
$\Pi_{uv}^D$	dimensional upwinding approximation of systems
$W$	SPH smoothing kernel
$W^n$	FPM smoothing kernel

### Sets and spaces

$\mathbb{R}$	set of real numbers
$\Omega$	computational domain
$\partial\Omega$	boundary of the computational domain
$\mathcal{P}_d^\nu$	polynomials of order $\nu$ over $\mathbb{R}^d$
$SO(d)$	special orthogonal group over $\mathbb{R}^d$

# References

- [1] BELYTSCHKO, T., GUO, Y., LIU, W.K. AND XIAO, S.P., *A Unified Stability Analysis of Meshless Particle Methods*, International Journal for Numerical Methods in Engineering, **48**: 1359–1400 (2000)
- [2] BENZ, W. AND ASPHAUG, E., *Impact Simulations with Fracture. I. Methods and Tests*, Icarus, **107**: 98–116 (1994)
- [3] BENZ, W. AND ASPHAUG, E., *Simulations of Brittle Solids using Smoothed Particle Hydrodynamics*, Computer Physics Communications, **87** (1995)
- [4] BENZ, W. AND ASPHAUG, E., *Catastrophic Disruption Revisited*, to appear in Icarus (1999)
- [5] CHADWICK, P., *Continuum Mechanics, Concise Theory and Problems*, George Allen & Unwin Ltd., London (1976)
- [6] CRANDALL, M. AND MAJDA, A., *The Method of Fractional Steps for Conservation Laws*, Numerische Mathematik, **34**: 285–314, Springer-Verlag, Berlin (1980)
- [7] DECONINCK, H., HIRSCH, C. AND PEUTEMAN, J., *Characteristic Decomposition Methods for the Euler Equations*, Proceedings of the 10th Int. Conf. on Numerical Methods in Fluid Dynamics, Lecture Notes in Physics, **264**: 216–221, Springer (1986)
- [8] DECONINCK, H., *Upwind Methods and Multidimensional Splittings for the Euler Equations*, VKI LS 1991–01, von Karman Institute for Fluid Dynamics (1991)
- [9] DEUFLHARD, P. AND HOHMANN, A., *Numerische Mathematik I: Eine Algorithmisch Orientierte Einführung*, 2. Auflage, Walter de Gruyter & Co., Lehrbuch, Berlin (1993)
- [10] DOUGLAS, J.JUN., *Alternating Direction Methods for Three Space Variables*, Numerische Mathematik, **4**: 41–63, Springer-Verlag, Berlin (1962)
- [11] FEISTAUER, M., *Mathematical Methods in Fluid Dynamics*, Longman Scientific and Technical (1993)

- 
- [12] GINGOLD, R.A. AND MONAGHAN, J.J., *Smoothed Particle Hydrodynamics: Theory and Application to Non Spherical Stars*, MNRAS, **181** (1977)
- [13] GODLEWSKI, E. AND RAVIART, P.-A., *Numerical Approximation of Hyperbolic Systems of Conservation Laws*, Applied Mathematical Sciences, **118**, Springer, New York (1995)
- [14] HERRMANN, W., *Constitutive Equations for Large Dynamic Deformations*, Constitutive Laws for Engineering Materials, ASME Press, New York (1991)
- [15] HIERMAIER, S., *Numerische Simulation von Impaktvorgängen mit einer netzfreien Lagrangemethode*, Dissertation, Freiburg (1997)
- [16] HIRSCH, C., *Numerical Computation of Internal and External Flows*, Volume 1 & 2 John Wiley & Sons, New York (2000)
- [17] HUJEIRAT, A. AND RANNACHER, R., *A Method for Computing Compressible, Highly Stratified Flows in Astrophysics Based on Operator Splitting*, International Journal for Numerical Methods in Engineering, **28**: 1–22 (1998)
- [18] JANENKO, N.N., *Die Zwischenschrittmethode zur Lösung Mehrdimensionaler Probleme der Mathematischen Physik*, Springer-Verlag, Berlin (1969)
- [19] JOHN, F., *Plane Waves and Spherical Means Applied to Partial Differential Equations*, Interscience Publishers, Inc., New York (1955)
- [20] JOHN, F., *Partial Differential Equations*, Applied Mathematics Sciences, Springer, New York (1982)
- [21] JUNK, M., *Hyperbolic Conservation Laws and Industrial Applications*, Berichte der Arbeitsgruppe Technomathematik, Kaiserslautern (2001)
- [22] KARLSEN, K.H. AND RISEBRO, N.H., *An Operator Splitting Method for Nonlinear Convection-Diffusion Equations*, Numerische Mathematik, **77**: 365–382, Springer-Verlag, Berlin (1997)
- [23] KHLUDNEV, A.M. AND SOKOLOWSKI, J., *Modelling and Control in Solid Mechanics*, Birkhäuser (1997)
- [24] KUHNERT, J., *General Smoothed Particle Hydrodynamics*, Dissertation, Shaker Verlag, Aachen (1999)
- [25] KUHNERT, J., *An Upwind Finite Pointset Method for Compressible Euler and Navier-Stokes Equations*, Lecture Notes in Computational Science and Engineering, **26**, Springer, New York (2002)
- [26] LANDAU, L.D. AND LIFSCHITZ, E.M., *Lehrbuch der Theoretischen Physik, Band I, Mechanik*, Friedrich Vieweg & Sohn, Braunschweig (1970)

- 
- [27] LEVEQUE, R.J., *Numerical Methods for Conservation Laws*, Second edition, Birkhäuser (1992)
- [28] LEVEQUE, R.J., *Finite Volume Methods for Hyperbolic Problems*, Cambridge Texts in Applied Mathematics (2002)
- [29] LUCY, L., *A Numerical Approach to the Testing of the Fission Hypothesis*, *Astrono. J.*, **82**: 1013 (1977)
- [30] MELOSH, J., *Impact Cratering Modeling*, Impact Cratering and Evolution of Planet Earth, 4th International Workshop, Ancona (1995)
- [31] MONAGHAN, J.J., *An Introduction to SPH*, *Comp. Phys. Commun.*, **48**: 89–96 (1988)
- [32] MONAGHAN, J.J., *Smoothed Particle Hydrodynamics*, *Annu. Rev. Astron. Astrophys.*, **30**: 543–574 (1992)
- [33] MONAGHAN, J.J., *SPH without a Tensile Instability*, *Journal of Computational Physics*, **159**: 290–311 (2000)
- [34] MORRIS, J.P., *An Overview of the Method of Smoothed Particle Hydrodynamics*, *Berichte der Arbeitsgruppe Technomathematik*, Universität Kaiserslautern (1995)
- [35] VON NIDA, M., *A Lagrangian Method for Fracture Dynamics*, Diploma thesis, Kaiserslautern (2001)
- [36] RABCZUK, T., BELYTSCHKO, T. AND XIAO, S.P., *Stable Particle Methods based on Lagrangian Kernels*, *Comput. Methods Appl. Mech. Engrg.*, **193**: 1035–1063 (2004)
- [37] SÄNDIG, A.-M., *Mathematical Methods in Solid Mechanics*, *Berichte der Arbeitsgruppe Technomathematik*, Universität Kaiserslautern (1998)
- [38] SANZ-SERNA, J.M. AND CALVO, M.P., *Numerical Hamiltonian Problems*, *Applied Mathematics and Mathematical Computation* 7, Chapman & Hall (1994)
- [39] SCHICK, C., *Adaptivity for Particle Methods in Fluid Dynamics*, Diploma thesis, Kaiserslautern (2000)
- [40] SCHWARZ, H.R., *Numerische Mathematik*, B.G. Teubner Stuttgart (1988)
- [41] SCHWETLICK, H. AND KRETZSCHMAR, H., *Numerische Verfahren für Naturwissenschaftler und Ingenieure*, Fachbuchverlag Leipzig (1991)
- [42] SEGEL, L.A., *Mathematics Applied to Continuum Mechanics*, Dover Publications, Inc., New York (1987)

- 
- [43] SWEGLE, J., HICKS, D.L. AND ATTAWAY, J., *Smoothed Particle Hydrodynamics Stability Analysis*, Journal of computational physics, **116**, 1: 123–134 (1995)
- [44] TIMOSHENKO, S.P. AND GOODIER, J.N., *Theory of Elasticity*, McGraw-Hill Book Company (1970)
- [45] ULLRICH, P., TRAMEÇON A. AND KUHNERT J., *Advanced Air Bag Fluid Structure Coupled Simulations Applied to Out of Position Simulations*, Europam Conference, Nantes (2000)
- [46] VILA, J.-P., *On Particle Weighted Methods and Smooth Particle Hydrodynamics*, MMMAS, **2**: 161–209 (1999)
- [47] VILA, J.-P., *SPH Renormalized Hybrid Methods for Conservation Laws: Applications to Free Surface Flows*, Meshfree Methods for Partial Differential Equations II, Springer (2004)
- [48] YANENKO, N.N., *The Method of Fractional Steps*, Springer-Verlag, Berlin (1971)
- [49] [http://www.deskeng.com/supplements/fea-\\_elements\\_of\\_analysis/demystifying\\_nonlinear\\_analysis/](http://www.deskeng.com/supplements/fea-_elements_of_analysis/demystifying_nonlinear_analysis/)
- [50] [http://www.efunda.com/materials/common\\_matl/Common\\_Matl.cfm?MatlPhase=Solid&MatlProp=Mechanical](http://www.efunda.com/materials/common_matl/Common_Matl.cfm?MatlPhase=Solid&MatlProp=Mechanical)

## Curriculum Vitae

06. May 1975	Born in Landau in der Pfalz (Rheinland-Pfalz)
1981 – 1985	Attendance at the Grundschule Gommersheim
1985 – 1994	Attendance at the Käthe-Kollwitz-Gymnasium, Neustadt an der Weinstraße
June 1994	Abitur
Oct. 1995 – Dec. 2001	Study of Technomathematics at the University of Kaiserslautern
Nov. 1997	Vordiplom in Technomathematics
Sept. 1998 – March 1999	Study of Technomathematics at Chalmers University, Göteborg
Dec. 2001	Diplom in Technomathematics
Feb. 2002 – Sept. 2005	PhD student at the Department of Mathematics at the University of Kaiserslautern in co-operation with the Fraunhofer ITWM, Kaiserslautern





## Wissenschaftlicher Werdegang

06. Mai 1975	geboren in Landau in der Pfalz (Rheinland-Pfalz)
1981 – 1985	Grundschule in Gommersheim
1985 – 1994	Käthe-Kollwitz-Gymnasium, Neustadt an der Weinstraße
Juni 1994	Abitur
Okt. 1995 – Dez. 2001	Studium der Technomathematik an der Universität Kaiserslautern
Okt. 1997	Vordiplom Technomathematik
Sept. 1998 – März 1999	Studium der Technomathematik an der Technischen Universität Chalmers, Göteborg
Dez. 2001	Diplom Technomathematik
Feb. 2002 – Sept. 2005	Doktorand am Fachbereich Mathematik der Universität Kaiserslautern in Zusammenarbeit mit dem Fraunhofer ITWM, Kaiserslautern